UNIVERSITY OF CALIFORNIA,

Los Angeles

On the Generation and Expulsion of Plasmoids in Earth's Magnetotail

A dissertation submitted in partial satisfaction

of the requirements for the degree

Doctor of Philosophy in Geophysics and Space Physics

By

Shanshan Li

2014

ABSTRACT OF THE DISSERTATION

On the Generation and Expulsion of Plasmoids in Earth's Magnetotail

By

Shanshan Li

Doctor of Philosophy in Geophysics and Space Physics

University of California, Los Angeles, 2014

Professor Vassilis Angelopoulos, Chair

Plasmoids have been observed over a broad distance along Earth's magnetotail, from X= -30 R_E to -200 R_E (X points positively sunward along the sun-Earth line). As described in the near-Earth-neutral-line (NENL) substorm model, reconnection at the NENL causes a plasmoid to be formed and ejected tailward. Because distant-tail (X<-100 R_E) plasmoids are correlated one-to-one with large, isolated substorms, they are reliable remote signatures of substorms. Such a correlation, however, does not exist between mid-tail (-100 R_E < X <-30 R_E) plasmoids and substorms. Also, as indicated in recent studies, magnetic reconnection may be quite localized rather than extending across the entire magnetotail in the dawn-dusk direction. Hence, plasmoid formation and evolution are not well explained by the two-dimensional NENL substorm model. In this dissertation, I will reconcile these seemingly inconsistent observations and describe the formation and expulsion of plasmoids from a three-dimensional perspective using multi-point

observations of mid-tail plasmoids and other reconnection-generated structures (dipolarization fronts and anti-dipolarization fronts).

To understand the formation and expulsion of plasmoids in three dimensions, I investigate the following unresolved questions: What are the three-dimensional configurations of plasmoids in the near-Earth region, the mid-tail, and the distant-tail? Is local lobe reconnection required for plasmoid ejection? How does a plasmoid that originates near Earth evolve while propagating tailward? My results reveal that a mid-tail plasmoid is typically localized and its azimuthal extent increases with increasing substorm intensity. Local lobe reconnection is not always necessary for plasmoid ejection, and thus a plasmoid can grow due to continuous reconnections on closed field lines. Reconnection produced not only plasmoids, but also anti-dipolarization front (ADF), which shares similar observed properties with plasmoids but represents an interface between the reconnected hot outflow and the ambient plasma sheet plasma. In this dissertation, I present a case study suggesting that an ADF could evolve into a plasmoid.

The dissertation of Shanshan Li is approved.

Lawrence R. Lyons

Robert L. McPherron

Christopher T. Russell

Vassilis Angelopoulos, Committee Chair

Table of Contents

ACKNOWLEDGEMENTS

The work in this dissertation would not have been possible without encouragement, support, and guidance from my advisor, Professor Vassilis Angelopoulos. During the past six years, he has spent countless hours patiently guiding my research. No matter how busy he has been, he has never turned me down when I asked for help. His advice about writing and presentation have greatly improved my scientific communication skills. I appreciate the trust and funding he provided me, which enabled me to focus on the scientific topic that interested me. It has been a privilege to have his mentorship on my Ph.D. journey, and his enterprising spirit will continue to influence my life.

I am also grateful for my first mentor in space physics, Professor Zuyin Pu, who was my undergraduate advisor. Professor Pu suggested that I use the flux transfer event (FTE) as my first research topic. Without this research experience, I would not have been able to start my Ph.D. at UCLA, and I would not have chosen plasmoids (flux ropes) as my thesis topic.

Many people contributed significantly to this dissertation. I especially appreciate the generous help from the senior researchers in my research group, Dr. Andrei Runov and Dr. Xuzhi Zhou, who taught me the basics of magnetotail dynamics, and contributed their valuable experience and expertise to my dissertation work. I would also like to thank Dr. Jiang Liu, who shared his front-identification code with me. This code helped me greatly in identifying anti-dipolarization fronts (ADFs) in my fourth research paper. I am also very thankful to Dr. Hui Zhang and Dr. Stefan Kiehas for their fruitful discussions regarding flux ropes and to Dr. Drew Turner for his effort to improve SST instrument calibration.

I am also grateful to many faculty members at UCLA (Christopher Russell, George Morales, Larry Lyons, Margaret Kivelson, Robert McPherron, etc.), who taught me the basics of plasma physics and inspired me with their intelligence and enthusiasm. I greatly appreciate help from Ray Walker in preparing my field exam. My deep gratitude always goes to them as I move forward in science.

I thank many scientists for providing the tools and data used in my study. I acknowledge NASA THEMIS contract NAS5-02099 for financial support during my doctoral studies. I am grateful to John W. Bonnell and Forrest S. Mozer for use of the THEMIS EFI data. I thank Davin Larson and Robert P. Lin for use of THEMIS SST and Charles W. Carlson and James P. McFadden for use of ESA data. I am grateful to Karl-Heinz Glassmeier, Uli Auster, and Wolfgang Baumjohann for the use of FGM data provided under the lead of the Technical University of Braunschweig and for financial support through the German Ministry for Economy and Technology and the German Center for Aviation and Space (DLR) under contract 50 OC 0302. I am grateful to Patrick Cruce, Aaron Flores, Cindy Russell, Brian Kerr, and the rest of the THEMIS programmer team for help in using these data.

I am very thankful to Judy Hohl, who has patiently helped me with her expertise in scientific writing and refined my manuscripts in all aspects (word choice, structure, format, etc).

My great appreciation goes to my academic twin, Dr. Xiaojia Zhang; my officemate, Dr. Christine Gabrielse; and my roommate Hairong Lai, who accompanied me during all the years of graduate school. I wish them great success as space scientists.

Finally, I want to thank my parents and my husband, Dr. Letian Dou, for their unconditional love and support. Without their encouragement, I would not have been able to finish this dissertation.

Shanshan Li

Aug 5th, 2014

Chapter 3 is a version of "Li, S.-S., V. Angelopoulos, A. Runov, X.-Z. Zhou, J. McFadden, D. Larson, J. Bonnell, and U. Auster (2011), On the force balance around dipolarization fronts within bursty bulk flows, *J. Geophys. Res.*, *116*, A00I35, doi:10.1029/2010JA015884".

Chapter 4 is a version of "Li, S. -S. et al. (2014a), Azimuthal Extent and Properties of Mid-tail Plasmoids From Two-point ARTEMIS Observations at the Earth-Moon Lagrange Points, *J. Geophys. Res. Space Physics*, 119, 1781-1796, doi: 10.1002/2013JA019292".

Chapter 5 is a version of "Li, S.-S., V. Angelopoulos, A.Runov, S. Kiehas, X.-Z. Zhou (2013), Plasmoid growth and expulsion revealed by two-point ARTEMIS observations, *J. Geophys. Res. Space Physics*, 118, doi:10.1002/jgra.50105 ".

Chapter 6 is a version of "Li, S.-S., J. Liu, V. Angelopoulos, A. Runov, X. –Z. Zhou, and S. Kiehas (2014b), Anti-Dipolarization Fronts Observed by ARTEMIS, *J. Geophys. Res. Space Physics*, DOI: 10.1002/2014JA020062"

VITA

2004-2008	Bachelor of Science in Space Physics
	School of Earth and Space Sciences, Peking University
2008-2010	Master of Science in Geophysics and Space Physics
	Department of Earth, Planetary and Space Sciences
	University of California, Los Angeles
2008-2014	Graduate Student Researcher
	Department of Earth, Planetary and Space Sciences
	University of California, Los Angeles

MAJOR PUBLICATIONS

Li, S.-S., V. Angelopoulos, A. Runov, X.-Z. Zhou, J. McFadden, D. Larson, J. Bonnell, and U. Auster (2011), On the force balance around dipolarization fronts within bursty bulk flows, *J. Geophys. Res.*, *116*, A00I35, doi:10.1029/2010JA015884

Li, S.-S., V. Angelopoulos, A.Runov, S. Kiehas, X.-Z. Zhou (2013), Plasmoid growth and expulsion revealed by two-point ARTEMIS observations, *J. Geophys. Res. Space Physics*, 118, doi:10.1002/jgra.50105

Li, S. -S. et al. (2014a), Azimuthal Extent and Properties of Mid-tail Plasmoids From Two-point ARTEMIS Observations at the Earth-Moon Lagrange Points, *J. Geophys. Res. Space Physics*, 119, 1781-1796, doi: 10.1002/2013JA019292

Li, S.-S., J. Liu, V. Angelopoulos, A. Runov, X. –Z. Zhou, and S. Kiehas (2014b), Anti-Dipolarization Fronts Observed by ARTEMIS, *J. Geophys. Res. Space Physics*, DOI: 10.1002/2014JA020062

CHAPTER 1 INTRODUCTION

1.1 Plasmoids and Flux Ropes

According to the near-Earth-neutral-line (NENL) substorm model [*McPherron et al.*, 1973; *Russell and McPherron*, 1973; *Hones*, 1977; *Baker et al.*, 1996] illustrated in Figure 1.1, during a substorm, near-Earth-neutral-line reconnection causes part of the closed field line region of the Earth's plasma sheet to be ejected down the magnetotail in the form of a plasmoid. In this model, the NENL, which forms at substorm onset, causes conversion of a significant portion of the magnetic energy stored in the magnetotail to heat and kinetic energy of plasma. Plasmoid release is thought to occur when magnetic reconnection proceeds to include lobe field lines [*Baker et al.*, 1996; *Ieda et al.*, 1998]. When a plasmoid travels down the magnetotail, the lobe magnetic field is compressed and its field lines are draped over the plasmoid. Compression in the total lobe magnetic field (about 5% enhancement) concurrent with a bipolar signature in the B_Z component has been called a traveling compression region (TCR). These regions, which are often observed in conjunction with substorms, have been considered as remote signatures of plasmoids in the magnetotail lobes [*Slavin et al.*, 1984, 2005].

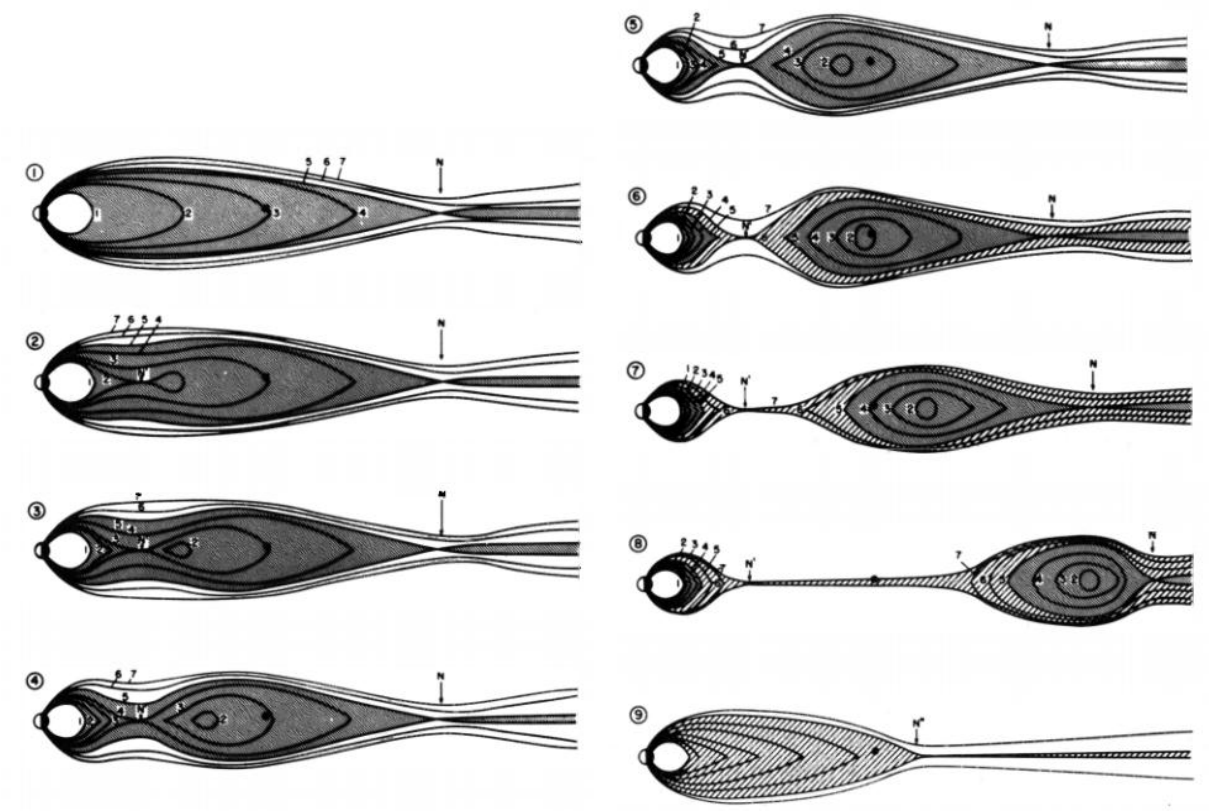

Figure 1.1 Plasmoid formation in two dimensions described by the NENL substorm model.

Correlations between plasmoids/TCRs and substorm activity on Earth have been observed by ISEE3 at the distant tail [*Hones et al.*, 1984; *Slavin et al.*, 1984]. Despite large timing uncertainties associated with the considerable distance between the NENL and the distant tail, a one-to-one correlation between distant-tail plasmoids (those observed beyond 100 R_E downtail) and large isolated substorms has been well documented statistically using observations from ISEE 3, IMP 8, and Geotail [*Richardson et al.*, 1987a; *Moldwin and Hughes*, 1993; *Nagai et al.*, 1994]. Therefore, plasmoids observed in the distant magnetotail have been considered as one of

the most important substorm signatures. Signatures indicating a observation of a typical plasmoid in the magnetotail are shown in Figure 1.2 [*Kiehas et al.*, 2013].

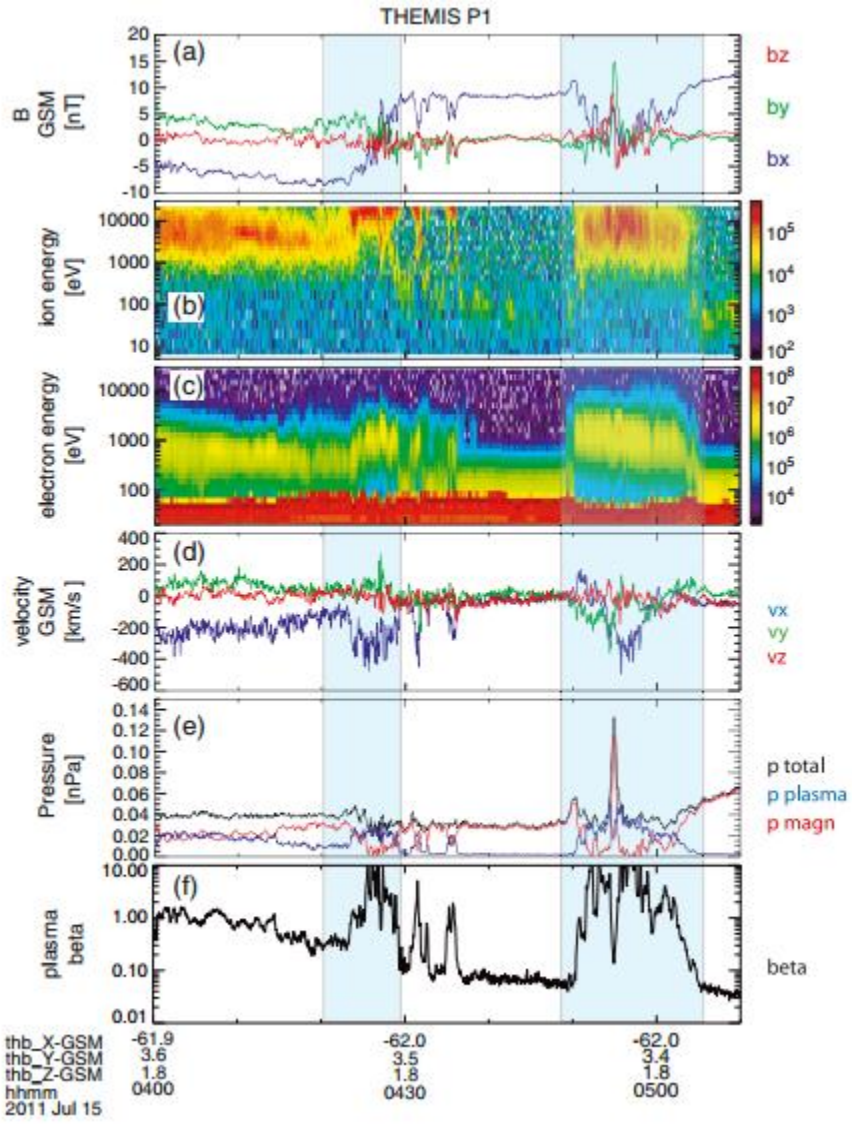

Figure 1.2 Signatures indicating observation of a typical plasmoid at 0455UT on Jul 15, 2011.

Since plasmoids were first described in detail [*Hones*, 1977], our understanding of plasmoid formation and release has changed very little. When NENL reconnection starts, plasma near the reconnection site is heated and accelerated, forming an earthward outflow on the earthward side and a plasmoid-associated tailward outflow on the tailward side. In a two-dimensional scheme, a magnetic loop containing heated plasma is formed between the NENL and the distant neutral line (DNL). After reconnection expands to encompass open lobe field lines, the plasmoid, propelled by tension from the newly reconnected lobe field lines, is released down the magnetotail [*Richardson et al.*, 1987b]. In a three-dimensional scheme, however, the plasmoid typically has a helical field line structure with a core field in the Y-direction that is dependent on the Y-component of the interplanetary magnetic field (IMF) [*Moldwin and Hughes*, 1992a]. Therefore, it is often called a flux rope [*Hughes and Sibeck*, 1987]. Since a flux rope is initially connected to the two ionospheres on its two sides, *Hughes and Sibeck* [1987] thought that for plasmoid release, lobe reconnection must extend over a wide sector of the tail so the resultant tailward tension will overcome the earthward tug from the ionosphere. In my dissertation, I do not distinguish between plasmoids and flux ropes, as the distinction is largely based on the strength of the core field, a quantitative distinction in a continuum of states.

Even though a one-to-one relationship between plasmoids or TCRs and substorm activity has been established, such a correlation between substorms and mid-tail ($-50\ R_E > X_{GSM} \geq -100\ R_E$, GSM stands for the Geocentric Solar Magnetospheric coordinate system) plasmoids/TCRs has not been found [*Nagai et al.*, 1994; *Taguchi et al.*, 1998a]. Similarly, in the near-Earth region ($X_{GSM} \geq -30\ R_E$) a statistical study of 87 plasmoids and TCRs found that only 36 of them were substorm-related (AL<-100nT) [*Imber et al.*, 2011]. A possible explanation for the lack of a

good one-to-one correlation between mid-tail plasmoids and substorms is that the azimuthal extent of mid-tail plasmoids is limited, so plasmoid signatures may be missed by spacecraft in another magnetotail sector. This idea is consistent with the original NENL substorm model, where the neutral line is described to be confined to the magnetotail both azimuthally and along Z_{GSM}[*Russell and McPherron*, 1974]. Statistical studies of the correlation between fast tailward flows (V_X < -400 km/s) used as a plasmoid proxy and the MLT location of substorm onset also indicate that plasmoids are not extended (< 10 R_E) in the azimuthal direction (in Y_{GSM}) in the near-Earth region [*Ieda et al.*, 2008]. Another explanation for the lack of correlation is that ground magnetic field perturbations of small, localized substorms may be limited and thus not easily identifiable by the sparse network of AE stations. In addition, tailward-propagating plasmoids in the near-Earth-tail and mid-tail have occasionally been linked to pseudobreakups rather than fully developed substorms [*Petrukovich et al.*, 1998; *Aikio et al.*, 1999].

It is unclear whether and how localized near-Earth plasmoids evolve into extended distant-tail plasmoids. As revealed by simulations, near-Earth plasmoids may coalesce in the X_{GSM} direction [*Richard et al.*, 1989]. If this is true, coalescence should take place somewhere between the NENL and the distant tail. It could happen anywhere, however, as a plasmoid with limited azimuthal extent in the mid-tail has been inferred from ARTEMIS spacecraft data [*Kiehas et al.*, 2013].

Most plasmoids propagate tailward [*Ieda et al.*, 1998], but quasi-stagnant and earthward-propagating plasmoids have also been observed [*Nishida et al.*, 1986; *Moldwin and Hughes*, 1992a, 1994]. In a statistical study using ISEE-3 observations, equal numbers of earthward-propagating and tailward-propagating plasmoids were observed at X_{GSM} > -100 R_E, indicating

that the DNL is located at X_{GSM} ~ -100 R_E [*Zwickl et al.*, 1984; *Slavin et al.*, 1985; *Moldwin and Hughes*, 1992a]. *Nishida et al.* [1986] proposed that if magnetic reconnection does not proceed to the lobes, the resultant plasmoid would be "trapped" within closed field lines. In such a case, background earthward convective flow from the DNL (assumed to be active) would oppose tailward flow from the NENL [*Nishida et al.*, 1986; *Moldwin and Hughes*, 1994; *Machida et al.*, 2000]. When flow from the DNL dominates, the entire structure, including the NENL and the plasmoid, would be swept earthward [*Slavin et al.*, 2003; *Eastwood et al*., 2005]. However, recent studies on the earthward side of the NENL reconnection site (in the near-Earth tail) reveal that many earthward-moving "plasmoids" do not have round field topologies (when projected normal to their axes), but are dipolarization fronts (DFs), as illustrated in Figure 1.3 [*Sergeev et al.*, 1992; *Semenov et al.*, 2005; *Sormakov and Sergeev*, 2008].

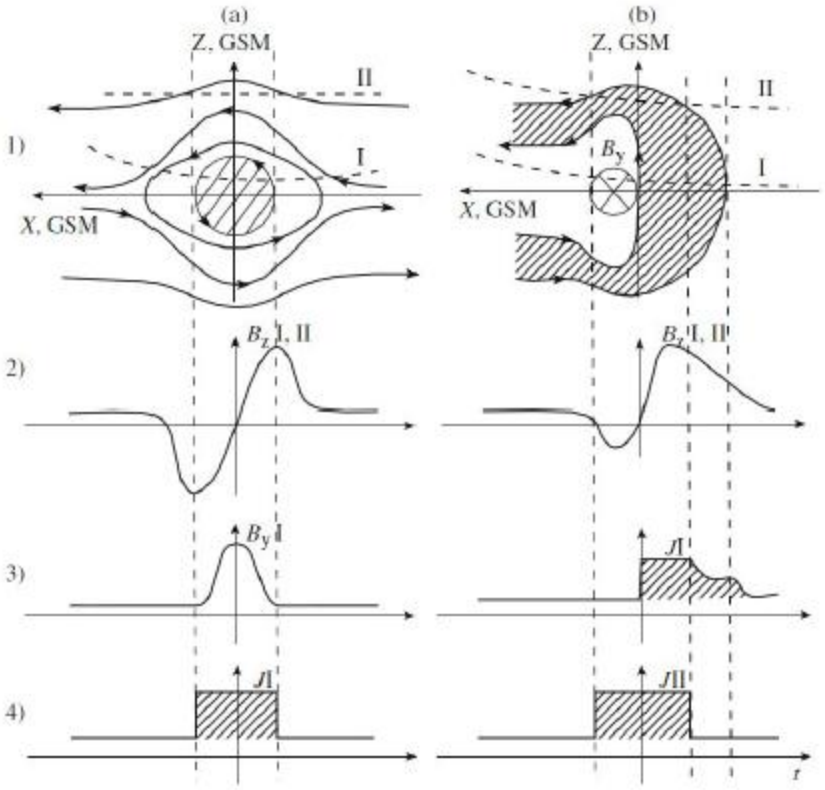

Figure1.3 Examples of two types of structures: (a) magnetic flux rope and (b) single reconnected tube (leading by the dipolarization front) and variations in magnetic field components and energetic electron flux (J) along various trajectories of the spacecraft (I and II).

1.2 Dipolarization Fronts (DFs) and Anti-Dipolarization Fronts (ADFs)

Dipolarization fronts, sudden, significant enhancements in the magnetic field B_Z component (GSM coordinate system), are usually observed to propagate earthward and are embedded within bursty bulk flows (BBFs) [*Russell and Mcpherron*, 1973; *Angelopoulos et al.*, 1992; *Nakamura et al.*, 2002; *Kiehas et al.*, 2009; *Runov et al.*, 2009, 2011; *Liu et al.*, 2013a]. The formation of

DFs has been shown in both magnetohydrodynamic (MHD) simulations and particle-in-cell (PIC) simulations.

Recent observations by the Time History of Events and Macroscale Interactions during Substorms (THEMIS) spacecraft constellation distributed along the tail have demonstrated that dipolarization fronts propagate from the midtail toward the near-Earth plasma sheet [Runov et al., 2009]. They have also been shown to be boundaries separating hot BBF plasma from the ambient plasma sheet population [Runov et al., 2009; Sergeev et al., 2009]. In the presence of large-amplitude DFs, Maxwell tension increases dramatically. If this earthward tension is not balanced by a tailward thermal or magnetic pressure force, the dipolarized flux tube (the structure leading by the dipolarization front) is accelerated earthward. Thus, formation of a dipolarization region seems to be essential to heated BBF plasma intrusion into the near-Earth plasma sheet.

Observations indicate, however, that appearance of a dipolarization front does not coincide with plasma flow onset. A plasma velocity increase, typically observed about a minute before front appearance [Sergeev et al., 2009; Runov et al., 2011], is caused by gradual acceleration of ambient plasma ahead of it. Zhou et al. [2010] suggested a mechanism of ion acceleration by an earthward-moving DF based on a kinetic model of ion motion in a step-like increasing magnetic field. In the MHD framework, ambient plasma acceleration may also be explained as fast-mode waves running ahead of the front.

In a DF a small decrease in B_Z is usually observed before a B_Z enhancement. This signature is similar to the south-north bipolar B_Z signature observed in a plasmoid [*Ohtani et al.*, 2004; *Runov et al.*, 2009, 2011]. Unlike the B_Z decrease associated with the core current structure of an earthward-moving plasmoid, however, the B_Z decrease associated with a DF likely results from a

dawnward current ahead of the front [*Yao et al.*, 2013; *Zhou et al.*, 2014]. Moreover, unlike a plasmoid, a DF separates two distinct plasma populations: dense, cold, compressed ambient plasma ahead of the front from dilute, energetic plasma with a strong magnetic field behind it [*Runov et al.*, 2011; *Liu et al.*, 2013a].

On the tailward side of the NENL reconnection site, tailward-moving structures dissimilar to plasmoids but similar to (mirror images of) DFs have been recently observed [*Angelopoulos et al.*, 2013]. The two ARTEMIS spacecraft at X~ -60 R_E first observed signatures of such a structure at the same time as the three THEMIS spacecraft observed signatures of an earthward-propagating DF (see Figure 1.4). Because both this structure and the DF are considered products of NENL reconnection, they are referred to as reconnection fronts. In this study, I use the term "anti-dipolarization front" (ADF) to represent the reconnection front on the tailward side of the reconnection site. After they are formed at the reconnection site, ADFs are expected to move tailward and DFs are expected to move earthward. The ADF observation is consistent with the MHD simulation of *Ugai* [2011] and the Nightside Flux Transfer Event (NFTE) model [*Semenov et al.*, 2005; *Kiehas et al.*, 2009]. A single fast reconnection site would directly generate a two-part tailward-moving structure: adiabatically compressed ambient plasma ahead of (tailward of) the front and plasma heated by reconnection dissipation with accumulated magnetic flux behind (earthward of) the front [*Ugai*, 2011]. In this dissertation, I study DFs and ADFs to understand acceleration processes ahead of reconnection fronts and the formation and evolution of plasmoids in response to the plasma interaction around these structures, since they are considered to be direct products of NENL.

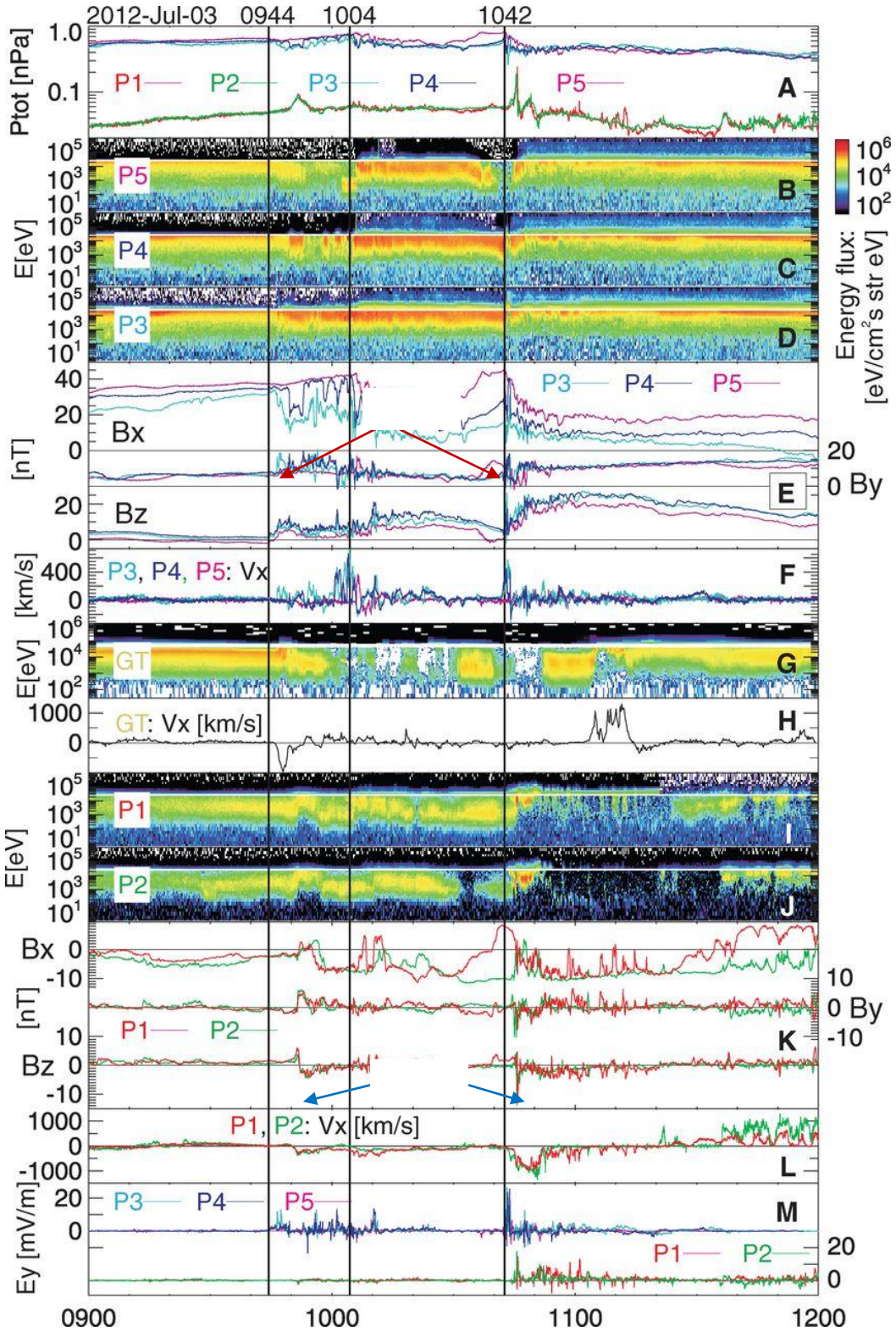

Figure 1.4 An example of observed DF and ADF ("proto-plasmoids") signatures

1.3 Motivation

I study plasmoids because they have been considered to be remote substorm signatures in the magnetotail. Using advanced multi-point observations on mid-tail plasmoids, I seek information about plasmoid formation and expulsion to further understand global substorm dynamics and to improve the NENL substorm model from a three-dimensional perspective.

As discussed in Section 1.1, because of the one-to-one correlation observed between distant-tail plasmoids and large substorms, distant-tail plasmoids are considered to be extended. Hence, the NENL substorm model describes the neutral point as a neutral line across the magnotail. However, this description is inconsistent with near-Earth observations (i.e., dawn-dusk anisotropy [*Imber et al.*, 2011] and the correlation between substorm MLT and tailward flow observations [*Ieda et al.*, 2008]), which suggest that NENL reconnection likely occurs locally, with a preference for the dusk sector of the magneotail. I suggest that a plasmoid may also be formed as a structure with finite size due to localization of NENL reconnection process, and it may evolve considerably during its motion from the near-Earth region to the distant tail. Testing this hypothesis involves addressing two major questions: (1) What are the configuration and properties of a newly formed plasmoid? (2) How does a newly formed "plasmoid" at near-Earth evolve and form an extended rope-like structure at the distant-tail? These questions can be addressed using observational investigations with existing theoretical simulations as references.

Previous statistical studies on plasmoids or TCRs are shown in Table 1.1. Early observations by the ISEE 3 and GEOTAIL missions indicate that plasmoids remain stable after they are fully developed ($X < -100\ R_E$). Systematic observations of near-Earth plasmoids by the Cluster and

THEMIS missions, however, indicate that their properties vary considerably from the near-Earth-tail (X > -30 R_E) to the distant-tail (X< -100 R_E). ARTEMIS, which systematically provides two-point observations at the mid-tail, can improve our understanding of plasmoid development.

Statistical Study on Plasmoids/TCRs						
Data Period	Mission	Measurements	Orbit description	Work	Events #	Highlights
1983	ISEE 3-Geotail	B, electron properties	X=[-240,-40] R_E, biased	[Moldwin& Hughes,1992a]	366 (160)	stable for X<-100 R_E
				[Slavin et al., 1993]	66	35*15*15 R_E estimation
1992Jul-1994	GEOTAIL	B, ion/electron (LEP)	X=[-16,-210] R_E	[Ieda et al., 1998]	824	expanding from near-> mid tail
1998Nov-1999Apr	GEOTAIL	B, ion/electron (LEP)	X=[-10,-30] R_E	[Slavin et al., 2003]	73	
2001-2002	CLUSTER	focus on B (TCR study)	X=[-11,-19] R_E	[Slavin et al., 2005]	148	4-point => flux-rope
2008Dec-2009Apr	THEMIS	B,ion/electron(ESA+SST)	X=[-14,-31] R_E	[Imber et al., 2011]	87	Dusk preference
2010Oct-2011Jul	ARTEMIS	B,ion/electron(ESA+SST)	X=[-50,-70] R_E	?		two-point => scale evidence

Table 1.1 Previous statistical studies of plasmoids and flux ropes.

1.4 Dissertation Outline

In this dissertation, I study formation and evolution of plasmoids using ARTEMIS spacecraft observations at mid-tail. Both statistical studies and case studies reveal the general properties of mid-tail plasmoids (associated with ADFs) and their earthward-moving counterparts, NFTEs (associated with DFs). The dissertation is organized as follows:

In Chapter 2, I introduce the database and methodologies used in this dissertation. In the following chapters, I discuss four studies and their methodologies in detail.

In Chapter 3, I present my study of force-balance evaluation near DFs. I select a typical DF event observed by three inner THEMIS probes (P3, P4, P5). With their special geometrical configuration, I am able to estimate the magnetic field curvature force and the pressure gradient during DF passage. This study reveals that: (1) A dipolarization front is a boundary between the energetic particle population in the flow burst magnetic flux bundle and the ambient colder plasma ahead of the front. (2) Force-density imbalance is found ahead of and behind the front. Ahead of the front, decrease in the tailward pressure gradient force (due to the front arrival) results in earthward flow acceleration; behind the front, even though the radius of field line curvature increases, the curvature force density increases even further, mostly due to an increase in the magnetic field magnitude. Thus, I conclude that plasma acceleration at and immediately after the dipolarization front can be explained by the resultant increased curvature force density.

In Chapter 4, I present my study of the azimuthal ($\sim Y_{GSM}$) extent of mid-tail plasmoids. This study reveals the properties of under-studied mid-tail plasmoid observations and tries to explain inconsistent observations in the near Earth (localized DFs, etc.) and the distant tail (extended

plasmoids). I compare the observed distributions of mid-tail plasmoids with those of near-Earth plasmoids. Then I explore the two-spacecraft observation correlations as a function of their separations in the azimuthal direction and compare the results with my expectations from different assumptions about plasmoid azimuthal size. After confirming the existence of a small but finite population of plasmoids with a highly extended cross-tail size in my database, I investigate them further and suggest that the plasmoid azimuthal extent is related to the intensity of substorm activity.

In Chapter 5, I follow my study of plasmoid generation and evolution with a case study. In this case, two spacecraft were lined up along the direction of plasmoid propagation, and they traversed the plasmoid core near its northern boundary. By analyzing plasma properties, I conclude that the plasmoid ejection might happen without local lobe reconnection, and thus an ejected plasmoid can still grow as the NENL reconnection proceeds to outer field lines.

In Chapter 6, I study anti-dipolarization fronts (ADFs), which are important to plasmoid formation, since they accelerate the plasma tailward immediately following tail reconnection. Superposed epoch analyses are applied on a carefully selected list of well-observed ADFs, and the results are compared to both DFs at the near-Earth region and mid-tail plasmoids selected from the same ARTEMIS database. The comparison confirms that ADFs, interfaces between different flow populations, differ from plasmoids but are similar to DFs. Anti-dipolarization fronts occur frequently in the mid-magnetotail, and, as suggested by a case study, they could evolve into plasmoids.

In Chapter 7, the results of this dissertation are summarized.

CHAPTER 2 Dataset and Methodology

Launched on Feb 17, 2007, the THEMIS (Time History of Events and Macroscale Interactions during Substorms) mission was originally a constellation of five NASA spacecraft (P1 to P5) distributed along the tail with apogees from 10 R_E to 30 R_E. In spring 2010, two of the THEMIS spacecraft, P1 and P2, were inserted into Lissajous orbits around lunar Lagrange points to begin the ARTEMIS (Acceleration, Reconnection, Turbulence, and Electrodynamics of the Moon's Interaction with the Sun) mission. My first case study of force evaluation at a dipolarization front (DF) is based on data from the THEMIS mission, and the three studies on plasmoids and anti-dipolarization fronts (ADFs) are based on data from the ARTEMIS mission.

2.1 THEMIS/ARTEMIS Instrument and Data

The five THEMIS spacecraft are equipped with identical instruments: a fluxgate magnetometer (FGM), an electrostatic analyzer (ESA), a solid state telescope (SST), and an electric field instrument (EFI). The FGM measures the direct-current (DC) magnetic field (Auster et al., 2008). The ESA measures 5 eV to 25 keV ion and electron distribution functions (McFadden et al., 2008). The SST detects high-energy (25keV to 1 MeV) ion and electron fluxes (*Angelopoulos*, 2008b).

Magnetic field data from FGM are available in 3-4s resolution (fluxgate spin-fit, FGS) most of the time and in 4-samples-per-second resolution (FGL) during spacecraft fast-survey intervals (approximately 8-12 hours per day, depending on the year). I applied selection criteria (details in Chapter 2.2) on FGS data and present magnetic field data in highest resolution.

I calculated plasma moments from the full particle angular distributions. The SST transmits full-angle distribution data to the ground in spin resolution during fast-survey intervals (nominally ~8 h per day) and in 1 min resolution during slow-survey intervals (the remainder of the time). The onboard moment computations, though at higher temporal resolution most of the time, are not automatically decontaminated from sunlight effects. When I study and discuss the fine structure of rapidly varying phenomena like ADFs (Chapter 6), I present only data captured during fast-survey intervals. When I study the plasmoid extent using two-point observations statistically with plasma moments (Chapter 4), I applied corrections to the moment data to obtain the thermal pressure during slow survey so as to enlarge my database.

2.2 Methodology

2.2.1 Determination of Plasmoid Azimuthal Extent From Two-Point Observations

I study plasmoid extent based on statistical correlations between observations from the two spacecraft (Chapter 4). First, I develop a set of automated criteria to identify plasmoids using single-spacecraft observations. The spacecraft (P1 or P2) where a plasmoid event is identified using these criteria is hereby called the "reference spacecraft"; the other spacecraft is the "test spacecraft". I then examine the correlation between the reference spacecraft and the test spacecraft. The dependence of this correlation on inter-spacecraft separation is expected to provide an estimate of typical plasmoid azimuthal extent.

I base my operational definition of a plasmoid on three attributes discussed in the Ieda et al. [1998] study of distant-tail plasmoids: (1) a total pressure enhancement>10%, (2) a bipolar signature in the B_Z component with a peak-to-peak difference >2nT, and (3) a tailward flow

speed over 200 km/s. The third criterion includes both earthward- and tailward-propagating plasmoids. To avoid missing plasmoids because of plasma sheet flapping or twisting, I required that at least the reference spacecraft be within the plasma sheet for a conjunction observation to be valid. Thus, for the reference spacecraft, additionally, (4) I require that the spacecraft be inside the plasma sheet (maximum β value >0.5), and (5) I exclude events whose B_Z variations are caused by neutral sheet crossing.

I compare my observations with theoretical predictions and reveal that most of the mid-tail plasmoids observed are fewer than 10 Re in azimuthal extent.

2.2.2 Assessment of Plasmoid Expulsion and Growth From Two-Point Observations

The two ARTEMIS spacecraft are orbiting the Moon near X= -60 R_E, which is exactly the region where plasmoids are thought to evolve from the original near-Earth-tail small (in X_{GSM}) plasmoids to developed distant-tail plasmoids. To study plasmoid evolution after ejection, I surveyed the period when the ARTEMIS spacecraft were lined up in the X_{GSM} direction, the plasmoid propagation direction.

In Chapter 5, I present a case study of a plasmoid observed by both P1 and P2 when they were separated only in the X_{GSM} direction ($\delta Y_{GSM} << \delta X_{GSM}$, $\delta Z_{GSM} << \delta X_{GSM}$). In this event, the two spacecraft were originally located in the northern lobe and traversed the plasmoid above its center. The plasmoid propagated from ARTEMIS-P1 to ARTEMIS-P2 at a speed over 500 km/s, and P2 spent a longer time inside the plasmoid. Based on a thorough examination of the spacecraft configuration and solar wind conditions, I concluded that the plasmoid grows during

propagation. As I suggested from particle observations, such growth is caused by reconnection of closed plasma sheet field lines.

2.2.3 Selection of Anti-Dipolarization Fronts

Unlike a plasmoid, which is usually considered to be a heated plasma sheet bulge, an anti-dipolarization front is a boundary that separates a reconnected plasma population from an ambient plasma sheet plasma population. To select anti-dipolarization fronts, I use the dipolarization front selection criteria of *Liu et al*. [2013a] with some simplifications. My selection criteria for an isolated ADF required that the magnetic field B_Z variation be (1) sharp ($|dB_Z/dt| > 0.5$ nT/s) and (2) large ($|dB_Z| > 5$ nT). Also, the magnetic field B_Z should be (3) significantly negative after front arrival and (4) relatively unperturbed prior to front arrival.

I applied a superposed epoch analysis to the selected ADFs and compared the results with those of a similar analysis of DFs and plasmoids. My goal was to determine whether ADFs, like DFs, are products of reconnection and whether they are distinctively different from plasmoids. Additionally, I studied ADFs observed by two spacecraft for evidence of evolution from an ADF to a plasmoid. Specifically, I checked the observations of electron pitch-angle distributions that indicate evolution in the magnetic field configuration.

CHAPTER 3 On the Force Balance around Dipolarization Fronts

3.1 Introduction

While tailward plasma acceleration from reconnection is required for plasmoid formation and expulsion, it has not been studied extensively in the past. I therefore look for analogs on the earthward side of the reconnection line, where fast earthward flows are more abundant and their properties (including the dipolarization of the magnetic field and plasma heating) have been extensively studied by past (ISEE3, Geotail, AMPTE/IRM) and recent (Cluster, THEMIS) spacecraft. On the earthward side I can benefit significantly from past experience and place the local acceleration process in the context of global substorm dynamics.

Bursty bulk flows (BBFs), which are frequently observed in the plasma sheet, are the most efficient means of transporting energy and magnetic flux in the magnetotail [Angelopoulos et al., 1994]. BBFs are often accompanied by a rapid increase in the magnetic field component normal to the undisturbed cross-tail current sheet (B_z) and a decrease in the plasma thermal pressure. These signatures are similar in the midtail and the near-Earth plasma sheet [Ohtani et al., 2004]. BBF braking in the near-Earth plasma sheet at geocentric distances -10 R_E is one of the most important elements of a magnetospheric substorm [Shiokawa et al., 1998; Baumjohann et al., 1999]. Questions remain, however, about how BBFs are decelerated and which factors control the depth of BBF penetration into the near-Earth plasma sheet.

Impulsive magnetic reconnection in the midtail plasma sheet is generally considered to be the mechanism that generates fast flow bursts [Sergeev et al., 2004]. This mechanism implies plasma acceleration and imbalance between the curvature-dependent components of the $j \times B$ force and

the plasma pressure gradient. Recent particle-in-cell simulations of impulsive reconnection with open boundary conditions have indicated that the force balance is restored in approximately one ion gyroperiod [Sitnov et al., 2009]. Individual flow bursts within BBFs, on the other hand, occasionally show "plasma bubble" properties [Sergeev et al., 1996]. These bubbles are narrow, transient, earthward moving plasma streams with lower density than the ambient plasma sheet population. According to plasma bubble theory (see Wolf et al. [2009] for a review), the relative motion of the bubble is due to lower flux tube entropy $S = pV^{\gamma}$, where S is the entropy, and V is the flux tube volume within the bubble. The inward motion of the bubble continues until the bubble entropy (S_b) equals the entropy of the surrounding plasma. Because the parameter S is global, it is difficult (perhaps impossible) to estimate it using local spacecraft observations. Using local parameters, changes in flux tube entropy in the vicinity of the neutral sheet ($B_x = 0$) may be roughly estimated as $\delta S = \delta(p/Bz)$ [Sergeev et al., 2004]. Dubyagin et al. [2010] conducted a detailed analysis of flux tube entropy changes in the flow-braking region using the Wolf et al. [2006] formula. Here I study the problem of BBF penetration into the dipole-dominated, near-Earth plasma sheet by examining the force densities acting on the flux tube near the magnetic equator.

In the ideal magnetohydrodynamic (MHD) approximatio $\mathrm{d}/\mathrm{dt}(\mathbf{B}/\rho) = (\mathbf{B}/\rho \cdot \nabla)\mathbf{v}$, plasma (considered as a fluid with mass density ρ) and the magnetic field move together at a velocity v. Each magnetic field line, therefore, is a flux tube with a specific plasma population. Considering force densities acting on the equatorial element of a flux tube, the acceleration (or deceleration) of plasma and magnetic field in the tube is defined by the balance between the j × B force and the plasma thermal pressure gradient, or equivalently, between the Maxwell tension and the total

pressure gradient. Ideal MHD simulations of bubble evolution in realistic 2-D geometry have shown a rapid increase in the magnetic field Z component (i.e., dipolarization front (DF) formation) during the early stages of underpopulated flux tube evolution [Birn et al., 2004]. Formation of dipolarization fronts has also been shown in PIC simulations of impulsive magnetic reconnection [Sitnov et al., 2009]. Recent observations by the Time History of Events and Macroscale Interactions during Substorms (THEMIS) spacecraft constellation distributed along the tail have demonstrated that dipolarization fronts may propagate from the midtail toward the near-Earth plasma sheet [Runov et al., 2009]. They have also been shown to be boundaries separating hot BBF plasma from the ambient plasma sheet population [Runov et al., 2009; Sergeev et al., 2009]. In the presence of large-amplitude DFs, Maxwell tension increases dramatically. If this tension is not balanced by the thermal pressure gradient, the dipolarized flux tube is accelerated earthward, towards the inner magnetosphere. In terms of flux tube entropy, S ~ p/Bz experiences a step-like decrease, propelling the dipolarized flux tube deeper inward and leading to acceleration of ambient plasma ahead of the front. Thus, formation of a dipolarization region seems to be an essential element in heated BBF plasma intrusion into the near-Earth plasma sheet.

Imbalance between the Maxwell tension and the total pressure gradient produces a slingshot effect on the ambient plasma ahead of the dipolarization front. This effect has also been recognized by Panov et al. [2010a, 2010b], who showed that the flow bursts interact with the inner magnetosphere recoil via pressure gradient force, initiating a damped oscillatory motion in the Pi2 frequency range.

In this chapter, I consider in detail the force densities acting on the plasma at an earthward moving dipolarization front embedded into a fast bulk flow in the near-Earth plasma sheet. Using the comprehensive data set from THEMIS [*Angelopoulos et al.*, 2008a; *Sibeck and Angelopoulos*, 2008b], I select a case with probe separation suitable for magnetic field curvature estimation and compare the estimated Maxwell tension (curvature force density) in the earthward direction with the corresponding total pressure gradient. I seek to explain the force imbalance and consequent acceleration in the vicinity of the front. Of particular interest to me is the increase in the curvature force during magnetic field dipolarization when the field line curvature radius is actually increasing.

3.2 Observations and Data Analysis

3.2.1 Observations inside the Plasma Sheet

I examined a dipolarization front observed by the three innermost THEMIS spacecraft (P3, P4 and P5) on 0314 UT, March 5, 2009. The configuration of the five THEMIS spacecraft is shown in Figure 3.1. At this time, P3, P4 and P5 formed a closely separated cluster at around X~-10 R_E: P3 at (−10.3, 1.5, −1.8) R_E; P4 at (−9.2, 2.4, −1.6) R_E; P5 at (−9.1, 2.4, −2.3) R_E. The outer two probes, P1 and P2, were located at (−27.3, 13.2, 2.7) R_E and (−18.0, 1.4, −1.6) R_E. It is notable that the front normal Y component was directed dawnward at Y = 1.5 R_E (P3) and duskward at Y = 2.4 R_E (P4/P5). This large difference in front normal direction within a cross-tail distance of 1 R_E indicates a front curvature radius smaller than 1 R_E on the XY plane, which is consistent with the description of Dipolarized Flux Bundle (DFB) [Liu et al., 2013a].

Figure 3.2 shows P2 magnetic and particle observations. Located in the northern half of the plasma sheet ($B_x \approx 15$ nT), P2 observed a quiet, cool plasma sheet (about 1 to 20 keV). Beginning at 031230 UT, P2 observed variations in all three magnetic field components and increases in ion and electron energy and plasma bulk velocity. During flow passage, B_x at P2 changed from 15 nT (before 0313 UT) to almost zero (after 0315 UT), which indicates that P2 was originally located in the northern half of the plasma sheet and subsequently close to the neutral sheet, presumably due to current sheet expansion. However, dipolarization appeared gradually at P2.

Figure 3.3 shows the observations of P3, P4, P5 for the same period as shown in Figure 3.2. The small B_x value detected by P3 and P4 indicates that the probes were located very close to the

neutral sheet. P5 was located in the southern half of the plasma sheet with a B_x level of −30 nT. At around 0314UT, all three spacecraft detected a sudden jump in the B_z component within 13 seconds, referred to as a dipolarization front. The front was accompanied by changes in particle energy spectrograms, similar for all three probes, indicating that the probes crossed a boundary between distinct plasma populations: cool, ambient plasma sheet and the hot plasma populating the dipolarized flux tube. Since P3 and P4 were close to the neutral sheet where B_Z component dominates, the V_X component was mostly perpendicular to the local magnetic field. Thus, as expected, agreement between the X components of the perpendicular ion flow velocity (blue) and E × B drift velocity (black) was observed ahead of the front; most of the particles are in the ESA energy range in the following energy flux spectrum plot. Furthermore, as evidenced by the ion spectra moments (not shown here), a density drop and a temperature rise were also observed by all three probes after front passage.

Figure 3.4 shows the front as a clear boundary for P3 and P4, separating local cold plasma from hot, earthward propagating plasma. In the lower energy range, very little cold plasma is detected inside the dipolarized flux tube, whereas higher densities are detected prior to front arrival. In the higher energy range, the energetic population is only detected within 2 min of front arrival, in good correlation with the flow increase. The hot plasma detected ahead of the front is consistent with local plasma acceleration.

3.2.2 Methodology for Force Density Estimation

Timing of front arrival at P3 and P4, located at $X = -10.3\ R_E$ and $X = -9.2\ R_E$, respectively, reveals its earthward propagation at a velocity of 540 km/s, though the average velocity behind the front was 400 km/s. P5, located at the same X and Y as P4, detected the front and the

energetic plasma population five seconds earlier than P4. This delay is consistent with assumption of an inward moving, but curved (on both XY and XZ planes) front of a flux tube with depleted entropy [Birn et al., 2004; Wolf et al., 2009]. This assumption is also consistent with the front normal direction shown in Table 3.1, evaluated using minimum variance analysis (MVA) [Sonnerup and Scheible, 1998]: Note that the normal direction is plotted projected on the XY and YZ GSM planes in Figure 3.1. However, because the front normal has a non-negligible Y component, the 540 km/s velocity is not appropriate for further calculation. Thus in the following estimation, the average X component velocity after the front is assumed to be the earthward propagation velocity of this flow burst, approximately 400 km/s.

To evaluate the force density balance at the front, I compare the curvature force density F_{curv} and the total pressure gradient force density F_{grad}; both are derived from MHD momentum functions as represented in

$$\rho\left(\frac{\partial \mathbf{u}}{\partial t} + (\mathbf{u}\cdot\nabla)\mathbf{u}\right) = \mathbf{j}\times\mathbf{B} - \nabla P$$

$$\mathbf{j}\times\mathbf{B} = \frac{1}{\mu_0}(\nabla\times\mathbf{B})\times\mathbf{B} = -\nabla\frac{B_z^2}{2\mu_0} + (\mathbf{B}\cdot\nabla)\mathbf{B}/\mu_0$$

$$F_{\text{total}} = F_{\text{grad}} + F_{\text{curv}} = -\nabla\left(\frac{B_z^2}{2\mu_0} + P_{\text{th}}\right) + (\mathbf{B}\cdot\nabla)\mathbf{B}/\mu_0$$

Since all three spacecraft were located close to the neutral sheet, I only evaluated the X component of the force density. As part of the j × B force, the curvature force vector points in the X direction earthward, at the equatorial plane. The other part of the j × B force, the magnetic pressure gradient, forms the total pressure gradient term P_{total} together with the thermal pressure

gradient. Data from P3 and P4 were used to calculate pressure gradient force density, because they were located near the equatorial plane.

The total pressure gradient force density in X direction is calculated using

$$F_{\mathrm{grad_x}} = F_{\mathrm{grad_x}}(\mathrm{quiet}) + \left(\frac{\delta(P_{\mathrm{th}} + P_{\mathrm{B}})}{\delta t}\right)/V_{\mathrm{x}}$$

. In this equation, V_X is a constant representing the velocity of front propagation, which is obtained by timing of the front motion. The F_{gradx} (quiet) term is assumed to be a constant that balances the curvature force at quiet time before the front disturbance took place.

The curvature force density in X direction can be obtained by two different methods. The first method (equation A) implies an estimation of the magnetic field curvature radius (R_{curv}):

(A) $$F_{\mathrm{curv_x}} = \left(\frac{B_z^2}{\mu_0}\right)/(R_{\mathrm{curv}})_{\mathrm{min}}$$

. To evaluate R_{curv}, observations at the three innermost probes (P3, P4, and P5) were used. Using multipoint measurements, the magnetic field curvature radius may be estimated by fitting the magnetic field, measured by different probes as a parabola. For simplicity, I assume a 2-D parabolic field line shape expressed as $x = a\,(z - b)^2 + c$, where all of the parameters are time dependent. As shown in Figure 3.3, the similarity between magnetic field variations observed by the innermost probes and their close separation suggest similarly shaped magnetic field lines at the dipolarization front. In other words, I assume the three probes have experienced exactly the same variation in field line structure, only at different locations. To account for the propagation of the BBF, I shifted the magnetic field time series in time for each individual probe so as I have three-point observations of the same field line at each

relative time. After shifting, magnetic field (B_X, B_Z) and probe position (X, Z) data are linearly fitted to the function $B_X / B_Z = 2a(Z - b)$. The curvature radius at the parabola center is considered the curvature radius at the neutral sheet.

The second method of curvature force estimation is based on the modified Harris-type model of a current sheet with a uniform normal magnetic field component. In this model, the magnetic field is B = (B_X, 0, B_Z), where B_X depends only on the vertical coordinate Z:

$B_x = B_{\text{lobe}} \tanh\left(\frac{z - z_0}{\lambda}\right), B_z = \text{constant}$. Here B_{lobe} is the lobe magnetic field strength, z_0 is the neutral sheet (B_X = 0) coordinate, and L is the current sheet half thickness. In this model, the curvature force x component may be expressed as (B) $F_{\text{curv}_x} = (B_z \cdot B_{\text{lobe}})/\mu_0 \lambda$.

3.2.3 Force Density Estimation Result

Figure 3.5 shows the parabolle fitting results indicating the field line shape change from more stretched to more dipolarized as the DF passed the probes. 1 to 6 (the front passed at time 4) in Figure 3.5 mark the same relative times as marked in Figure 3.4.

Figure 3.6 summarizes my force evaluation near the front. The first panel shows the curvature radius variance obtained from the above parabola fitting. The corresponding curvature force based on equation A is plotted in red in the third panel. The black line in the third panel represents the curvature forces estimated from Harris-sheet model (equation B). As we can see, good agreement is achieved between the two methods.

The second panel shows the pressure structure observation by P4: magnetic pressure in blue, thermal pressure in magenta, and total pressure in black; the smoothed total pressure is represented by the red dashed line. This is similar in structure to those detected by P3 and P5 (because of the similarity, neither of the latter variations is shown here). Ignoring the absolute pressure differences between different probes as due to small differences in efficiency factors, I obtain the pressure gradient force density from the temporal file of the pressure by assuming a constant propagation velocity of 400 km/s in the vicinity of the front. Only data from P4 are analyzed with the equation mentioned before, and the pressure gradient force is represented in the forth panel in Figure 3.6.

By assuming a balance between curvature force F_{curv} and pressure gradient force F_{grad} at a quiet time prior to DF detection at 0313 UT when the flow was small, I evaluate only variations in these two force densities assuming they are caused by the approach of the dipolarized flux. The comparison between curvature force density and pressure gradient force density variations in X is shown in the fifth panel in Figure 3.6.

The force density imbalance begins about 1 min ahead of front arrival due to a decrease in the tailward pressure gradient force density. This is consistent with the time at which the velocity starts to enhance ahead of the front in similar studies by Runov et al. [2011]. The consistency between force-derived velocity and observations shown in Figure 3.6 supports the idea that the pressure gradient accelerates the local plasma ahead of the earthward propagating front structure.

Because of the increase in B_Z, the earthward directed curvature force density increased ~0.6 nPa/R_E on average with respect to the quiet time value after front passage. The total pressure

gradient force density, directed tailward most of the time (as shown in the third panel in Figure 3.6), increased only 0.3 nPa/R_E on average. Thus, there was a factor of 2 or greater imbalance between the Maxwell tension (F_{curv}) at the dipolarization front and the total pressure gradient, which explains the following detected acceleration of the energetic plasma inside the tube.

3.3 Discussion and Conclusion

I presented a THEMIS case study of an inward propagating dipolarization front. The configuration of the THEMIS probes allowed us to detect the BBF in the plasma sheet at X = −18 R_E and the dipolarization front at X = −10 and −9 R_E sequentially. The time delay from P2 to P3/P4/P5 indicates the earthward motion of this DF at a velocity of about 500 km/s.

The main goal of my study was to evaluate the origin and effect of local pressure force imbalance at dipolarization fronts. Although MVA reveals the 3-D nature of the DF surface, I assume that effects of front non-planarity do not significantly affect forces along the X direction and therefore use a 2-D geometric representation of the magnetic field lines in the force balance analysis. I evaluated the force density balance at the front by comparing the X components of the Maxwell tension F_{curv} and the total pressure gradient ($\nabla_x P_{total}$). The magnetic field curvature radius was estimated by fitting the observed magnetic field to (A) the parabolic function and (B) the modified Harris function with a uniform B_{mz}. Both methods produced similar estimates of F_{curv}, as indicated in the third panel of Figure 3.6.

The comparison reveals that within the dipolarization front the curvature forces increased dramatically, while the total pressure gradient did not change as much. Although the current sheet half thickness, L, increased to twice the original thickness at quiet time, the increase in

F_{curv} was determined by the step-like increase in B_Z, which prevailed over the increase in L. The observed imbalance between Maxwell tension and total pressure gradient at the front resulted in earthward acceleration of the dipolarized flux tube, which was separated from the ambient plasma by the front. The hot, tenuous population in the dipolarized flux bundle therefore intruded into the near-Earth plasma sheet.

Another important effect related to the observed force density imbalance is ambient plasma acceleration ahead of the front resulting from plasma compression by the dipolarized flux bundle. Analysis of P3 and P4 observations has revealed an increase in the total pressure about 3.5 R_E ahead (earthward) of the front without significant change in the curvature force density. Such enhancement in local pressure (ahead of the front) decreases the gradient between the near-Earth and the dipolarization front. Hence the decrease in the tailward pressure gradient force leads to the observed earthward acceleration of ambient plasma (Figures 3.3 and 3.4). In the MHD framework, the variation in plasma pressure could be explained as due to a fast-mode wave moving ahead of the front. In the kinetic framework, this pressure enhancement has been considered mainly due to the enhancement in earthward streaming ion flux accelerated by the electric field E_Y behind the front [Zhou et al., 2010, 2011]. Distribution function analysis can distinguish between the two mechanisms, by revealing whether a second (earthward streaming ions) population is superimposed on pre-existing plasma, or a single accelerated component is responsible for the flow velocity increase.

This case study suggests that flow bursts accompanied by a large-amplitude dipolarization front will penetrate deeper into the dipole-dominated, near-Earth plasma sheet due to the predominance of the curvature force density. This force results primarily from the magnetic field

increase that builds up to compensate the density depletion within the dipolarized flow burst. Further statistical analysis would be needed to determine how common these results are. However, I note that the characteristics of the flow bursts surrounding a dipolarization front, the pressure increase ahead of it and the sudden increase in B_Z are common to all events examined, and based on this I anticipate this mechanism to be common rather than fortuitous.

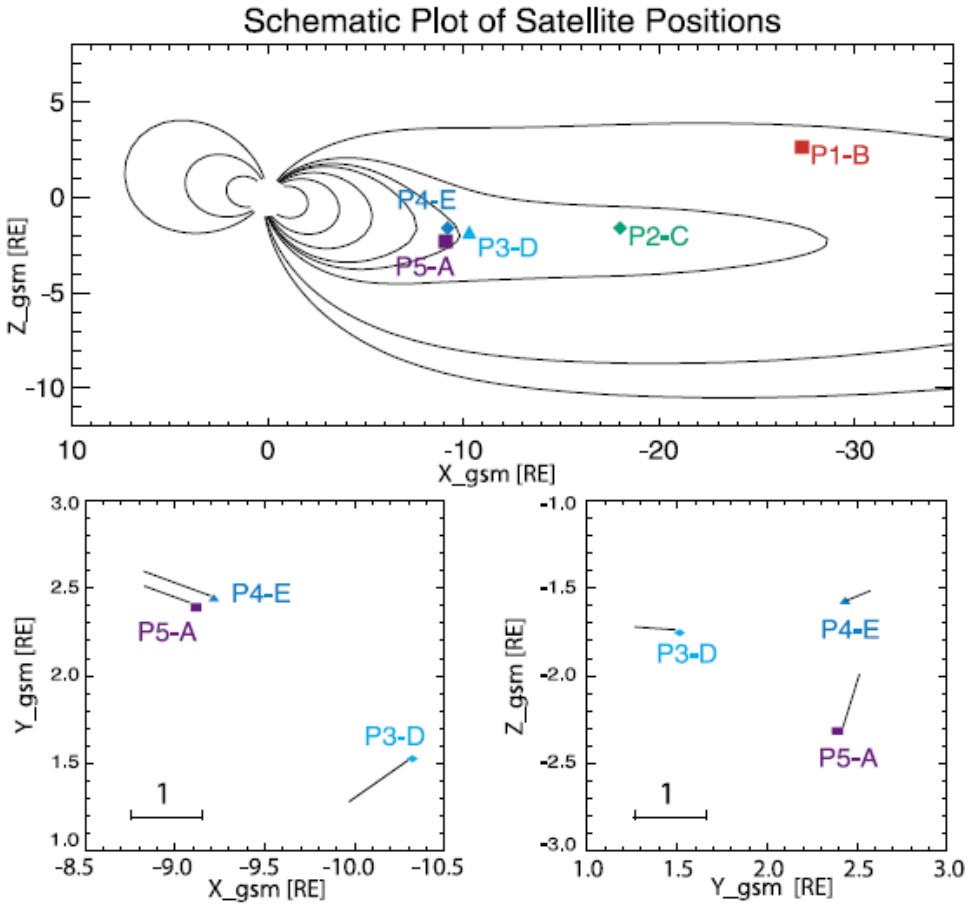

Figure 3.1 The spacecraft configuration at 0314 UT, Mar 5th, 2009. All data are shown in GSM coordinates. The normal directions of the dipolarization front are projected on the XY and YZ plane based on P3, P4 and P5 observations.

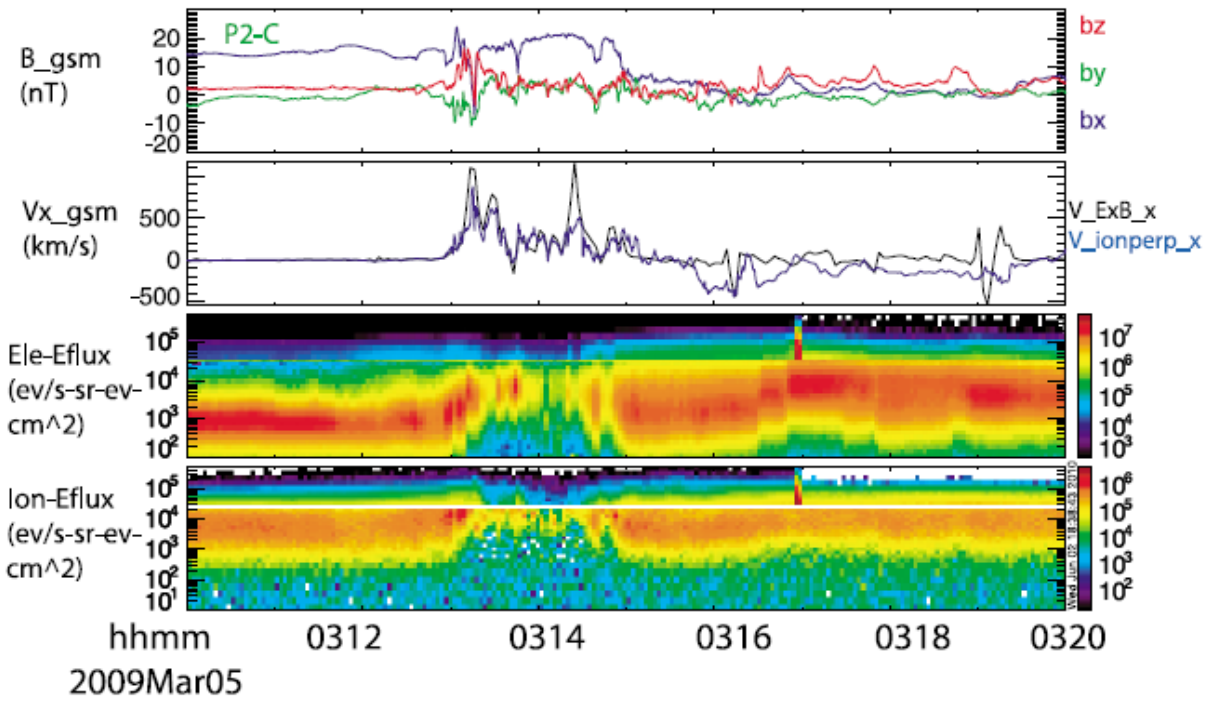

Figure 3.2 Field and plasma properties observed at THEMIS-P2. From top to bottom (GSM coordinate system): magnetic field, V_X, energy-time (ET) spectrograms for electrons, energy-time (ET) spectrograms for ions. In the first panel, magnetic field GSM components B_X, B_Y, and B_Z are plotted using blue, green, and red lines, respectively. The black line in the second panel represents the x component of E × B drift velocity, where E_X, E_Y are obtained from EFI measurement and E_Z is calculated assuming $E \cdot B = 0$ with magnetic field data from FGM measurement. The blue line in the second panel represents the x component of flow velocity calculated from ion fluxes measured by ESA and SST instruments.

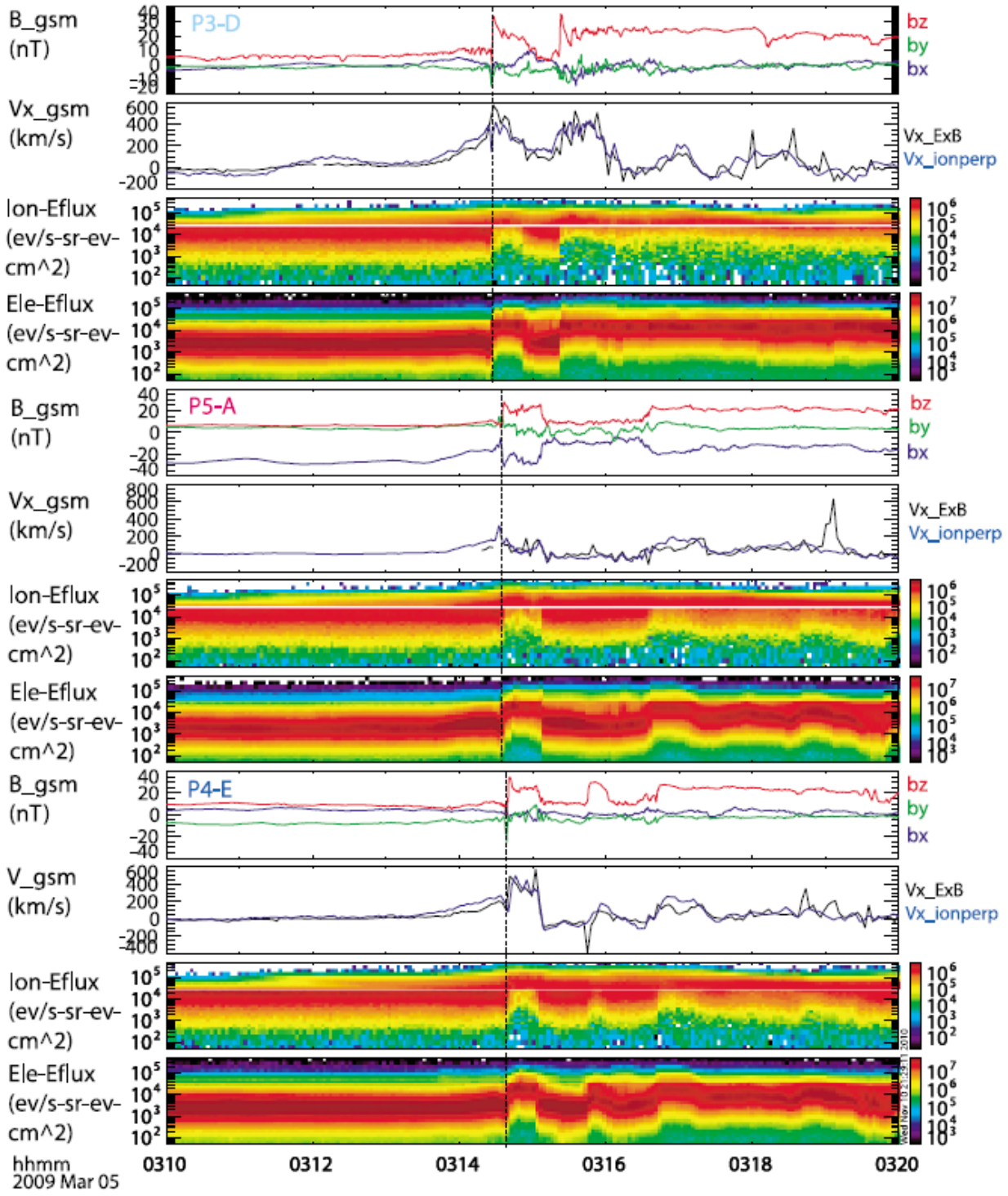

Figure 3.3 Overview of the field and plasma properties encountered by THEMIS-P3/P5/P4. The formats are the same with that of Figure 3.2.

Table 1. Eigenvalues and Front Normal Directions of P3/P4/P5[a]

Probe	Eigenvalue $\lambda1,\lambda2,\lambda3$	Normal Direction	Location
P3-THD	146.9, 15.1, 0.17	(0.82,−0.57,−0.04)	(−10.3,1.5,−1.8) Re
P4-THE	203.6, 19.7, 0.18	(0.93,0.34,0.14)	(−9.2,2.4,−1.6) Re
P5-THA	188.9, 14.2, 0.45	(0.64,0.23,0.74)	(−9.1,2.4,−2.3) Re

[a]Normal direction is chosen as the minimum variance direction obtained by MVA method and written in *X* positive.

Table 3.1 Eigenvalues and Front Normal Directions of P3/P4/P5

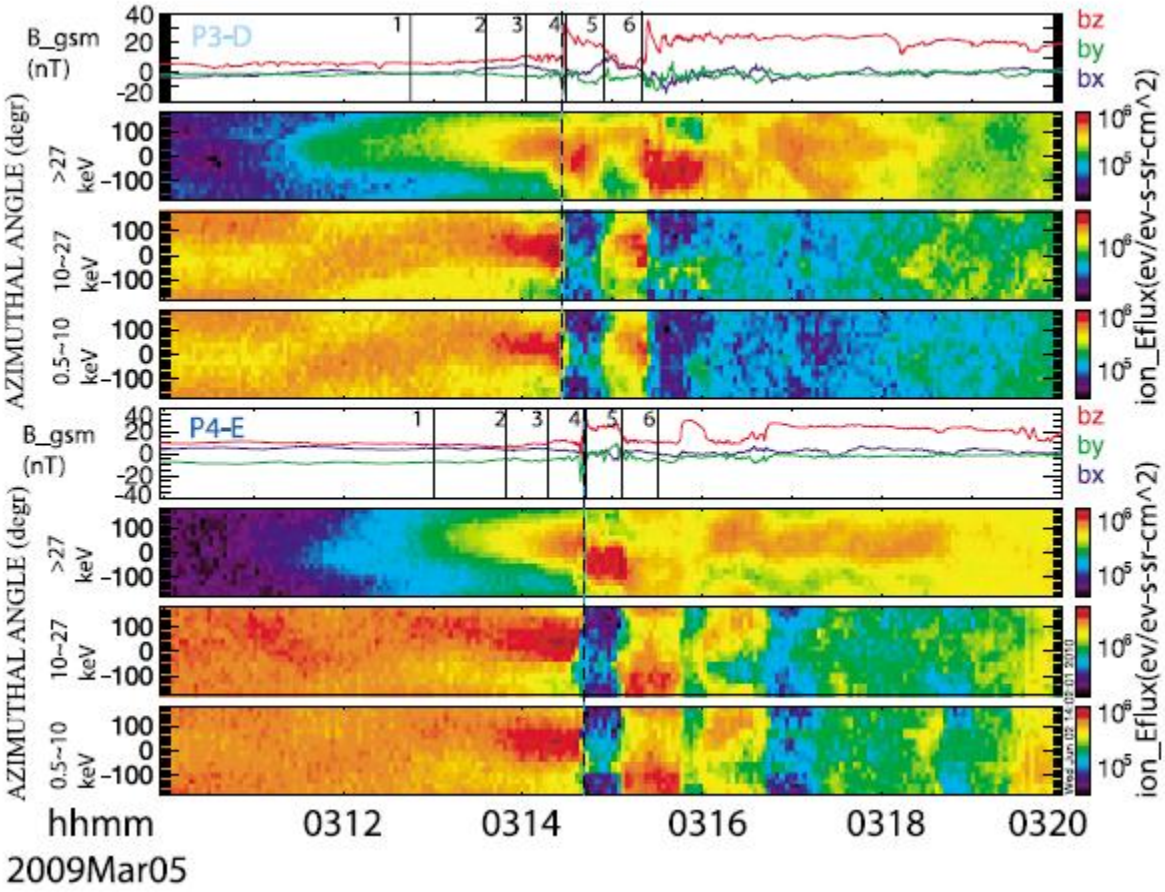

Figure 3.4 Dipolarization front as a boundary separating local cold plasma from hot, earthward propagating plasma. Results for P3 and P4 are shown. Dashed lines mark six signature times.

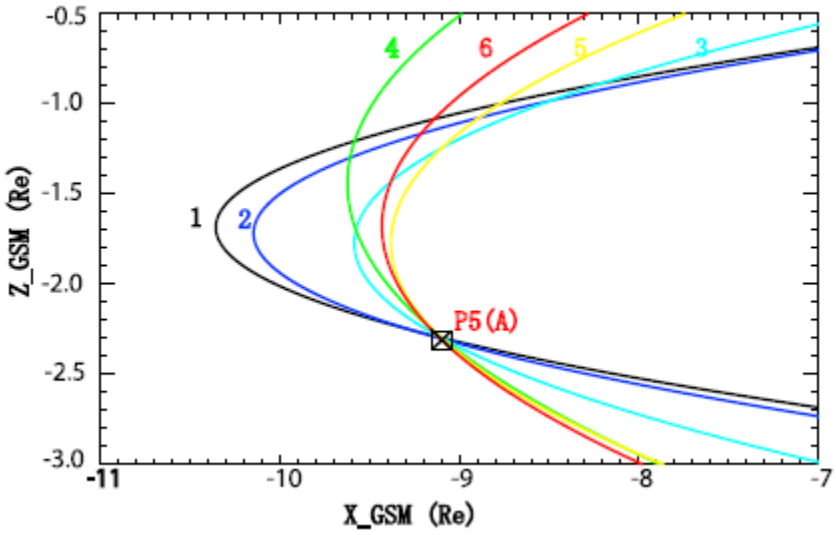

Figure 3.5 Field line parabolic fits for times denoted as 1 to 6 in Figure 3.4. Specifically, time 4 occurs right after the passage of the front structure. Only field lines connected to P5 are plotted here.

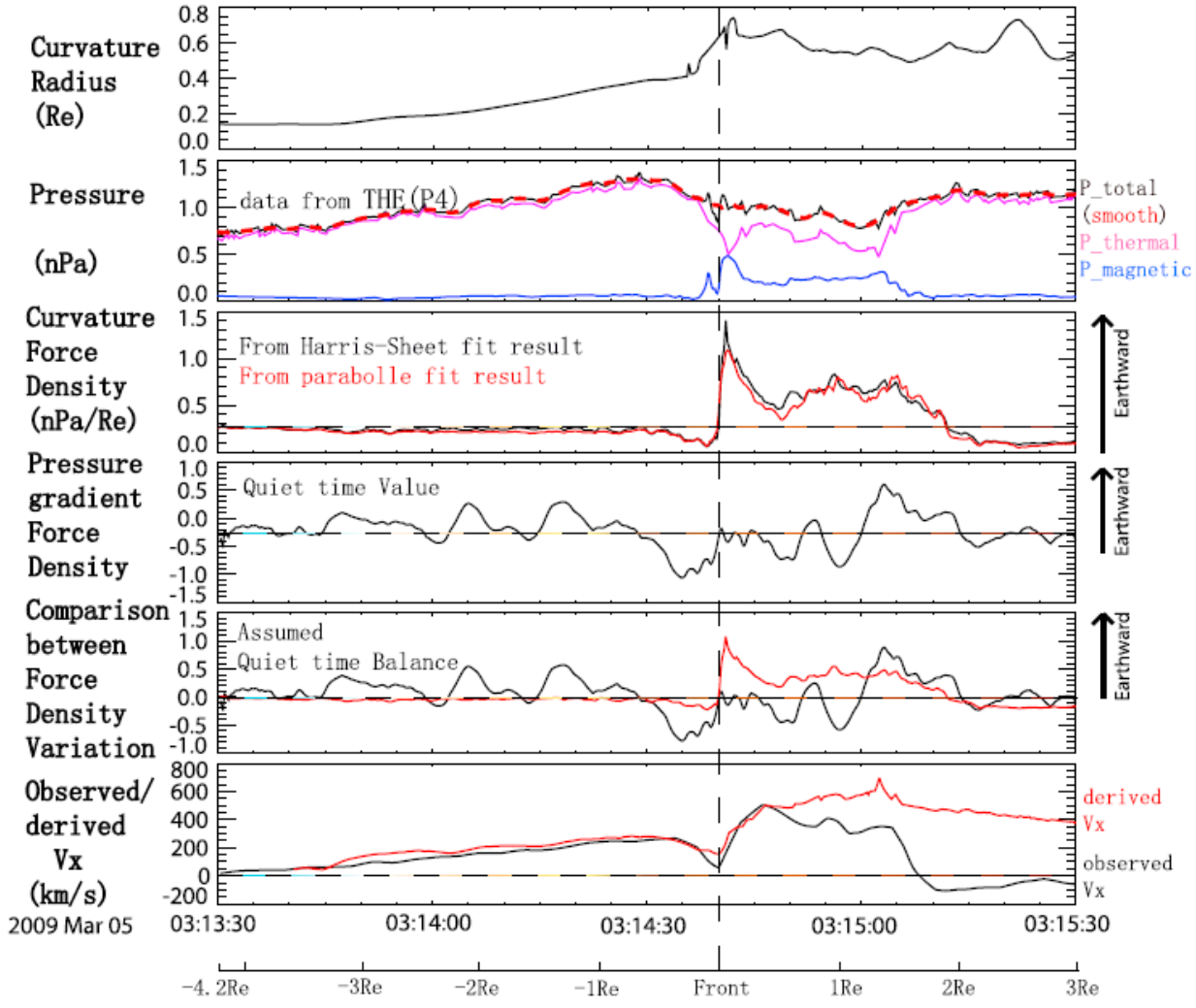

Figure 3.6 Force evaluation results.

CHAPTER 4 On the Azimuthal Extent and Properties of Midtail Plasmoids from Two-point ARTEMIS Observations

Here I study the mid-tail plasmoid azimuthal extent to explain the observational discrepancy between near-Earth and distant-tail plasmoid observations. My goals are to determine the azimuthal extent of plasmoids under a variety of geomagnetic conditions. To achieve this goal, I utilize the data from the ARTEMIS mission because of their special orbit design. Since October 2010, the ARTEMIS spacecraft (probes P1 and P2) [*Angelopoulos*, 2010; *Sibeck et al.*, 2011] have spent 4 days per month in the magnetotail close to lunar orbit. For a nine month period, the spacecraft were in Lissajous orbits on the same or on opposite sides of the Moon [*Angelopoulos*, 2010; *Sweetser et al.*, 2011]. Their separation in the YZ_{GSM} plane varied from less than 1 R_E to more than 20 R_E, with the largest separation along Y_{GSM}. This provides an ideal dataset for addressing the question raised above. I conclude that mid-tail plasmoids are typically 5~10 R_E in azimuthal direction but tend to be more extended during large substorms.

4.1 Introduction

In this study, the spacecraft orbits in the magnetotail are at X_{GSM} = -45 R_E to -65 R_E, which I refer to as the "mid-tail" region. ARTEMIS observations of earthward-propagating and tailward-propagating plasmoids will be compared with observations at the near-Earth (X > -30 R_E) [*Imber et al.*, 2011] and distant tail (X < -100 R_E) [*Ieda et al.*, 1998] regions. As described in the introduction (Chapter 1.1), one-to-one correlation exists between distant-tail plasmoids and substorm, but not between mid-tail plasmoids and substorm. A possible explanation for the lack of such a good one-to-one correlation between plasmoids and substorms is that the azimuthal extent of mid-tail plasmoids is limited, so plasmoid signatures may be missed by spacecraft at

another magnetotail sector. Another explanation is that ground magnetic field perturbations of small, localized substorms may be limited and thus not easily identifiable by the sparse network of AE stations.

Plasmoids and reconnection sites occur preferentially in the dusk sector of the near-Earth (-14 $R_E > X_{GSM} > -30\ R_E$) magnetotail. A statistical survey of plasmoids and TCRs during solar minimum showed that 81% occurred in that sector [*Imber et al.*, 2011]; a study of reconnection sites defined by flow reversals observed by the Geotail satellite also showed a higher occurrence rate in the dusk sector [*Nagai et al.*, 2013]. This dawn-dusk asymmetry supports the idea that plasmoids are not extended structures in the near-Earth region. Bursty bulk flows (BBFs), a product of reconnection on the earthward side, have been shown to be highly localized azimuthally, which indicates that reconnection is also localized [*Angelopoulos et al.*, 1992; *Angelopoulos et al.*, 1997; *Nakamura et al.*, 2004]. From Geotail and WIND observations, BBFs (convective flows) have been found to occur more often on the duskside, whereas field-aligned beams are symmetrically distributed [*Nagai et al.*, 1998; *Raj et al.*, 2002]. Plasmoids, a product of reconnection on the tailward side, should also be azimuthally localized, though this has not yet been confirmed by direct observations. Note that the above studies were not restricted by intensity of ground activity, so their results reflect the most common activity conditions, when the AE index is not necessarily high. As the peak of the expansion phase is reached, azimuthal spreading of earthward fast flows has been demonstrated by multi-spacecraft observations, which suggests that the reconnection region expands azimuthally during active times [*Slavin et al.*, 1997].

It is unclear whether and how localized near-Earth plasmoids evolve into extended distant-tail plasmoids. As revealed by simulations, near-Earth plasmoids may coalesce in the X_{GSM} direction [*Richard et al.*, 1989]. If this is true, coalescence should take place somewhere between the NENL and the distant tail. This coalescence may happen anywhere, however, as a plasmoid with limited azimuthal extent has been inferred in the mid-tail from ARTEMIS spacecraft data [*Kiehas et al.*, 2013].

To obtain further information about plasmoid evolution during its progression from the near-Earth to the distant tail, I perform a statistical study of the azimuthal scale-size of mid-tail plasmoids using the unique, two-point measurement capability of ARTEMIS. In the data analysis section (Section 4.2), I describe my plasmoid event selection criteria (basic and stricter). Then I present the distribution of selected plasmoid events from my database, the correlation between P1 and P2 observations versus different spacecraft separations, and the geomagnetic activity levels for each event. Next I present plasma and magnetic data in detail for three atypical cases: first and second when the two spacecraft were separated azimuthally by a large distance but both observed a plasmoid; and third when the spacecraft were separated by a small azimuthal distance but only one of them observed a plasmoid. In the discussion and conclusions section (Section 4.3), I estimate typical plasmoid azimuthal extent and suggest an explanation for the abovementioned size discrepancies in the near-Earth and distant-tail regions.

4.2 Data Analysis

4.2.1 Dataset

I examine magnetic field and plasma data at 3-4s resolution (spin period was increased during this time from 3 to 4 s) from instruments onboard ARTEMIS, including the fluxgate magnetometer (FGM) [*Auster et al.*, 2008], the electrostatic analyzer (ESA) [*McFadden et al.*, 2008], and the solid-state telescope (SST) [*Angelopoulos*, 2008b].

In my plasmoid observations, a significant portion of ions falls in the >25 keV energy range captured by the SST. The SST transmits full-angle distribution data to the ground in spin resolution during fast-survey intervals (nominally ~8 hours per day) and in 1-min resolution during slow-survey intervals. At the same time, the SST onboard software calculates moments in spin resolution in both slow-survey and fast-survey intervals. I correct the effect of sun contamination to the SST full-angle particle distributions transmitted to the ground using the following standard procedure: I manually remove the contaminated angle bins and interpolate these affected angle bins between the unaffected angle bins in each SST distribution. This standard procedure is not available to the onboard software, however. Hence, the onboard moment estimations, though at higher temporal resolution most of the time, are not automatically decontaminated from sunlight effects. In order to obtain the correct ion thermal pressure at high time resolution, I applied the following simple technique: (i) I removed the sun contamination from the full-angle distribution dataset (1-min resolution during slow-survey) and obtained the difference between the original (contaminated) and the cleaned, ground-processed omni-directional energy spectrograms. This difference, caused by sun contamination effects, varies very slowly. (ii) I removed my sun contamination estimate (after interpolation at 3 second resolution) from the 3s onboard-calculated energy spectrograms and combined the resultant spectrum with that from the ESA instrument (in the 0-25 keV energy range). (iii) Assuming that

the resulting energy spectrogram reflects a shifted (flowing) Maxwellian distribution based on the ESA-computed velocity, I calculated the ion-thermal pressure from this spectrogram. For typical distant plasma sheet temperatures of a few keV, the contributions of the energetic SST ions to the plasma velocity and density are very small compared to the contributions of those ions to the pressure. Thus, this technique has not been attempted for correcting the partial velocity and density from the SST ions. The ESA-derived partial velocity and density have been used as good approximations of the total velocity and density of the plasma.

4.2.2 A Typical Plasmoid Observed by Two Spacecraft

Figure 4.1 shows a typical plasmoid observed by both ARTEMIS spacecraft at 1015 UT on 15 June 2011. Probe 1 (P1) was located at (-51.6, -7.1, 1.7) R_E and P2 was at (-49.2, -5.9, 1.3) R_E in aberrated Geocentric Solar Magnetospheric (AGSM) coordinates. Separated by >2 R_E in the YZ_{AGSM} plane, the two spacecraft observed a similar plasmoid structure. In Panels 4.1(d) and 4.1(h), a total pressure enhancement over 2 minutes in duration centered at around 1015 UT reveal plasmoid passage. As indicated in Panel 4.1e (4.1i), P1 (P2) was originally located at the outer plasma sheet or lobe, then traversed the plasmoid and went back to the ambient plasma sheet. Panel 4.1b (4.1f) shows that during plasmoid traversal, the B_Z component had a clear north-south bipolar signature and the B_Y component was enhanced in the duskward direction. The green and red dashed lines represent the peak times of the total pressure at P2 and P1, after low-pass filtering using a 30 second running average. The two peak times show a 40s delay from P2 to P1, indicating tailward propagation at ~400km/s. The plasma velocity observations in Panel 4.1c (and 4.1g) also show a 400km/s peak tailward flow. Both the flow and the time delay of the pressure are consistent with tailward motion of the magnetic structure as inferred from the

north-south signature in the B_Z component. Based on the 400 km/s peak flow speed and its gradually changing profile, this plasmoid cross section along the spacecraft trajectory (in the X_{AGSM} direction, close to the southern edge of the plasmoid) is ~ 6 R_E. Note that this plasmoid's cross section along X_{AGSM} would be larger if the spacecraft trajectory were closer to the neutral sheet. Since the two spacecraft were separated by over 2 R_E in the YZ_{AGSM} plane (mostly along Y_{AGSM}), I deduce that this plasmoid should be longer than 2 R_E in the azimuthal direction.

I cannot estimate the full azimuthal extent of plasmoids from case studies alone, as the azimuthal center of a plasmoid cannot be determined using single spacecraft in-situ measurements, so I estimate it statistically. First I develop a set of automated criteria to identify plasmoids using single-spacecraft observations. The spacecraft (P1 or P2) where a plasmoid event is identified using these criteria is hereby called the "reference spacecraft" whereas the other spacecraft is the "test spacecraft". I then examine the correlation between the reference spacecraft and the test spacecraft. The dependence of this correlation on inter-spacecraft separation is expected to provide an estimate of typical plasmoid azimuthal extent.

4.2.3 Criteria for Statistical Study

I investigate periods when both spacecraft were inside the magnetotail ($|Y_{AGSM}| < 20\ R_E$) and the data quality from all instruments was good (SSTs were not contaminated by moonlight and spacecraft were not in the shadow of the Earth or the Moon). When the reference spacecraft (P1 or P2) observed a plasmoid, I checked whether the test spacecraft also observed a plasmoid or TCR within 5 minutes. The five-minute maximum time delay was chosen because in 5 minutes a plasmoid with (typical) 400km/s or greater propagation speed could travel the 20 R_E maximum distance between P1 and P2 along X_{AGSM}. To avoid missing plasmoids because of plasma sheet

flapping or twisting, I required that at least the reference spacecraft be within the plasma sheet for a conjunction observation to be valid. Thus, I applied a set of stricter plasmoid detection criteria for the reference spacecraft than for the test spacecraft. Although the test spacecraft was not required to be in the plasma sheet, it could be at the lobe, from which it could also observe a passing plasmoid as a TCR.

I base my operational definition of a plasmoid on three attributes discussed in the *Ieda et al.* [1998] study of distant-tail plasmoids: a total pressure enhancement >10%, a bipolar signature in the B_Z component with a peak-to-peak difference > 2nT, and a tailward flow speed over 200km/s. I modify these attributes to include earthward-propagating plasmoids as well as tailward-propagating plasmoids. My basic criteria for plasmoid/TCR selection are: (1) The pressure enhancement must be > 10% above the background, estimated as the 30-minute average. Therefore, plasmoids with a pressure enhancement period longer than 30 minutes are not considered in this study. (2) The pressure enhancement must be isolated: the maximum total pressure variation above background within 5 minutes preceding and 5 minutes following the pressure enhancement period must be less than 25% of the peak pressure enhancement above the background. (The duration of a plasmoid passage is confirmed as the period when the total pressure variation rate (|dP/dt|) is greater than 0.01nPa/min close to the beginning and ending time of the pressure enhancement period.) (3) The B_Z bipolar signature within the duration of plasmoid passage must have a peak-to-peak amplitude value greater than 2nT. The peak-to-peak amplitude was selected automatically, and I eliminated events with ambiguous bipolar signatures by visual inspection.

To enhance the reliability of the statistics, I applied stricter plasmoid identification criteria to the reference spacecraft: (1) The total pressure enhancement must be greater than 20%. (2) The pressure enhancement must be isolated (same as for the test spacecraft above). (3) The B_Z bipolar signature must have peak-to-peak amplitude greater than 4nT. (4) Events with B_Z variations caused by neutral sheet crossings are excluded using the criteria described by *Ieda et al.* [1998]: events were eliminated if the difference between the average Bx value before the plasmoid passage and that after the plasmoid passage is larger than 15 nT. (5) The spacecraft must be inside the plasma sheet (maximum β value > 0.5) during the pressure enhancement.

A plasmoid event is a plasmoid selected using my stricter identification method on single spacecraft observations. If both spacecraft satisfied the stricter criteria within 5 minutes, I concluded that the same plasmoid was observed as two plasmoid events since either spacecraft could be considered as reference. As a result, the total number of plasmoid events identified by both spacecraft considered as reference should be larger than the total number of actual plasmoids (up to twice as large, if all plasmoids extended across the entire magnetotail).

In the following section I estimate typical plasmoid azimuthal extent based on the conjunction occurrence rate (how many plasmoids observed by the reference spacecraft were also observed by the test spacecraft) as a function of inter-spacecraft separation. In order to obtain the correct relative ratios, a plasmoid observed by both spacecraft should be counted as two events as it is in my statistical study. My database of 362 hours of observations (260 hours inside the plasma sheet) contained 74 plasmoid events observed by the reference spacecraft. The test spacecraft missed 51 of the 74 plasmoid events and captured 18 plasmoid events (9 pairs) and 5 “TCR” (only able to satisfy the basic criteria) events. Each of the latter two types of events is

categorized as a paired event. I checked all of the paired events visually and confirmed that none of them show oppositely-moving plasmoids.

A superposed epoch analysis of the 74 plasmoid events is shown in Figure 4.2. Zero epoch is the peak time of the total pressure. As expected, 52 tailward-moving plasmoid events (Panel 4.2e) show north-to-south B_Z bipolar signatures (Panel 4.2c) and 22 earthward-moving plasmoid events (Panel 4.2f) show south-to-north B_Z bipolar signatures (Panel 4.2d).

4.2.4 Dawn-Dusk asymmetry

Figure 4.3a shows the separations of the two spacecraft in the YZ_{GSM} plane (vertical axis) plotted against the Y_{AGSM} location of the reference spacecraft (horizontal axis) for all (74) events. Each red star represents a paired event, which means that the test spacecraft observed a plasmoid or a TCR as well. Each blue triangle represents a single event, which means that the test spacecraft observed neither a plasmoid nor a TCR. Numbers denote specific plasmoid events that will be presented individually in Section 2.6. For ease of identification, plasmoid event groupings (singles or pairs) are represented by different colors (blue and red, respectively). Figure 4.3b shows the occurrence rate of these events at various Y_{AGSM} locations (black lines). Although a high plasmoid occurrence rate (>60% of the events) is observed between $-2\ R_E < Y_{AGSM} < 12\ R_E$ (about 30% of the cross-tail distance), the time (green) the reference spacecraft was inside the plasma sheet (identified as times when $\beta > 0.5$) has a uniform distribution in the azimuthal direction ($-20\ R_E < Y_{AGSM} < 20\ R_E$). Indeed, the normalized event distribution (magenta) shows the highest occurrence rate of plasmoids within the $-2\ R_E < Y_{AGSM} < 12\ R_E$ region.

A peculiar minimum at the center (4 R_E < Y_{AGSM} <8 R_E) of the high occurrence rate region can be seen in this figure. Figure 4.3c shows the average Kyoto AE index for different spacecraft locations. Outside the high occurrence rate region, plasmoid observations are consistent with higher AE-index values (see regions -8 R_E < Y_{AGSM} <-4 R_E and 12 R_E < Y_{AGSM} <16 R_E). Inside the high occurrence rate region, the AE-index values are lower than the overall average AE-index value, which suggests that the higher plasmoid occurrence rate on the duskside (-2 R_E < Y_{AGSM} <12 R_E) is not a result of high AE-index values. Moreover, the average AE-index values in the aforementioned localized minimum, 4 R_E < Y_{AGSM} <8 R_E, are not significantly different from the AE-index values in the surrounding high occurrence rate region. Thus, the localized minimum is not due to a pronounced AE-index minimum. Although similar distributions exhibiting localized minima in the broad region of increased occurrence rate at the pre-midnight sector have been observed in a few other statistical studies of reconnection sites and plasmoids in the near-Earth region [*Eastwood et al.*, 2010, Figure 4a; *Imber et al.*, 2011, Figure 9a; *Nagai et al.*, 2013, Figure 3a], their origin remains unclear.

4.2.5 Plasmoid Azimuthal Extent

Figure 4.4a shows the normalized number of all events (events divided by the total number, 74) as function of inter-spacecraft separation (black line). The profile is similar to the normalized residence time (green line), the time the reference spacecraft spent inside the plasma sheet (β > 0.5) in the region where plasmoid observations are most likely to occur (-2 R_E < Y_{AGSM} <12 R_E). This agreement shows that the event selections with different spacecraft separations are not biased by orbital characteristics in the database.

The black line in Figure 4.4b shows the ratio of the red line to the black line in 4.4a. This success ratio represents the probabilities that the test spacecraft will observe a plasmoid at different test-reference spacecraft separations if the reference spacecraft encounters a plasmoid. Note that because of the nature of the orbits and poor statistics, no event was selected when the spacecraft were separated by 6 to 9 R_E, and I chose to eliminate that meaningless zero point between 6 to 9 R_E from the profile in 4.4b. My choice of 3 R_E as the bin size is a compromise between reliability on sufficiently good statistics and resolution in plasmoid scale-size estimation. In addition, I calculate the ideal success ratios for plasmoids of different azimuthal sizes (5 R_E, 10 R_E, 15 R_E, 20 R_E) based on the simple model described in the Appendix A and plot them in Figure 4.4b. I estimate typical plasmoid extent by comparing my observations with the ideal curves. In the range of 0 to 3 R_E spacecraft separations, nearly all plasmoids are observed by both spacecraft (>0.85 success ratio). From 3 to 6 R_E separations, the possibility of observing a plasmoid decreases rapidly to 0.3. Beyond 9 R_E separations, only a few plasmoids can be captured by both spacecraft (the ratio drops to 0 at 9-12 R_E separations). Comparing the data to the model curves, this trend reveals that the typical plasmoid azimuthal extent at around X=-60 R_E should be less than 10 R_E, most likely about 6 R_E.

However, as indicated in Figure 4.3a, in several events the two spacecraft have large separations (> 9 R_E) but still observe plasmoids within 5 minutes of each other (e.g., numbers 1 through 5). I will investigate these special events in detail in Section 2.5. Also, I present a counter-example of the extended plasmoid in which the spacecraft were separated by only 3 R_E but the test spacecraft missed the plasmoid completely (number 6).

Figure 4.5a shows the Kyoto AE-index values for all 74 events (the 9 double-counted events are plotted on top of each other) distributed in different spacecraft separations. The AE-index value for each event is taken as the maximum value of the AE-index within 30 minutes of the total pressure peak. As shown in Figure 4.5a, all paired events observed from extended separations (> 9 R_E) occur under high AE-index conditions. In addition, the events observed when the spacecraft were separated by 3 to 6 R_E are mostly concentrated at AE-index ~ 100 nT. To further confirm my estimation of plasmoid extent based on the entire database, which contains various activity levels, I split the events into three groups according to AE-index range: low (AE <200 nT), moderate (200nT < AE < 400nT), and high (AE > 400 nT). The success ratio curves for the three groups are shown in Figure 4.5b.

For events associated with low (<200 nT) AE-index values, dual plasmoid observations are unlikely (0.15) for separations as low as 3 to 6 R_E. This suggests that for low AE-index values, plasmoid azimuthal size is limited to ~5 R_E (compare the magenta curve in Figure 4.5b to the magenta curve in Figure 4.4b). For events with moderate (200nT < AE < 400nT) AE-index values, none of the plasmoids were captured by both spacecraft when they were separated by over 9 R_E. Hence, for moderate AE-index values, the plasmoid size is less than 10 R_E. Note that my database for moderate AE-index values contains only one plasmoid observed when the spacecraft were separated by 3 to 6 R_E; none were observed when the spacecraft were separated by 6 to 9 R_E. For this reason, success ratios for events with moderate AE-index values are not plotted for separations between 3 and 9 R_E. For events with high (> 400 nT) AE-index values, extended plasmoid observations are presented. The ratios are high for large separation

observations, which indicate that at high AE-index values, the plasmoid size may be larger than 20 R_E.

In summary, from Figures 4.4 and 4.5 I conclude: (1) The plasmoid azimuthal size is typically 5 to 10 R_E. This estimation is based on my dataset in which the majority of events are observed when AE-index peak values are lower than 400 nT. (2) The plasmoid azimuthal extent increases with increasing AE-index values. For AE-index values higher than 400 nT, plasmoids may be larger than 20 R_E.

4.2.6 Case Studies

As revealed by Figure 4.3(a), when the spacecraft are separated by more than 10 R_E, most plasmoids are detected by only one spacecraft, whereas for smaller separations plasmoids are detected simultaneously by both. There are notable exceptions, however: extended plasmoids and exceedingly small plasmoids. I describe these in case studies (see Figures 4.3(a) and Figure 4.5, Numbers 1 through 6).

4.2.6.1 The 1410 UT, 20 December 2010 Events (Numbers 1 and 2)

Figure 4.6 shows the magnetic field and plasma data for the paired event that occurred at 1410 UT on 20 December 2010. The locations of the two spacecraft in AGSM coordinates were: P1 (-65, -1.5, 0.8) R_E and P2 (-54, 14.7, 0.1) R_E. The red dashed line indicates the plasmoid observation by P1; the green dashed line indicates the plasmoid observation by P2. Both of them satisfy the stricter criteria, so two paired events are counted for this observation.

The large pressure enhancement and the north-south bipolar signature in B_Z that defined the plasmoid are clearly seen. Probe 1 (P1) and Probe 2 (P2) observed a similar core field, as evidenced by the negative-to-positive bipolar signature in the B_Y component. Probe 2, located 10 R_E earthward of P1, observed the plasmoid 2.5 minutes earlier than P1. This gives an average plasmoid propagation speed of approximately 400 km/s, which agrees with the observed flow speed. The above observations support the idea that even though they were separated by >16 R_E in the YZ_{AGSM} plane (mostly along Y_{AGSM}), the two spacecraft observed the same plasmoid.

Even though both spacecraft observed the plasmoid within a 5-minute interval, their observations are not identical. As shown in the ion energy spectra and the magnetic field B_x component, both spacecraft were originally located at the northern lobe or plasma sheet boundary layer. Probe 2, which encountered earthward flow before plasmoid arrival, tailward flow during plasmoid passage, and tailward flow after plasmoid passage remained at the plasma sheet near the neutral sheet. When traversing the plasmoid from and back to the lobe region, P1 observed mostly tailward flow (except for a transient earthward flow interval around 14:08:50). Probe 2, however, observed a multi-layer plasmoid structure similar to the structure that will be discussed in Chapter 5. Unfortunately, during this period only slow-survey data are available, and particle full distributions are not at sufficiently high time resolution to help identify the source of the earthward pre-plasmoid flow. The earthward flow could be reconnection outflow from the distant-neutral-line (DNL) [*Nishida et al.*, 1986] or ambient plasma sheet flow caused by compression of the tailward-propagating plasmoid [Will be discussed in *Chapter 5*]. In the reconnection outflow scenario, the DNL would have been active at P2's azimuthal sector (Y_{AGSM}=14.7R_E) and inactive at P1's location (Y_{AGSM} =-1.5R_E), which suggests that the DNL is

either localized or discontinuous. In the ambient plasma sheet flow scenario, P1 may have observed a well-developed plasmoid, whereas P2 observed a plasmoid during its growth and evolution from the plasma sheet. Because P1 and P2 are widely separated in both Y_{AGSM} and X_{AGSM}, the difference in plasmoid observations at the two locations could be caused by azimuthal structuring of the plasmoid or evolution of a growing plasmoid with time. In either case, the coincidence and agreement between the speed, pressure, and magnetic field profiles and magnitudes at the two locations strongly suggest that a single extended plasmoid rather than two independent events was responsible for the observations. These observations, therefore, favor the argument that extended plasmoids occur during times of very strong geomagnetic activity.

4.2.6.2 The 1040 UT ~ 1110 UT, 14 July 2010 Events (Numbers 3, 4, 5)

Figure 4.7 shows magnetic field and plasma data for three plasmoid events in my database that occurred at about 1100 UT on 14 July 2010. Red dashed lines mark the two plasmoid events identified in my database when P1 was the reference spacecraft (# 3, 5). The green dashed line marks the plasmoid event identified by my stricter criteria when P2 was the reference spacecraft (#4 identified by the peak pressure on P2).When P1 identified the first plasmoid as a plasmoid event (#3) using the stricter criteria, P2, the test spacecraft, also recognized this plasmoid using the basic criteria. P2 did not identify this plasmoid as a plasmoid event because it was crossing the plasma sheet at that time. As mentioned in Section 2.3, two plasmoid events (one observed by P1 and the other by P2) within 5 minutes are actually one plasmoid observed by two spacecraft. This is the case for the second plasmoid. The second plasmoid was identified as a plasmoid event (#4, #5) by P1 and P2 as both reference and test spacecraft. Hence, these three events in my database were all categorized as paired events.

During the period shown in Figure 4.7, the two spacecraft were located at approximately: P1 (-60, 9.6, -1.7) R_E and P2 (-53, -1.5, 3.6) R_E in AGSM coordinates. Thus, P1 and P2 were separated by >12 R_E in the YZ_{AGSM} plane. They both detected two (presumably large) plasmoids at ~1040 UT and at ~1110 UT. Probe 1 (P1) was originally located in the southern lobe, and P2 was located inside the plasma sheet. The pressure enhancements and north-south bipolar B_Z signatures for both events can be seen in Figure 4.7. Tailward flows (with no earthward pre-plasmoid flows) were observed at both spacecraft during all three events (#3, 4, 5). Note that in P1's observations of event #3, even though the bulk velocity (calculated based on < 25 keV particles) does not show tailward flow, the energetic particles (>25 keV) have a clear tailward direction (not shown here). For events #4 and #5, P1, located duskward of P2, observes an obvious duskward flow. This is probably because P1 is closer to the duskside edge of the plasmoid. Interestingly, however, several TCRs were observed at P1 between the two paired events but there was no evidence of them at P2, suggesting that despite the large azimuthal extent of the two plasmoids discussed here, there is also evidence for more localized structures in the magnetotail in this period.

4.2.6.3 The 0315 UT, 17 April 2011 Event (Number 6)

Figure 4.8 shows the magnetic field and plasma data for the 0315 UT, 17 April 2011 event. Probe 1 (P1) is the reference spacecraft; its pressure enhancement peak time is indicated by the red dashed line. Just before the plasmoid was observed by P1, a clear substorm onset is evident in the AE-index. Typical substorm signatures were also observed by the two THEMIS [*Angelopoulos*, 2008b] probes (THEMIS-A or probe P5 and THEMIS-E or probe P4) located near midnight at the outer central plasma sheet and close to geosynchronous orbit (not shown

here): Before and after AE onset, gradual enhancement of and decrease in magnetic field strength were observed, which indicates plasma sheet thinning and recovery before and after substorm onset.

The ARTEMIS spacecraft AGSM locations were: P1 (-46, 16.6, 2.9) R_E and P2 (-44, 12.3, 1.3) R_E. Although the two spacecraft were separated by only about $4R_E$ in YZ_{AGSM}, they observed quite distinct signatures. P1 observed a tailward-propagating plasmoid with a clear pressure enhancement, a south-then-north bipolar B_Z signature, a dawnward B_Y core field, and tailward plasma flow. P2, on the other hand, observed an ambiguous, broad pressure enhancement without a clear bipolar B_Z component or evidence of a core field in B_Y and a much slower tailward and duskward flow (about 200km/s in the -X and +Y directions). I infer that P2 most likely encountered the perturbed plasma sheet plasma surrounding a localized plasmoid observed by P1. Even though only P1 captured the plasmoid as identified based on total pressure enhancement and bipolar B_Z signature, the flow perturbations surrounding the plasmoid were actually observed by P2 as well. (The flow perturbations refer to the Vx and Vy enhancements observed by P2, which started when P1 observed the plasmoid.) This event suggests that the azimuthal extent of flow perturbations surrounding plasmoids near lunar orbit (X~-60 R_E) may be larger than the azimuthal extent of the plasmoids' magnetic and peak-pressure signatures.

4.3 Discussion and Conclusions

The above statistical study of mid-tail plasmoids near lunar orbit reveals three features: (1) Plasmoids occur more frequently in the dusk sector of the magnetotail, similar to plasmoids and reconnection sites in the near-Earth region reported previously. (2) The typical plasmoid azimuthal size is only 5~10 R_E, assuming the peak AE-index values are lower than 400nT, a

most common condition. (2) Occasionally, extended plasmoids (>12 R_E) are observed during large AE enhancements (>400nT). This is taken as indication of a positive correlation between mid-tail plasmoid azimuthal extent and ground activity level (determined by the AE-index).

In the superposed epoch analysis plot (Figure 4.2), the Bz perturbation for the 52 tailward-propagating plasmoids has an asymmetric bipolar signature (south perturbation is stronger than north) that is probably related to inclusion of a special type of plasmoid with a front-like sudden decrease in B_Z. Observations of this type of plasmoid have been presented in a recent study [*Angelopoulos et al.*, 2013]. Such asymmetric plamoids could be described well by the tailward-moving reconnection fronts (reconnection fronts are defined in [*Angelopoulos et al.*, 2013], which represent a pair of fronts propagating oppositely towards the earth and the distant-tail), which have the same nature as DFs [*Sormakov and Sergeev*, 2008], better than the classical flux rope model. *Angelopoulos et al.* [2013] suggested that these front-like plasmoids have just emanated from the reconnection site. Because they are closer to the X-point, their northward excursions are not so prolonged, and the southern excursions dominate. These so-called "proto-plasmoids" are fairly common in the ARTEMIS dataset. I will discuss front-like plasmoids comprehensively in Chapter 6.

The dawn-dusk asymmetry in plasmoid occurrence rate I observed at the mid-tail is similar (though azimuthally broader) than in previous studies of plasmoids or reconnection flow-reversals at the near-Earth region [*Imber et al.*, 2011; *Nagai et al.*, 2013]. The near-Earth (X > -30 R_E) plasmoid/TCR distribution pattern [*Imber et al.*, 2011] with its sharp boundaries at Y_{AGSM} = 0 and Y_{AGSM} = 10 R_E is narrower than my distribution pattern, which has boundaries at Y_{AGSM} = -2 R_E and 12 R_E (Figure 4.3b). This difference suggests a 4 R_E plasmoid expansion in the

Y_{AGSM} (azimuthal) direction during the 30 R_E tailward plasmoid propagation. If the expansion continues at the same rate at which the plasmoid is propagating tailward, the distant-tail plasmoid ($X<-200\ R_E$) will have an azimuthal length 20 R_E longer than the mid-tail plasmoid, which is consistent with distant-tail observations.

Figure 4.4 reveals that plasmoid azimuthal sizes at $X_{GSM} \sim -60\ R_E$ are limited ($< 10\ R_E$); most are likely 5 to10 R_E. Also, plasmoid observations can be distinctly different even within 3 R_E spacecraft separations (Figure 4.7). Considering the aforementioned estimated plasmoid expansion rate of $4R_E$ (in Y_{AGSM}) per 30 R_E of downtail ($-X_{AGSM}$) propagation, the typical plasmoid in the near-Earth region ($X\sim-30\ R_E$) should be $< 6\ R_E$ (most likely 1 to 6 R_E). The *Ieda* et al. [2008] study of the correlation between tailward flows at the near-Earth region ($X\sim-30\ R_E$) and auroral brightening revealed that plasmoids are originally localized structures in the near-Earth region with typical azimuthal size of about 10 R_E. However, this scale size is considerably larger than my estimate. Two reasons may contribute to this difference. First, the accuracy of mapping from the MLT of auroral brightening to the expected reconnection location in the magnetotail has an error of several R_E in the magnetotail. Second, the studied events associated with clear auroral brightening may be correlated with larger AE-index values than the typical AE-index value in my dataset (median 230nT). Larger AE index values may be statistically associated with azimuthally more extended plasmoids in the Ieda et al. database.

Figure 4.5 suggests a correlation between extended mid-tail plasmoids and high AE-index values that is consistent with the observed one-to-one correlation between distant-tail plasmoids and large substorms [*Moldwin and Hughes*, 1993; *Nagai et al.*, 1994]. In other words, even though most plasmoids are localized structures within and at lunar orbit, only the extended ones are

related to large substorms and thus were selected for analysis. In addition, extended plasmoids may expand further after downtail propagation past lunar orbit, so they have a greater chance of being captured by single spacecraft. Moreover, since the initial azimuthal extent of plasmoids is closely related to the cross-tail width of reconnection sites, such a correlation between extended plasmoids and large AE-index values may also suggest a correlation between the cross-tail extension of near-Earth reconnection sites and substorm intensities. The latter correlation between reconnection site extension and substorm intensity was suggested by *Slavin* et al. [1997] based on simultaneous earthward-propagating BBF observations by multiple, widely separated spacecraft at the peak of the substorm expansion phase. My findings are consistent with the Slavin et al. results.

In this study I suggested a positive correlation between mid-tail plasmoid azimuthal extent and substorm intensity. However, the ARTEMIS spacecraft azimuthal separations never exceed 25 R_E in the database used for this study, and thus plasmoids with extremely large azimuthal sizes (~40 R_E, comparable with the cross-tail length) cannot be identified via two-point ARTEMIS observations. If they exist, these extremely extended plasmoids could be observed by ARTEMIS in conjunction with other missions. Future observational studies are needed to further test this hypothesis.

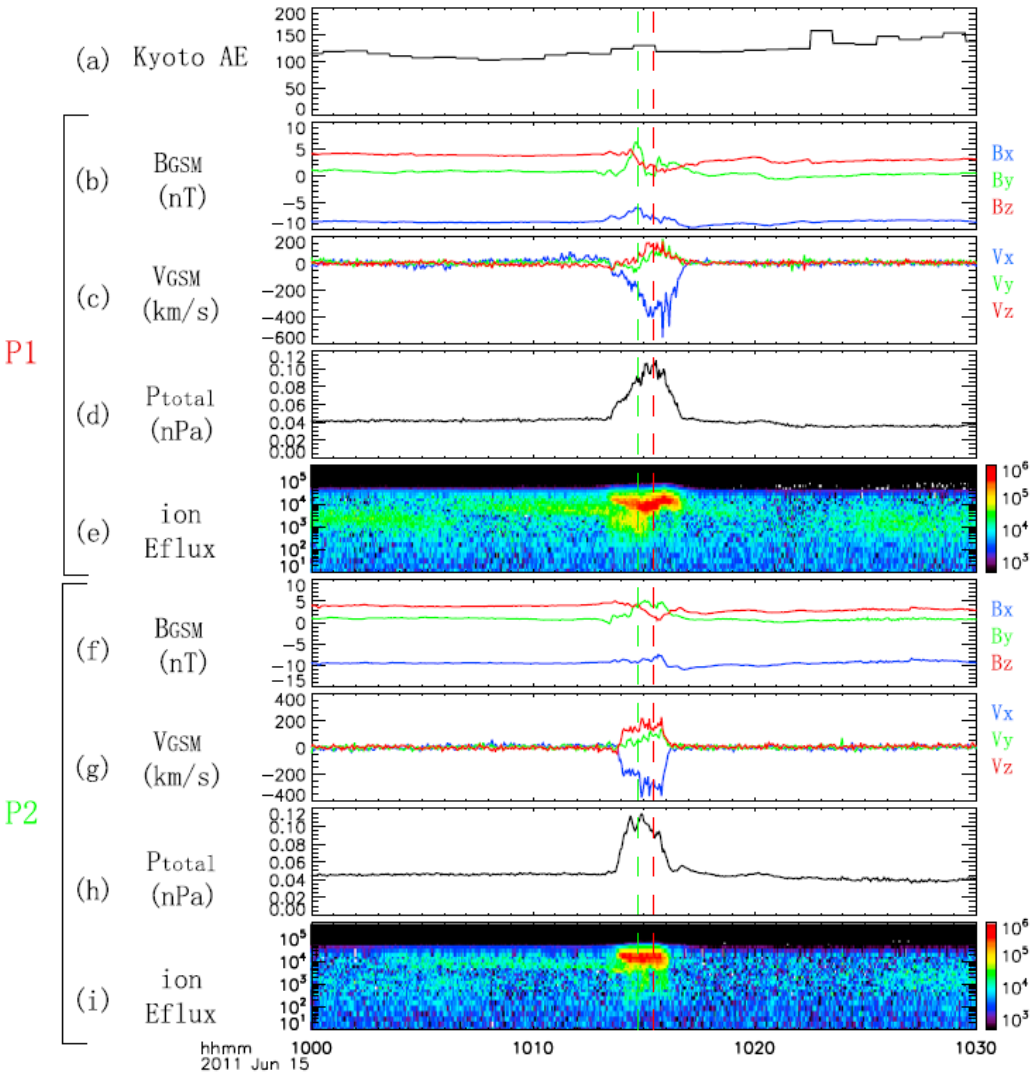

Figure 4.1 A typical plasmoid event observed by the two ARTEMIS spacecraft, P1 and P2. From top to bottom are the (a) Kyoto AE index, (b–e) P1 observations, and (f–i) P2 observations. The spacecraft observations include the magnetic field and ion velocity (from ESA) in GSM coordinates, the total pressure (thermal and magnetic field pressure), and the ion energy flux spectrogram (from ESA and SST). Event times, as selected from my database using my stricter criteria at each reference spacecraft, are demarcated by vertical lines.

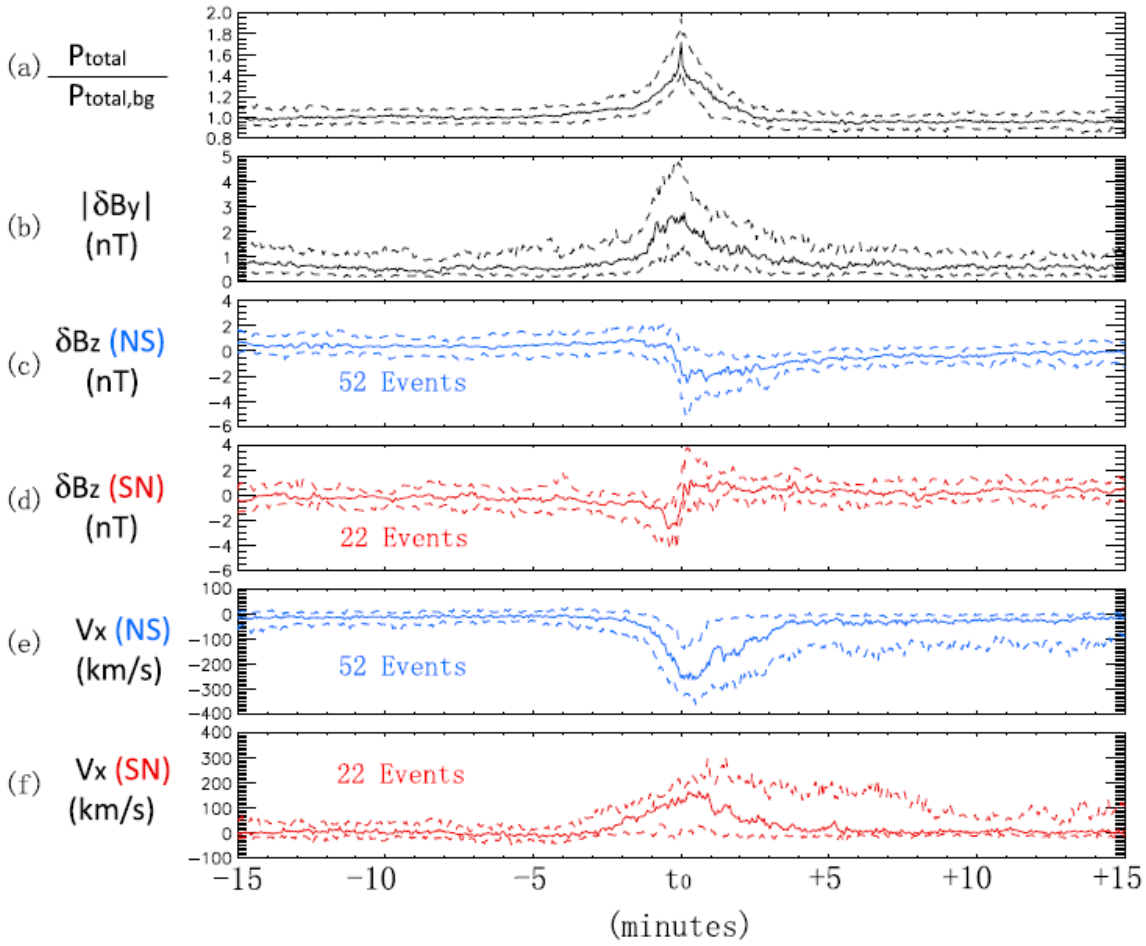

Figure 4.2 A superposed epoch analysis plot of variables from the 74 events selected by the reference spacecraft. Solid lines represent medians and dashed lines represent upper and lower quartiles. (a) Normalized total pressure enhancement. (b) Absolute value of the BY variation. (c and d) BZ variation in the north-south (NS) and south-north (SN) subset of the plasmoid database. (e and f) Velocity in the X_{GSM} direction for the NS and SN databases, respectively.

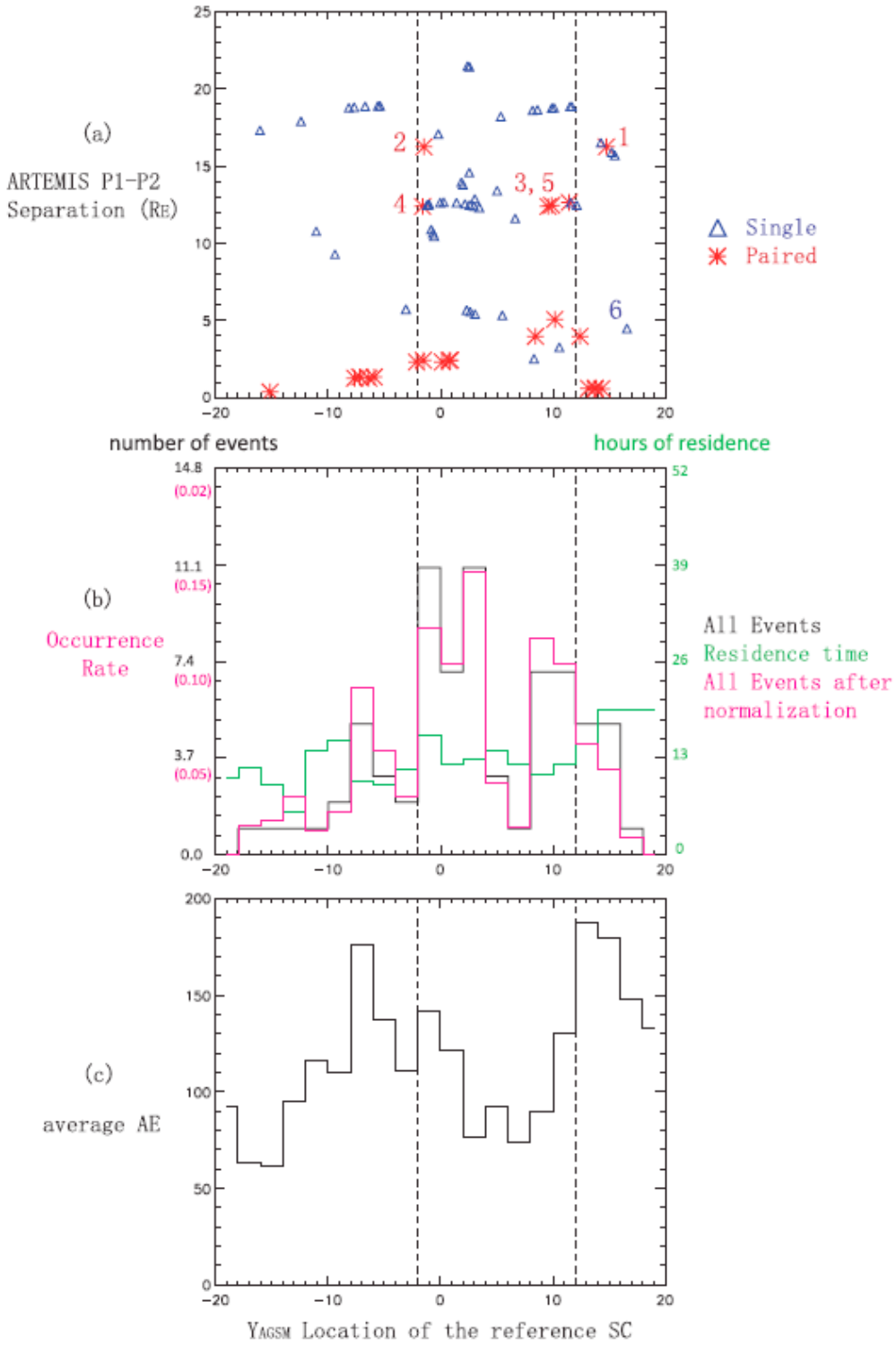
(a)
ARTEMIS P1-P2
Separation (RE)
Single
Paired
1
2
3, 5
4
6
number of events
hours of residence
(b)
Occurrence
Rate
All Events
Residence time
All Events after
normalization
(c)
average AE
YAGSM Location of the reference SC

Figure 4.3 Event distribution in the azimuthal direction (Y_{AGSM}). (a–c) The horizontal axis is the Y_{AGSM} location of the reference spacecraft. In Figure 3a, the vertical axis shows the separation of the two space- craft projections on the YZ_{AGSM} plane. Each red star or blue triangle represents one of the 74 events. In Figure 3b, the total number of events at different Y_{AGSM} locations is shown in black. The residence time of the spacecraft at different Y_{AGSM} locations is plotted in green. The normalized event distribution (total number divided by residence time) is shown in magenta. Figure 3c shows the average AE index for the times when the spacecraft was located at different azimuthal bins. The dashed lines at $Y_{AGSM} = 2\ R_E$ and $Y_{AGSM} = 12\ R_E$ represent the boundaries of the high occurrence rate region.

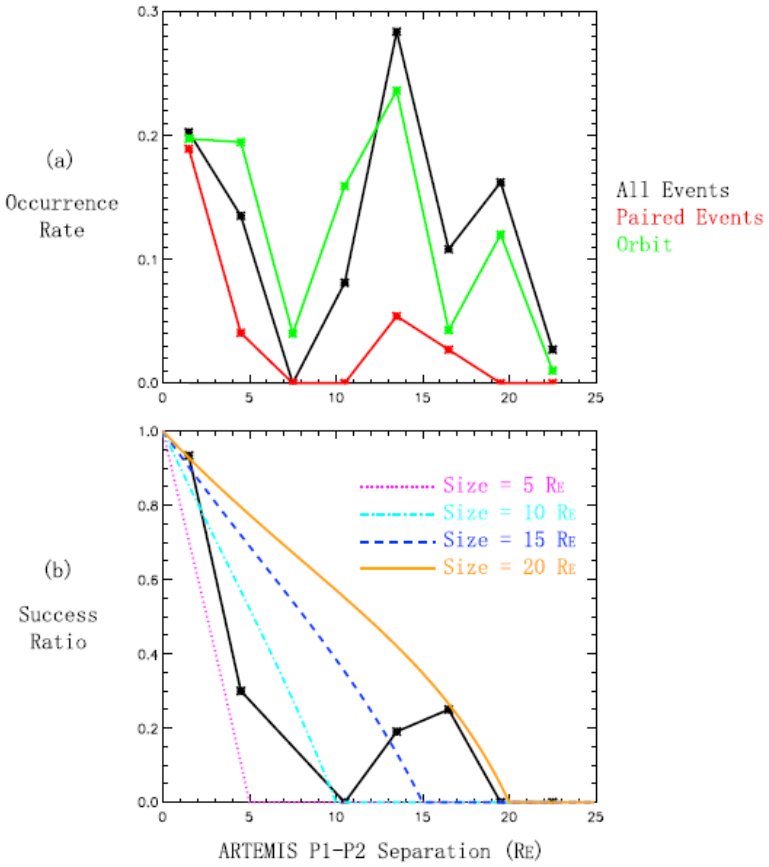

Figure 4.4 (a) Distribution of plasmoids, orbit residence time, and (b) paired events occurrence rate (success ratio) plotted against the separation between the two spacecraft in the YZ_{AGSM} plane. The black line in Figure 4.4a is the normalized distribution of the total number of events (number in each bin divided by 74), and the green line represents the normalized distribution of spacecraft residence time (hours in each bin divided by 362 h) in each interspacecraft distance bin. The red line is the normalized number of events (divided by 74) during which the test spacecraft also observed plasmoids. The ratio between the red and the black lines in Figure 4a, plotted as the black line in Figure 4b, represents the probability that the test space- craft will observe the plasmoid captured by the reference spacecraft. The four color curves represent the ideal success ratios calculated from a model (Appendix A).

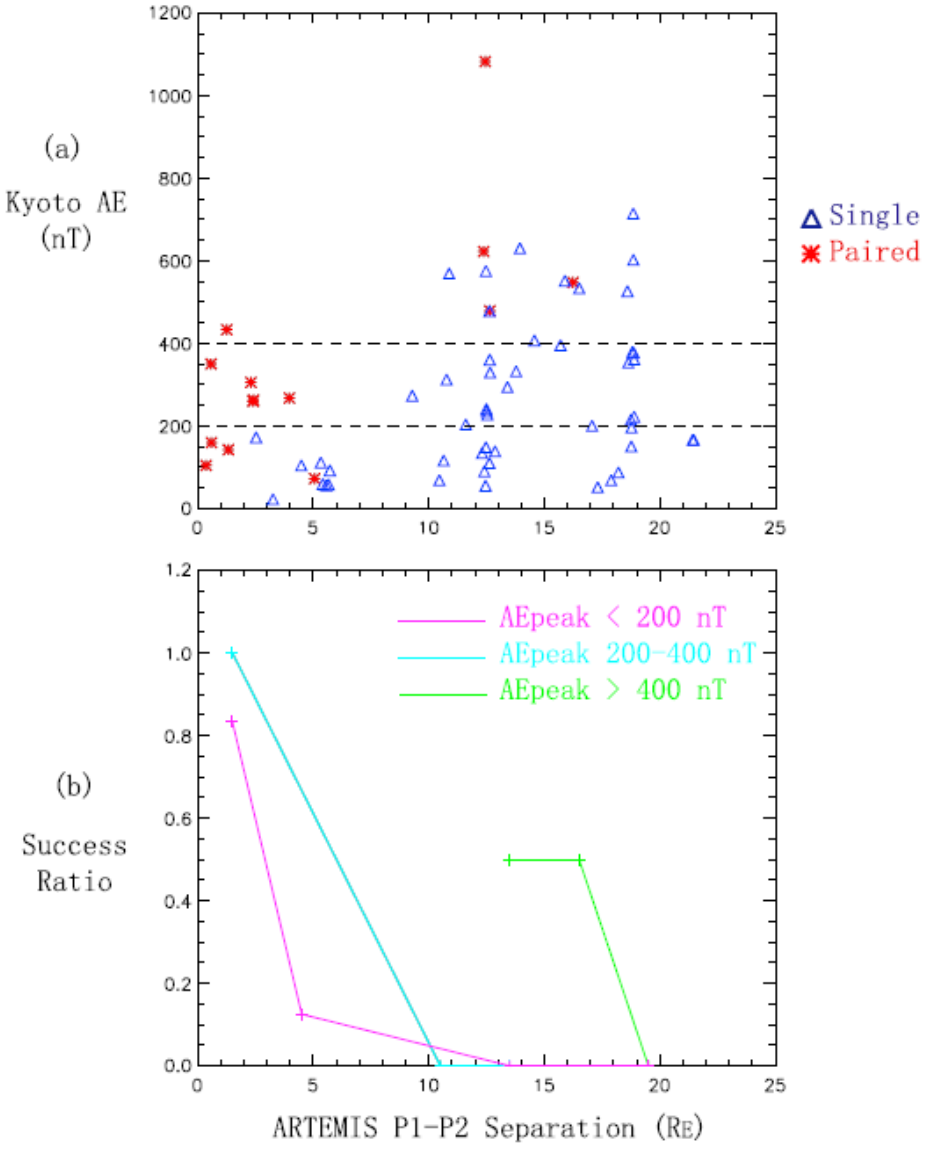

Figure 4.5 (a) The Kyoto AE index versus spacecraft separation for each event. Red stars and blue triangles represent the same events as in Figure 4.2a. Note that sometimes two events overlap and are shown as one point in this figure. For example, this was the situation for the 20 December 2010 case (marked here as 1 and 2) also shown in Figure 4.6. (b) The observed success ratios of the three subgroups distinguished by different Kyoto AE-index ranges.

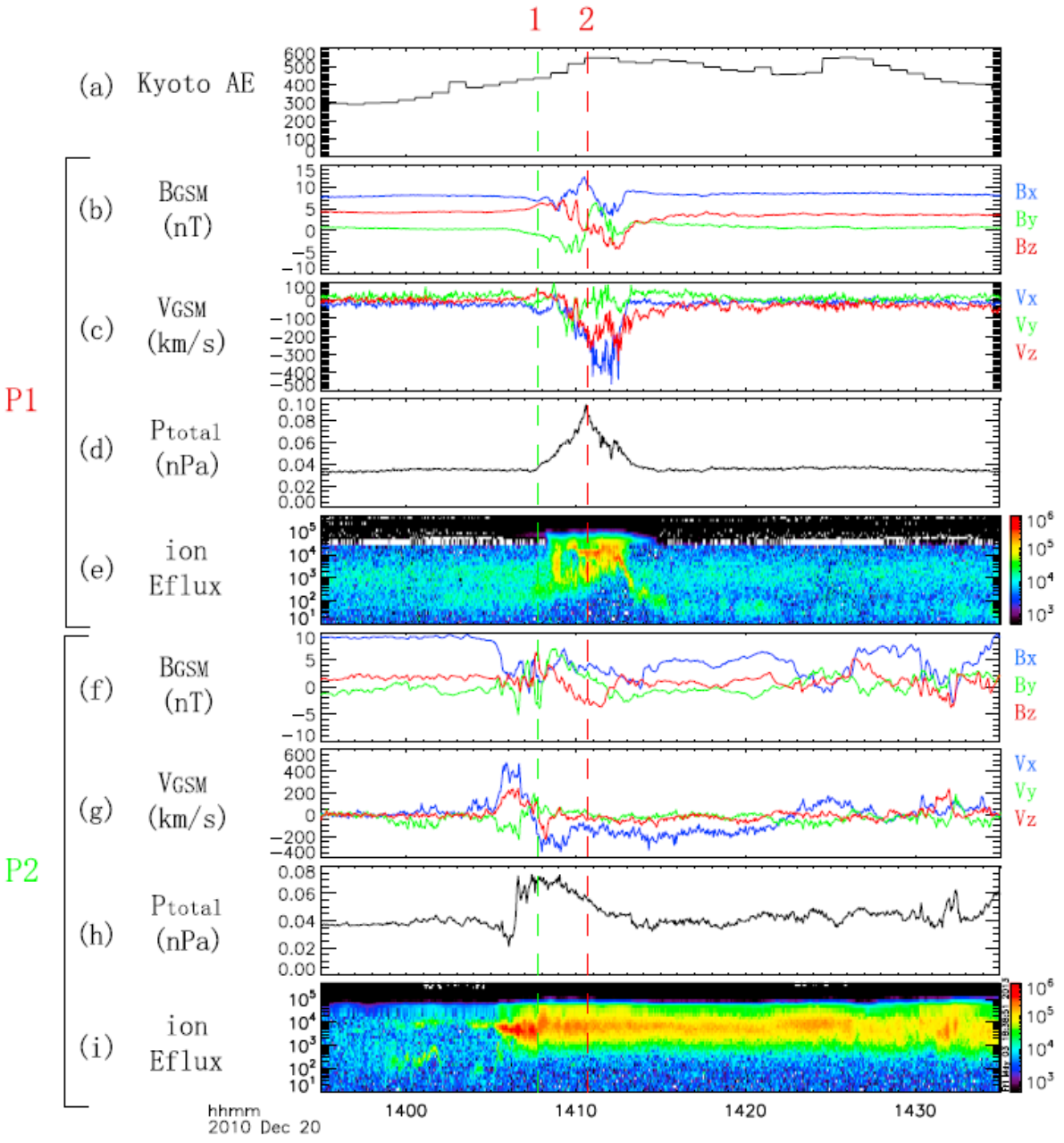

Figure 4.6 An plasmoid (two plasmoid events, #1 and #2) observed by both P1 and P2 when they were widely separated. The format is the same as in Figure 4.1.

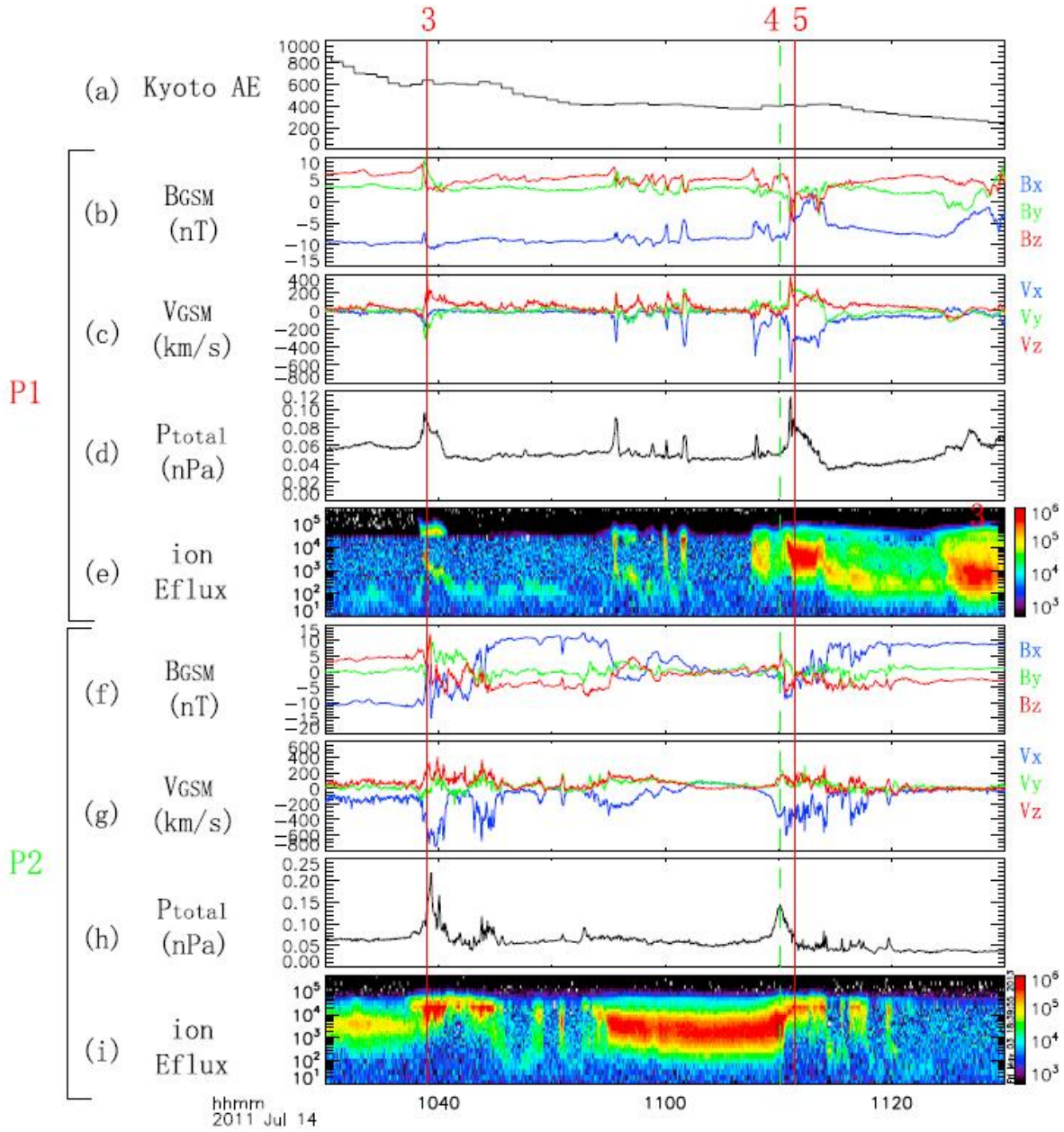

Figure 4.7 Two plasmoids (three plasmoid events, #3, #4, and # 5) observed by both P1 and P2 at large separations. The format is the same as in Figure 4.1.

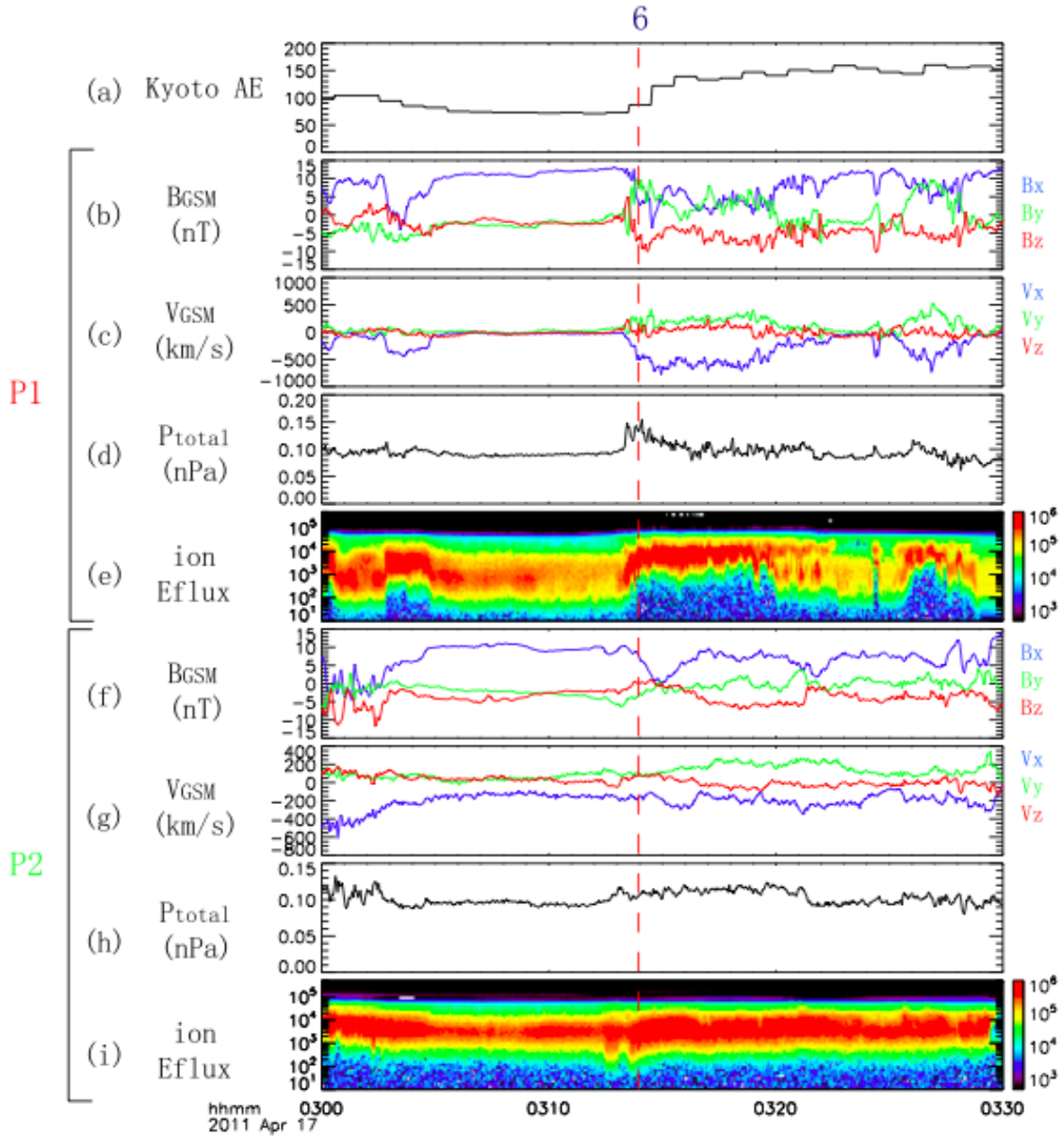

Figure 4.8 A plasmoid (one plasmoid event #6) observed by only P1, even though P2 was just 3 R_E away. The format is the same as in Figure 4.1.

CHAPTER 5 Plasmoid Growth and Expulsion Revealed by Two-Point ARTEMIS Observations

On 12 October 2011, two ARTEMIS probes, in lunar orbit ~9 R_E north of the neutral sheet, sequentially observed a tailward-moving, expanding plasmoid. Their observations revealed a multilayered plasma sheet composed of tailward-flowing hot plasma within the plasmoid surrounded by earthward-flowing, less energetic plasma. Prior observations of similar earthward flows ahead of or behind plasmoids have been interpreted as earthward outflow from a continuously active distant-tail neutral line opposite an approaching plasmoid. No evidence of active distant neutral line reconnection was observed by the probes, however, as they traversed the plasmoid's leading and trailing edges, penetrating above its core. We suggest an alternate interpretation: compression of ambient plasma by the tailward-moving plasmoid proper propels the plasma lobeward and earthward, i.e., above and below the plasmoid proper. Using the propagation velocity obtained from timing analysis, we estimate the average plasmoid proper size in its propagation direction to be 9 R_E and its expansion rate to be ~7 R_E /min at the observation locations. This observation of plasmoid expansion made at the plasmoid boundary is interpreted as plasmoid growth in both the X_{GSM} and the Z_{GSM} directions due to near-Earth-neutral-line reconnection on closed plasma sheet field lines. The velocity inside the plasmoid proper was found to be nonuniform; the core likely moves as fast as 500 km/s, yet the outer layers move more slowly (and in the reverse direction). The absence of lobe reconnection, in particular on the earthward side, suggests that plasmoid formation and expulsion both result from closed plasma sheet field-line reconnection.

5.1 Introduction

In the study of quasi-stagnant plasmoids, *Nishida et al.* [1986] proposed that if magnetic reconnection does not proceed to the lobes, the resultant plasmoid would be "trapped" within closed field lines. In such a case, background earthward convective flow from the DNL (assumed to be active) would oppose tailward flow from the NENL [*Nishida et al.*, 1986; *Moldwin and Hughes*, 1994; *Machida et al.*, 2000]. When the DNL is dominant, the entire structure, including the NENL and the plasmoid, would be swept earthward [*Slavin et al.*, 2003; *Eastwood et al.*, 2005]. Statistical studies have shown that the DNL is located at $X_{GSM} \sim -100\ R_E$ *[Zwickl et al.*, 1984; *Slavin et al.*, 1985; *Moldwin and Hughes*, 1992a], and tailward-propagating plasmoids in the mid-tail regions (earthward of that distance) have an average bulk speed of ~ 600 km/s [*Scholer et al.*, 1984; *Richardson et al.*, 1987b; *Ieda et al.*, 1998].

Statistical studies of plasmoids and TCRs based on ISEE 3, IMP 8, GEOTAIL, and CLUSTER observations in different magnetotail regions [*Richardson et al.*, 1987b; *Moldwin and Hughes*, 1992a, 1994; *Slavin et al.*, 1993; *Ieda et al.*, 1998; *Slavin et al.*, 2003, 2005] have revealed some aspects of plasmoid evolution. Plasmoids in the distant tail are reported to be larger both in Y_{GSM} [*Ieda et al.*, 1998] and X_{GSM} [*Slavin et al.*, 2003] than those in the near-Earth region. Fully formed plasmoids accelerate from near-tail (i.e., $-30\ R_E > X_{GSM} \geq -50\ R_E$) to mid-tail (i.e., $-50\ R_E > X_{GSM} \geq -100\ R_E$) regions [*Ieda et al.*, 1998; *Machida et al.*, 2000] and decelerate from mid-tail to distant-tail regions (i.e., $-100\ R_E > X_{GSM} \geq -200\ R_E$) [*Ieda et al.*, 1998]. Distant-tail plasmoids have higher density but temperatures similar to [*Ieda et al.*, 1998] or lower than [*Moldwin and Hughes*, 1992a] mid-tail plasmoids.

The mechanism of plasmoid expansion after ejection is not well understood. Early researchers [e.g., *Richardson et al.*, 1987b] expected that a plasmoid would expand adiabatically while

propagating down the tail. *Slavin et al.* [1989] suggested that a plasmoid contracts in X_{GSM} and expands in Z_{GSM} due to the higher tension of the field lines near the equatorial plane. In a statistical study by *Moldwin and Hughes* [1992a], however, plasmoids observed at different locations down the magnetotail were shown to have constant size (the authors suggested that plasmoids remain stable after their release). Additionally, the internal electron energy (N_eT_e) of plasmoids remains constant with increasing distance downtail, as the density (N_e) increases and temperature (T_e) decreases proportionately. Based on the above, *Moldwin and Hughes* [1992a] suggested that as a plasmoid propagates tailward, cool ambient plasma will enter it, so a balance between the plasmoid and the ambient plasma is maintained. Based on earlier TCR observations showing that corresponding (remotely-sensed) plasmoids propagate in groups of two or more [*Slavin et al.,* 1993], *Slavin et al.* [2003] suggested that an inverse reconnection between several small plasmoids near Earth may take place, producing the larger plasmoids eventually observed at the distant tail. Coalescence of small plasmoids in the X_{GSM} direction has also been seen in MHD simulations [*Richard et al.*, 1989].

Because of the limitations of single-spacecraft observations, there are few direct observations of plasmoid growth or expulsion. In a two-point case study of a TCR event using IMP-8 and Geotail observations, *Slavin et al.* [1999] suggested that the expansion rate of a "young" plasmoid located between X_{GSM} = -26 R_E and X_{GSM} = -44 R_E was 1.3 R_E /min in the X_{GSM} direction. In that study, the two spacecraft were separated by more than 7 R_E in all three directions. Other case studies of plasmoids using IMP 8 (X_{GSM} ~ -30 R_E) and ISEE 3(X_{GSM} < -200 R_E) observations have shown that once fully formed, plasmoids stabilize in size [*Moldwin and Hughes*, 1992b]. Given the wide separation between the spacecraft in the downtail, however,

it would be difficult to argue definitively that the same structures were observed at both observation sites.

To better understand plasmoid generation and evolution, I turn to observations from the two ARTEMIS spacecraft (probes P1 and P2) [*Angelopoulos*, 2010; *Sibeck et al.*, 2011], seeking plasmoids observed by probes with separations mostly in $X_{GSM.}$ The event selected for detailed study was particularly well suited for answering questions of growth and evolution, because the ARTEMIS probes were primarily separated in X_{GSM} (average separation $\delta X \sim 4.2\ R_E$), with no significant Y and Z separation ($\delta Y, \delta Z \leq 0.5\ R_E$). ARTEMIS P1 and P2 were located around $X_{GSM} = -60\ R_E$, near the center of the magnetotail. Both probes traversed the same plasmoid, which was apparently growing fast, having achieved a large tailward speed. Section 5.2 shows the ARTEMIS observations; Section 5.3 contains my interpretation. Ramifications of my results are discussed in Section 5.4.

5.2 Observation and Analysis

The plasmoid event I examined was observed at 0355 UT on 12 October 2011 when the two ARTEMIS probes, P1 (THB) and P2 (THC), were about 9 R_E above the nominal neutral sheet, the location of which was predicted by the *Tsyganenko* [1995] model. The probes were at (-60.5, -3.8, 6.4) R_E and (-64.7, -3.4, 6.65) R_E, respectively, in aberrated GSM coordinates, with a 4-degree aberration angle (Figure 5.1). Thus, they were separated by 4.2 R_E predominantly in the X_{GSM} direction. I analyze data from the Fluxgate Magnetometer (FGM) [*Auster et al.*, 2008], Electrostatic Analyzer (ESA) [*McFadden et al.*, 2008], and Solid State Telescope (SST) [*Angelopoulos*, 2008b]. The Kyoto AE index (Panel 5.2A) and Pi2 perturbations at station Bay Mills (Panel 5.2B) show onset signatures at around 0346 UT, about 8 minutes before the

plasmoid was observed by P1 (Figure 5.2C). Considering the 2-minute average time lag between NENL reconnection onset and the increase in the AE indices [e.g., *Angelopoulos et al.*, 2008a], I expect that slow reconnection at the NENL started at about 0344 UT, and a plasmoid was ejected tailward several minutes later.

As shown in Figure 5.3, a plasmoid was encountered by P1 and then P2. The total pressure is plotted at P2 (black) and at P1 (red); the latter plot is time-shifted by 48 s to give the best correlation between the two profiles. This time delay results in a tailward speed estimate of over 500 km/s, about 70% of the asymptotic Alfven speed calculated using lobe magnetic field strength (15 nT) and average plasma density in the ambient plasma sheet (0.2 particles/cm^3). Here the asymptotic Alfven speed is calculated as a maximum threshold by assuming that the magnetic energy stored in the first lobe field line can be fully converted to plasma kinetic energy. In addition to the pressure enhancement, all typical signatures of a tailward-propagating plasmoid were observed, including a clear "positive-then-negative" bipolar signature in B_Z (Panels 5.3A, 5.3E for P1 and P2, respectively) and heated plasma sheet plasma (Panels 5.3D and 5.3H) with β values (Panel 5.3I) exceeding 0.5 even near the plasma sheet boundary.

Instead of the tailward bulk flow expected from classical distant-tail plasmoid observations [*Baker et al.*, 1996], both probes observed an "earthward-tailward-earthward" variation in the V_X component of the flow within the plasmoid (Panels 5.3C, 5.3G). To distinguish between tailward- and earthward-flow regions, the velocity panels are shaded in light red (tailward) and light blue (earthward). Note that the positive V_X exceeding 100 km/s are observed at when probes first enter the structure with dense plasma sheet plasma. The ion omni-directional energy flux spectrograms (Panels 5.3D, 5.3H) reveal that the tailward and earthward flows are

composed of ions with different peak flux and average energy. Near the plasmoid center, where B_Z crosses 0 (~03:56:00 UT for P1 and ~ 03:56:45 for P2), the flow is tailward and the ions are more energetic (T_i =2.5 keV); on either side, the flow is earthward and the ions are of lower energy (T_i =1.5 keV). The ions in the tailward-flow (I refer to this region as the "plasmoid proper") and earthward-flow regions (I refer to this region as the "ambient compressed plasma sheet") are likely of different origin, giving the plasmoid a layered structure. I demarcate the two regions with lines (L1, L2, etc.) based on the sign of the flow's V_X component. It is worth noting that the peak magnitude of the V_X component of the ion velocity never exceeds 300 km/s, lower than the 500 km/s derived from the time delay of the pressure profile. This will be further discussed in the interpretation section.

The particle energy- and angular- distributions illustrate that the earthward and tailward flows represent two different plasma sheet populations. Figure 5.4 shows more detailed azimuthal and energy spectrograms of this event. The aforementioned populations are evident as separate, tailward (+/- 180 degrees) and earthward (0 degrees) ion populations in the azimuthal spectrograms (5.4A-C for P1 and 5.4H-J for P2, for ions of different energies). These panels, as well as the energy spectrograms for the earthward-propagating ions (near 0-degree pitch angle, Panels 5.4D and 5.4K for P1 and P2, respectively) and the tailward-propagating ions (near 180-degree pitch angle, Panels 5.4E and 5.4L), also demonstrate that the tailward population near the center of the plasmoid at each probe (0356 UT and 0358 UT, respectively) was more energetic than the earthward population on either side. At higher energies (30 to 50 keV, Panels 5.4A and 5.4H), duskward ions (-90 degrees) are always seen before field-aligned ions because of the remote-sensing effect of the approaching spatial boundary of a high-flux energetic ion layer (e.g.,

see *Richardson and Cowley*, 1985). When the probes entered the boundary of the tailward flow region (plasmoid proper), they observed that ions with higher energy arrived earlier than those with lower energy (Panel 5.4E). The energy dispersion signature is less clear, however, for the first appearance of earthward flows upon plasma sheet entry and for flows at the edges of the earthward population trailing the plasmoid proper. The observed energy dispersion can be explained by the time-of-flight effect or the velocity-filter effect (e.g., *Richardson and Cowley*, 1985); The latter is caused by the cumulative effect of enhanced equatorward convection along the particles' path from their source to the probe, even though the motion of the field lines locally is lobeward. Both effects indicate an energetic particle source earthward of the observation point, which is consistent with an NENL source acting within closed plasma sheet field lines to generate the tailward plasma population.

Electron pitch-angle distributions (Panels 5.4F and 5.4M) reveal cigar-type or near-isotropic distributions in the bulk velocity plane (Panels 5.5A, 5.5C, 5.5D, 5.5E, 5.5F, 5.5G, 5.5H, 5.5J) throughout most of this plasmoid (plasmoid proper and ambient compressed plasma sheet) encounter. Exceptions (Panels 5.5B and 5.5I) showing unidirectional flux occurred when the probes crossed flux tubes connected to the Moon, i.e., when d, the distance of each field line (assumed straight) to the lunar center, was less than one lunar radius ($d \leq 1\ R_L$ in Panels 5.4G and 5.4N). Such blockage of field-aligned superthermal electrons from the lunar direction has been reported previously [e.g., see *Halekas et al.*, 2012]. Outside these lunar connection periods, there was no evidence of unidirectional electron streaming but near-isotropic electron distributions.

Table 5.1 summarizes the evolution of the multi-layered plasmoid structure. I demarcate the plasmoid layer (section) boundaries using the flow reversals indicated by vertical dotted lines in Figure 5.3, Panels C and G. The leading section is L1-L2; the center section is L2-L3; and the trailing section is L3-L4. Comparison of these sections in Panels C and G shows that in Panel G, the leading section was reduced in duration, while the center section increased. Considering an average propagation velocity of 500 km/s, I estimate the cross-sectional lengths of the sections in the X_{GSM} direction directly from the observed time intervals (see listing in columns 3 and 4 of Table 5.1). As it propagated from P1 to P2, the center section expanded from 5 R_E to 12 R_E in the X_{GSM} direction. I interpret this expansion as plasmoid growth caused by an active NENL, which provides energy and newly reconnected magnetic flux to the plasmoid proper as it moves tailward. The asymmetric expansion, however, is not consistent with continuous reconnection followed by flux transport. To understand this further, I examine time-delay velocities of different plasmoid sections separately.

The time-delay velocities of various sections in Table 5.1, calculated based on the time differences between P1 and P2 observations of each boundary, reveal the velocities of different parts of the plasmoid. Time delays for each characteristic time pair are also shown in Table 5.1, Column 6; the results of propagation velocities are shown in Column 7. The large discrepancies between the velocities of different parts of the plasmoid reveal significant temporal evolution. The leading edge of the tailward section was observed to have an apparent velocity of ~900 km/s at ~ 03:55:45 to 03:56:14 UT; the trailing edge was observed moving at 200 km/s about one minute later (03:56:46 to 03:58:44). The 700 km/s difference in the apparent velocity of the two

sides of the plasmoid further validates the plasmoid's significant expansion during its fast (~500 km/s based on the pressure peak) tailward propagation.

Because the probes crossed the lobe-plasma sheet boundary interface upon entry into the plasma sheet, remote sensing of energetic ions (assumed to be protons) at the time of entry can provide independent estimates of plasma sheet orientation and expansion velocity [*Richardson and Cowley*, 1985; *Angelopoulos et al.*, 2008a]. For an active DNL, this velocity is a combination of the actual plasmoid convective speed and the apparent velocity due to the addition of newly reconnected flux tubes to the plasma sheet. Comparison of the velocity from the remote sensing technique with the measured convection velocity therefore provides an independent way of testing DNL reconnection activity at the time of boundary traversal. Figure 5.6 shows the 30 to 50 keV energetic ion azimuthal spectrograms from the two equatorial detectors of the SST instrument (the ones closest to the spin plane, i.e., closest to the GSE equator, with elevations centered at θ = 52 and 128 degrees in despun probe coordinates) and their fields of view of about 37 degrees [See *Angelopoulos*, 2008b for a description of the DSL (De-spun, Sun-pointing, L-vector) coordinate system and SST mounting]. Note that the P1, P2 spin axes are pointing near ecliptic south. For this event, the angle between Z_{GSE} and Z_{GSM} is about 20 degrees, smaller than the resolution of data collection (37-degree range). In a practical way, I consider $X_{DSL} \sim X_{GSM}, Y_{DSL} \sim -Y_{GSM}$ and $Z_{DSL} \sim -Z_{GSM}$ approximately. The particles observed first (e.g., at 0354 UT at P1, θ = 52 degrees, Φ = -90 degrees, Panel 5.6C) were moving approximately duskward. About 20 sec later, both duskward and dawnward particles were observed. Similar patterns are also shown in Panels 5.6D, 5.6G, and 5.6H. The similarity of the patterns in Panels 5.6C and 5.6D (also Panels 5.6G and 5.6H) indicates that the boundary normal is approximately

along the Z_{GSM} direction. Thus, the approaching boundary, a plane containing the magnetic field, is roughly parallel to the XY_{GSM} plane. The plane propagated two ion gyro radii northward between the first detection of duskward ions and the first detection of dawnward ions, as illustrated in Figure 5.7. From the azimuthal plots in Figure 5.6, I find duskward (marked by the $\Phi_B = -90^\circ$ lines) ions arriving about 15-20 seconds earlier than dawnward ions (marked by the $\Phi_B = +90^\circ$ lines), which suggests a boundary propagation velocity of 150 to 200 km/s in the Z_{GSM} direction, considering the 40 keV ion gyro radius is 1500 km. This is consistent with the measured local perpendicular plasma velocity of 150 to 200 km/s in the Z_{GSM} direction at that boundary (Panels 5.6B and 5.6F).

5.3 Interpretation

The aforementioned observations are consistent with a tailward-moving plasmoid embedded in the plasma sheet, as shown in Figure 5.8a. The relative trajectories shown in Figure 5.8 are consistent with the magnetic field observations [*Borg et al.*, 2012]. Formed by plasma sheet (but not necessarily lobe) reconnection at the NENL, the plasmoid is propelled tailward. This tailward propulsion opposes the curvature force from the closed plasma sheet field lines ahead (tailward) of the plasmoid. As a result, the ambient plasma on closed plasma sheet flux tubes ahead of the plasmoid is compressed by the approaching hot plasma of the reconnected flux tubes. As the plasmoid approaches, the ambient plasma near the magnetic equator is accelerated lobeward along the magnetic field (and possibly also sideways) and pushed around the plasmoid proper, i.e., earthward, as shown by the blue arrows in Figure 5.8a. Similar plasma behavior has been shown in theoretical models [*Semenov et al.*, 1984; *Kiehas et al.*, 2009]. Thus, a probe encountering an approaching plasmoid is engulfed first by the earthward flow within the ambient

compressed plasma sheet and then by the hot tailward-streaming plasma inside the plasmoid proper. On exit from the plasmoid proper, the probe again encounters the ambient plasma sheet earthward of it. Based on the data presented in Figure 5.3 and the pertinent discussion, both probes passed through the northern part of such a multi-layered structure, including the plasmoid proper and its ambient compressed plasma sheet.

Similar multi-layered plasmoid structures observed previously have been interpreted in the framework of multiple-reconnection (see Figure 5.8b). In this interpretation, the earthward flow is considered as an earthward outflow from an active DNL, where the only evidence for the active DNL is earthward-streaming ions (20-36 keV) in the plasma sheet boundary layer (PSBL) [*Nishida et al.*, 1986]. However, field-aligned ion beams in the PSBL are not necessarily related to magnetic reconnection [*Grigorenko et al.*, 2011; *Zhou et al.*, 2012]. In this study I examine this hypothesis further, seeking evidence of DNL reconnection in my event.

There are two types of ion beams in the PSBL, which are defined based on different electron distributions observed along with the ion beams. Type-I ion beams are always observed along with near-isotropic electrons, indicating that the ion beams' acceleration source is at closed magnetic field lines [*Grigorenko et al.*, 2011]. Type II ion beams are observed along with typical electron distributions at magnetic separatrices - cold electrons (<1 keV) moving towards the acceleration source and hot electrons (>1 keV) moving away from it [*Nagai et al.*, 2001; *Grigorenko et al.*, 2011]. Though a plasma sheet boundary layer without an active distant neutral line is not clearly defined in physics, I consider the PSBL as the boundary layer (if any) between the plasma sheet and the lobe region. In this event, both probes traverse the boundary between the plasma sheet and the lobe region. If there is a PSBL layer in between, a reconnection-related

electron distribution should be observed there. Throughout the entire plasma encounter period, however, the observed electron distributions are near-isotropic (shown in Figure 5.5), which indicates that the observed ion beams are not related to active DNL, and typical PSBL signatures were not observed in this event.

On the other hand, as illustrated in Figure 5.5, I estimated the plasma sheet boundary expansion velocity by a remote sensing technique applied on energetic (30keV-50keV) ions [*Richardson and Cowley*, 1985]. As described in detail in the analysis section, the agreement between the estimated boundary expansion velocity and the local plasma convection velocity indicates that the DNL was inactive. Thus, in my case, neither of these methods revealed DNL activity at the time of boundary layer crossings.

The total pressure began to increase gradually about 40 s before probe entry into the plasmoid, which indicates the compression between plasmoid and ambient plasma. Similar pressure profiles have been seen ahead of both tailward plasmoids [*Nishida et al.*, 1994] and earthward-moving dipolarization fronts [*Chapter 3*; *Runov et al.*, 2011]. This gradual pressure increase has been interpreted as resulting from compression at the interface between the approaching structure and the ambient plasma sheet plasma. According to simulations, this compression produces a pair of fast waves standing ahead of and behind this tailward-moving plasmoid core [*Abe and Hoshino*, 2001]. A localized total pressure increase at the pre-plasmoid plasma sheet is clearly seen (at L1-L2 in Figure 5.3) in my event.

Since there is no clear evidence of an active DNL, I favor the alternative scenario, shown schematically in Figure 5.8a. For this event, this compression is built up by the fast-moving plasmoid proper and the plasma sheet field line tension. The observed ambient plasma

compression ahead of the embedded plasmoid proper opposes the plasmoid's tailward propagation and accelerates the plasma up (and likely also sideways). In this scenario the tension force and the enhanced pressure ahead of the plasmoid proper results in the earthward flows observed ahead of (and by inference above) the plasmoid proper, at its leading and trailing sections.

Using the time delay of the total pressure profile at the two probes, I found a tailward speed (~500 km/s) faster than the measured ion flow speed at all plasmoid layers encountered by the two probes. The plasma speed at the plasmoid proper (~300 km/s) calculated from the particle distribution functions may not be the actual speed of the plasmoid's core, the portion nearest the equator. The plasmoid's core likely gives the plasmoid its apparent time-delay speed, 500 km/s. In other words, as the total pressure disturbance associated with field-line curvature from the passing plasmoid core is travelling downtail with the same speed as the core itself, the outer layers of plasmoid proper are sliding relative to the core and lagging behind it. Thus, the differential speed (shear) between the core and the ambient compressed plasma sheet (with earthward flow) is likely even greater than that measured by the probes crossing the outermost layers of the plasmoid proper.

The relative timing of magnetic field and plasma velocity signatures, summarized in Table 5.1, indicates an increase in plasmoid length along the tail. Figure 5.9 shows two stages of plasmoid evolution schematically. The two timings (035600UT and 035648UT) are chosen based on magnetic observations when B_Z is close to 0 and B_X achieves maximum simultaneously. Figure 5.9a shows the situation at ~ 0356UT, when P1 was inside the tailward-convecting plasmoid (light red region) and P2 was in the pre-plasmoid plasma sheet exhibiting earthward flow (light

blue region). Figure 5.9b shows the situation at ~035648UT, when P2 was inside the plasmoid and P1 was near the boundary between the post-plasmoid plasma sheet and the plasmoid itself. Based on the observed time delays, the expansion rate in the X direction is estimated to be ~7 R_E/min. The plasmoid cross-sectional length estimate is based on a constant propagation velocity of 500 km/s determined from the pressure profile time-delay at the two probes. Given the good agreement between the time-lagged pressure profiles in Figure 5.3F at all times during plasmoid passage, I expect this speed to be relatively stable for the duration of core passage. This expansion of the plasmoid proper resulting from plasma sheet reconnection happening at the NENL does not obviously change the magnetic curvature of the perturbed region, including the plasmoid proper, the outer layer, and the related TCR. Thus, the total pressure profile indicating plasma sheet field-line curvature remains stable within the short time of plasmoid propagation from P1 to P2.

The apparent expansion of the plasmoid's central portion, evidenced in traversal along the X_{GSM} direction by probes $9R_E$ away from the its center, might be misleading due to different probe trajectories through the plasmoid's X-Z cross-section. If that is true, the probe entering more deeply into the central plasmoid structure would cross a lengthier portion of the plasmoid proper. I first considered whether the apparent increase in plasmoid length could be caused by the positions of the two probes with respect to the magnetic equator. The probe closer to the neutral sheet should have crossed the plasmoid closer to its core and remained inside the plasmoid longer. If this is the situation, P2, which observed a longer plasmoid signature, should be closer to the neutral sheet and have larger β values. From the observations, however, P2 has slightly larger Z_{GSM} component and β values comparable to P1 observations. One could still argue that

since the Z_{GSM} position difference between the two probes is so small (about 0.2 R_E), a neutral sheet tilt about the Y_{GSM} axis (from a positive Z_{GSM} solar wind velocity component) could reverse the relative distances of P1 and P2 from the neutral sheet. Moreover, if the entire plasma sheet was moving upward during this period, the probes' relative trajectories through this plasmoid would also be tilted and thus traverse the plasmoid at different distances from the neutral sheet. Examining solar wind conditions using WIND data at 1 AU for 1 hour preceding plasmoid detection, I found the solar wind V_Z to be quite stable between -20km/s to 0km/s. Thus, the neutral sheet tilt should be no more than ~2 degrees in the $-Z_{GSM}$ direction. Even were there an upward plasma sheet velocity of ~10km/s due to flapping, the relative trajectory would only have a 3-degree maximum tilt angle, considering the fast plasmoid propagation velocity in X_{GSM} direction. Thus, I find no evidence that the apparent increase in plasmoid length was due to the two probes' traversals of the plasmoid at different distances from its core. Moreover, the observed peak-to-peak value of the magnetic field tilt angle on the X-Z plane did not change from the P1 to the P2 traversals. This further supports my argument that the plasmoid's XZ cross-sectional curvature did not change at the leading and trailing sides when crossed by the probes. By inference, the plasmoid did not deform significantly out of the plasma sheet in response to curvature forces in the $-X_{GSM}$ and $+Z_{GSM}$ directions. Since plasmoid growth involves proportional expansion in both the X_{GSM} and Z_{GSM} directions, the actual plasmoid growth rate close to the equator should be smaller than the estimated 7 R_E/min.

No signature of lobe reconnection was found (streaming particles from NENL), although plasma sheet reconnection could still be active at the NENL, as evidenced by the velocity-filter effect or time-of-flight effect as the probes entered the tailward-moving plasmoid layers. This suggests

that NENL reconnection had not proceeded to the lobe field lines yet, although the plasmoid had already achieved a high tailward propagation speed (over 500km/s). Without lobe reconnection, a quasi-stagnant plasmoid can achieve a speed of 300km/s [*Nishida et al.*, 1986]. In this event, I extend the possibility of "no lobe reconnection" to a fast-propagating plasmoid. To further test this interpretation, I examined flux transport by the curved portion of the plasmoid during the interval of increased total pressure (higher pressure is evidence of increased field-line curvature force in the $-Z_{GSM}$ direction required to balance the pressure gradient force in the $+ Z_{GSM}$ direction). First, within the period of total pressure enhancement (shown in Figure 5.3, Panel 5.3I), the northward flux transport in the tailward plasma sheet measured by both P1 and P2 is well balanced by the southward flux transport. Second, the typical magnetic flux stored in the northern plasma sheet (2.5×10^6 Wb/R_E, assuming a B_X of 20nT and a thickness of 3Re at a distance of 25 R_E) is more than sufficient to provide the observed closed flux within the plasmoid (1.5×10^6 Wb/R_E, a comparison to solar wind flux input is addressed in Appendix B), which is the integral of the flux transport rate (V_XB_Z-V_ZB_X) over time. Both of the above results support the scenario that the plasmoid was formed by closed plasma sheet reconnection; lobe reconnection was not necessary for plasmoid ejection.

This interpretation assumes that the plasmoid was embedded in the plasma sheet and propagated tailward while compressing and possibly stretching magnetic field lines ahead of it. This stretching increases the tension force acting against the plasmoid, which should decelerate it. Alternatively, from a 3-D scheme [*Hughes and Sibeck*, 1987], interchange instability could break the plasmoid (flux-rope) cross-tail into little pieces. If, however, this plasmoid were already localized in Y_{GSM} [*Ieda et al.*, 2008] rather than extended across a large portion of the tail, it

would continue propagating tailward by diverting the ambient plasma upwards and sideways. In this case, there would be no need for interchange instability to break it up. Therefore, if a plasmoid is ejected tailward without lobe reconnection, it should have been initiated as a localized blob or broken into smaller blobs after interaction with ambient plasma.

In both scenarios shown in Figure 5.8 (active and inactive DNL), plasmoid ejection is caused not by tailward forces from lobe field-line reconnection, but by the balance between the magnetic tension forces resulting from NENL (plasma sheet) reconnection and the curvature force from the ambient plasma sheet (Fig. 5.8a) or newly reconnected plasma sheet (Fig. 5.8b [*Nishida et al.*, 1986]) flux tubes. Without lobe reconnection, plasmoid formation can be directly related to abrupt, localized near-Earth reconnection on closed plasma sheet field lines. Hence plasmoid should be localized originally in the near-Earth region. Since there is a one-to-one correlation between the onset of large isolated substorms and distant-tail plasmoids observed by single spacecraft [*Hones*, 1984; *Slavin*, 1984; *Moldwin and Hughes*, 1993; *Nagai et al*., 1994], plasmoids are expected to attain a large scale in Y_{GSM} in the distant-tail [*Ieda et al*., 1998]. If tailward-moving, embedded, localized plasmoids such as the one observed in this study coalesce, what are the conditions for such a coalescence process? Since it is likely that each localized reconnection impulse produces a localized plasmoid, even when localized mid-tail plasmoids are not necessarily related to large-scale isolated substorms, coalescence of a sufficient number and size of plasmoids may produce good correlation between distant-tail plasmoids and large, isolated substorms. More case studies and modeling are required to answer these questions, but such studies are now within reach, thanks to the availability of ARTEMIS data.

5.4 Conclusions

Two-point ARTEMIS probe observations of an expanding, tailward-moving plasmoid were used to determine plasmoid expulsion and evolution. The ARTEMIS probes, separated by ~ 4 R_E (P2 tailward of P1) predominately along the X_{GSM} direction, were located near lunar orbit at X_{GSM} ~ -60 R_E. Both probes observed a similar multi-layered plasma sheet with tailward-flowing hot plasma wrapped in a layer of earthward-flowing, cooler plasma.

Since no evidence of active distant neutral line reconnection was found, the earthward plasma flow cannot be interpreted as reconnection outflow. An alternative interpretation that does not require active distant-tail reconnection was therefore favored: the plasmoid was formed by plasma sheet reconnection at the near-Earth neutral line and was ejected tailward without lobe reconnection. The tailward-moving plasmoid core embedded in closed plasma sheet field lines stretched the magnetic field lines ahead of (tailward) of it and compressed the ambient plasma sheet plasma. This compression resulted in diversion of ambient plasma around the plasmoid core and earthward flow in the layer surrounding the plasmoid proper.

The two-point observations allow us to estimate the plasmoid propagation velocity as well as the velocities of its leading and trailing boundaries. The propagation velocity is approximately 500 km/s (which could be achieved without lobe field reconnection since it is only 0.7 times the asymptotic Alfven speed). The velocity difference (by timing) of the leading and trailing boundaries reveals a plasmoid growth rate of 7R_E/min. Although this expansion takes place after the plasmoid has achieved a high propagation speed, it occurs during plasmoid formation, as NENL reconnection has not completely reached the tail lobe.

This event extends my understanding of plasmoid formation and propagation: First, the plasmoid is growing rapidly as it propagates tailward at high speed. Second, the plasmoid is still growing

as it expands in the X_{GSM} direction. Third, lobe reconnection is not necessary for plasmoid downtail ejection. In other words, as consistent with earlier observations (*Aikio et al.*, 1999), an ejected plasmoid may still show signatures in the Earth's ionosphere well equatorward of the polar cap boundary. Fourth, for this type of event, the earthward flow observed before and after the plasmoid can be interpreted as resulting from compression of the ambient plasma by the tailward-propagating plasmoid, rather than as ejecta from an active DNL.

This event also suggests that if plasmoids are localized in the Y_{GSM} direction rather than extended across the magnetotail during formation, they can be ejected farther tailward without lobe reconnection by diverting the ambient plasma sheet field lines sideways. If they are not localized during formation, they will likely become so because of interchange between tailward-moving flows and the ambient plasma. The further evolution and fate of embedded plasmoids similar to the observed one is an interesting unsolved problem. With the advantage of two-point observations provided by ARTEMIS, more evidence of this process can be found using case and statistical multipoint studies.

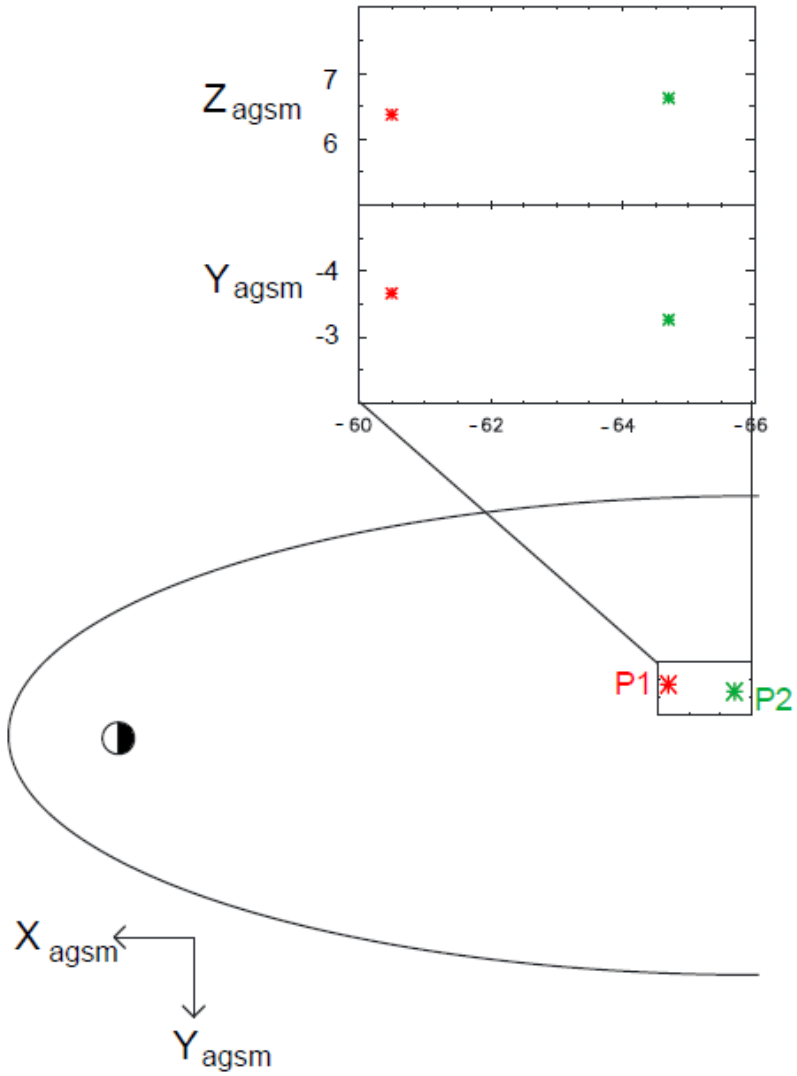

Figure 5.1 Probe locations (in aberrated GSM coordinates) for the event under study.

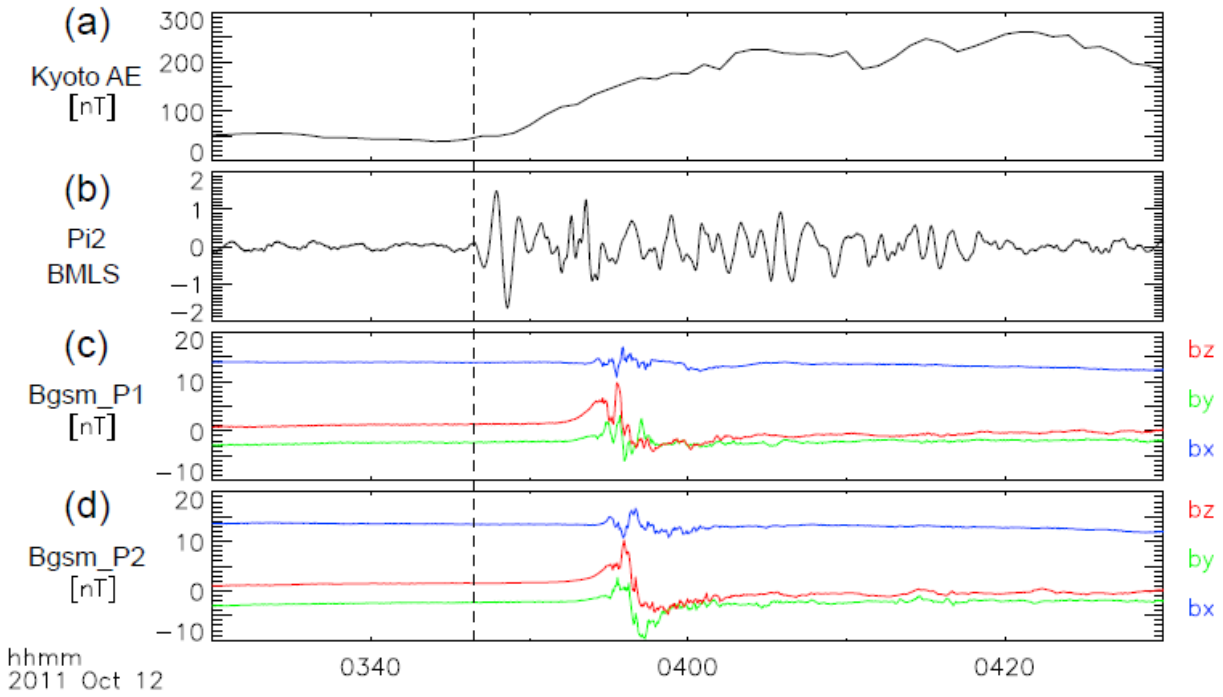

Figure 5.2 The correlation between substorm on Earth and plasmoid observation by P1 and P2 is shown briefly. Panel A is the Kyoto-AE index increasing from 50 to 200 nT; Panel B is Pi2 pulsation detected by Bay Mills ground station; Panel C and D are magnetic field variations observed by P1 and P2, indicating a plasmoid passage.

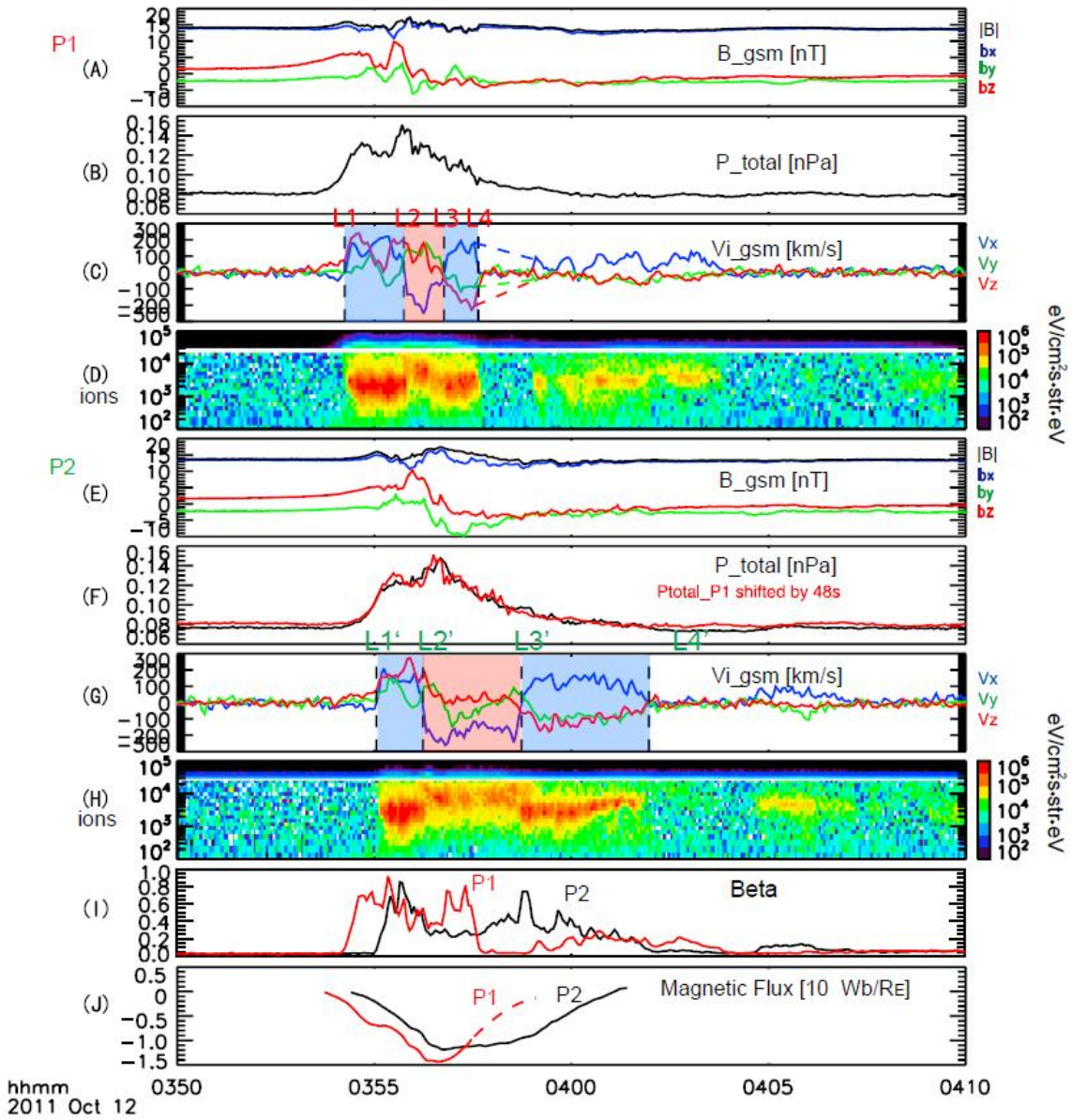

Table1	P1 observation time	Time interval between two P1 Tcharacter s	P2 observation time	Time interval between two P2Tcharacter s	P1-P2 time delay	Time-delay Velocity
L1. Vx starts positive	03:54:15		03:55:03		48 s	560km/s
L2. Vx turns to negative	03:55:45	90 s	03:56:14	71 s	29 s	920km/s
L3. Vx backs to positive	03:56:46	61s	03:58:44	150s	118 s	230 km/s
L4. Vx goes to zero	03:57:38	52s	04:01:58	194 s	220 s	120 km/s

Figure 5.3 Magnetic field and plasma data measured at P1 (THB, Panels A-D) and P2 (THC, Panels E-H), their β values (in Panel I), together with the estimated magnetic flux transport (Panel J, P1 estimation in red and P2 estimation in black). From top to bottom: magnetic field, total pressure, ion bulk velocity from ESA, and energy-time energy flux spectrogram for ions. All vectors are in GSM coordinates, and X,Y, and Z are blue, green, and red lines, respectively. The total magnetic field is overplotted in Panels A and E in black. In Panel F, the total pressure of P1 (from Panel B) is shifted by 48 s and overplotted in red. The plasma data were assembled by two different instruments: ESA measures 5-25keV ions, and SST measures particles with energies >30 kev. The two distinct ion populations are indicated in light blue and light red in the velocity Panels (C and G): the blue region has earthward bulk velocity and the red has tailward velocity. The four boundaries of the colored regions are defined based on the velocity transitions and marked by dashed lines. Table 5.1 presents an analysis of these characteristic times. The three time intervals defined by the four characteristic times listed in rows 3 and 5 of Table 5.1 can be related to the cross-sectional lengths of each sub-structure (leading portion, center portion, and trailing portion). Panel I represents the β values of P1 (in red) and P2. In Panel J, the flux transport during the time of total pressure enhancement is estimated based on ion bulk velocity and magnetic field measurements (transportation rate $E_y = V_X B_z - V_z B_x$). The dashed lines in P1 velocity (Panel C), which correspond to the dashed lines in flux transport estimation (Panel I), represent the interpolation results on the velocity gap when the flow data cannot be obtained due to low particle measurements.

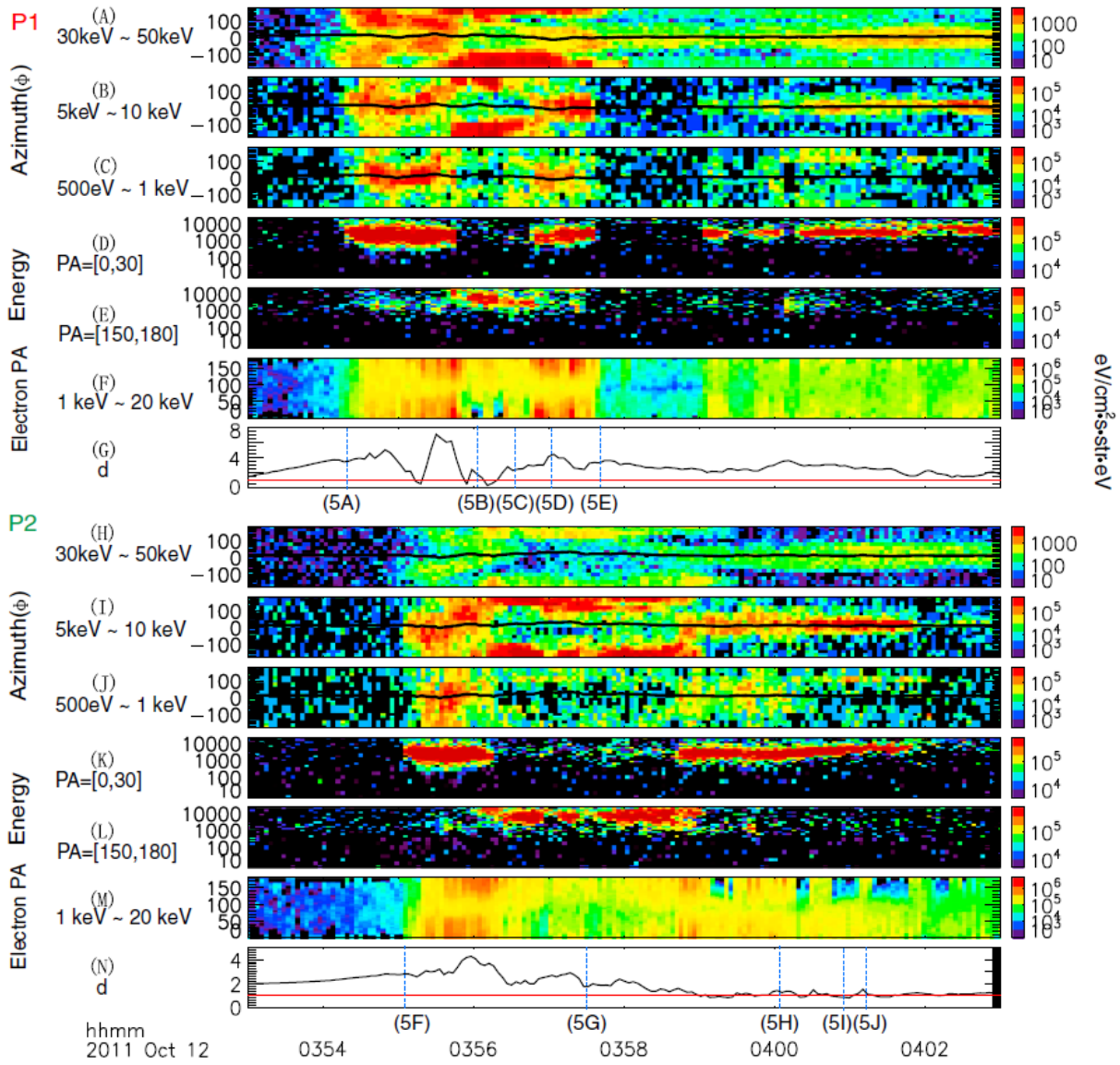

Figure 5.4. P1 and P2 observations of particle distributions are shown in Panels A to G and Panels H to N. Panels A to C represent the ion energy flux spectrum in azimuthal angle (Phi) in four energy ranges: 30 to 50 keV, 5 to 10 keV, and 0.5 to 1 keV. Azimuthal angle spectrograms are shown in DSL (De-spun, Sun-pointing, L-vector) coordinates. Phi = 0 refers to earthward- and Phi = 90 refers to dawnward-moving particles (spin axis is southward and the angles are right-handed in the probe coordinate system). The black lines over-plotted are φB, the azimuthal

angle of magnetic field. Notice that the Z-axis scale of Panels A and H is different from the other azimuthal distribution plots due to the much lower flux in the high energy band. Panels D and E split the ion energy spectrum into earthward (defined as pitch angle ≤ 30 degrees) and tailward (defined as pitch angle ≥ 150 degrees). Panel F shows the pitch-angle distribution of the energetic (≥ 1keV) electrons. Panel G shows the distance d (in lunar radius R_L) from the Moon's center normal to the locally measured magnetic field line. d = 1 R_L , represented by a red line, indicates when the local field is connected to the Moon, assuming a straight line approximation. Dashed lines in Panel G marked the specific times chosen to show detail particle distribution functions in figure 5.5.

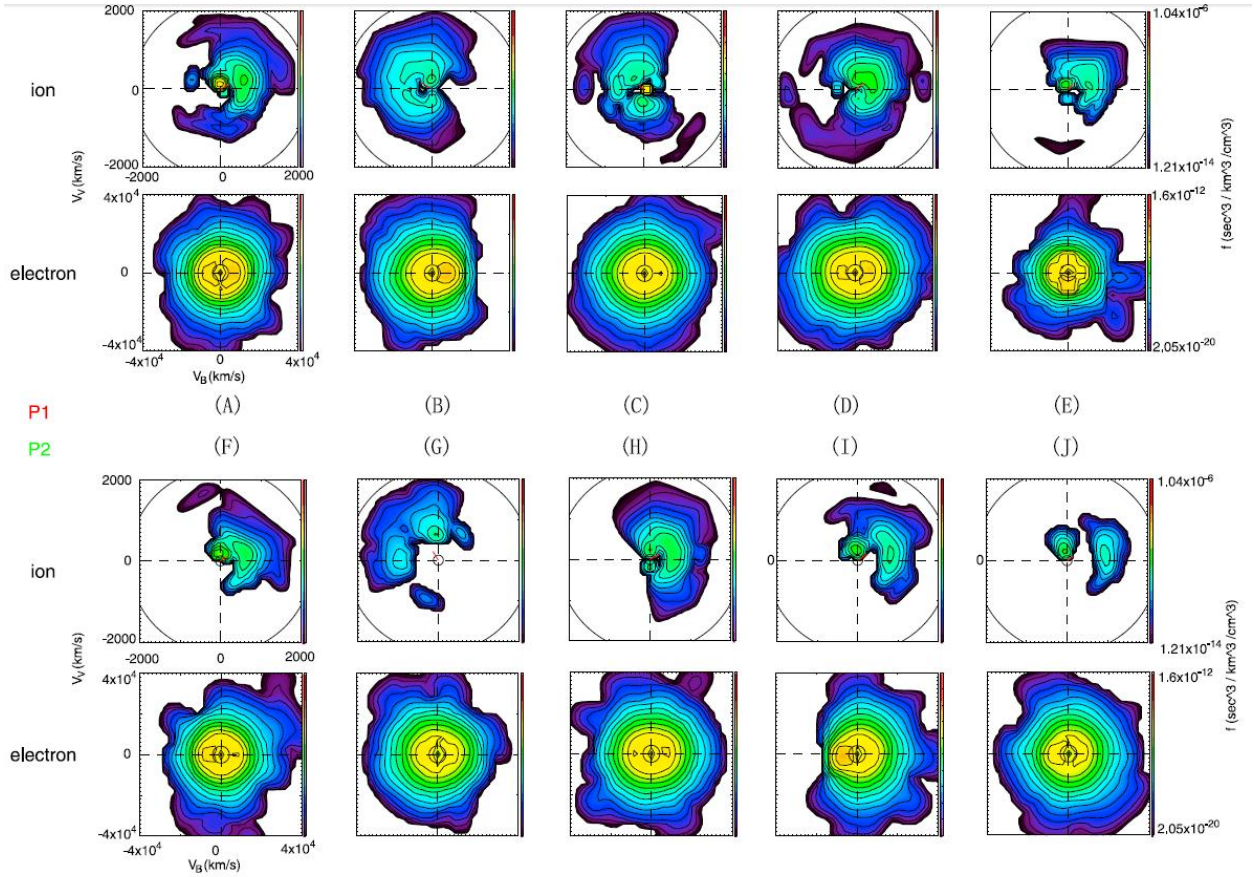

Figure 5.5. The ion and electron distribution function in the bulk velocity plane are represented here - P1observations shown in Panel A-E and P2 observations shown in Panel F-J.

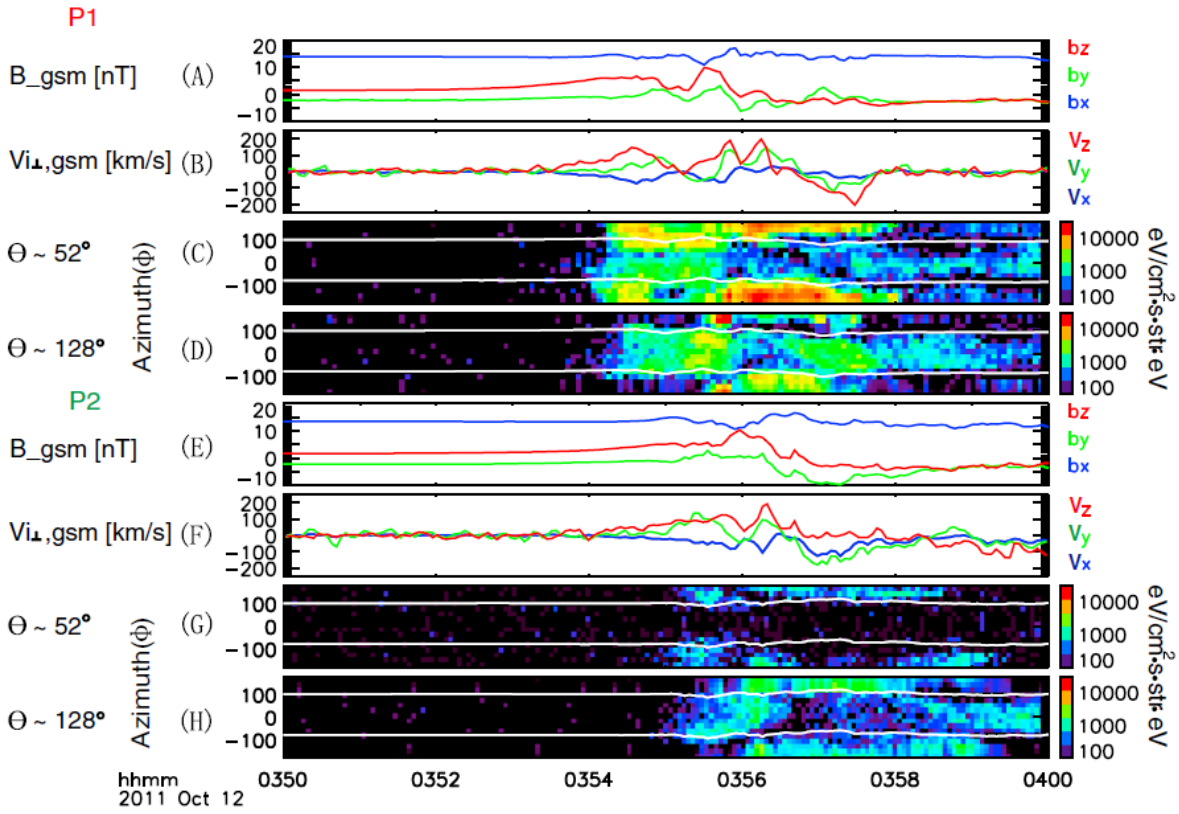

Figure 5.6. P1 and P2 observations are presented in Panels A to D and Panels E to H, respectively. Panels C and D (Panels G and H) show energetic (30-50 keV) ions' azimuthal distributions, which are similar to Panel A in Figure 3. Notice that Panel C/D (Panel G/H) only shows ions with □= -52/52 degrees. Overplotted white lines show the φB-90 degree- and φB+90 degree-directions. As the boundary of dense plasma approaches, a detector with direction perpendicular to the plane normal tends to observe duskward (φB-90 degree) ions earlier than dawnward (φB+90 degree) ions. The time delay reveals the boundary propagation velocity, based on the remote sensing technique (explained in the text), which is perpendicular to the magnetic field. For comparison I also show the perpendicular ion velocity in Panels B and F and magnetic field variations in Panels A and E.

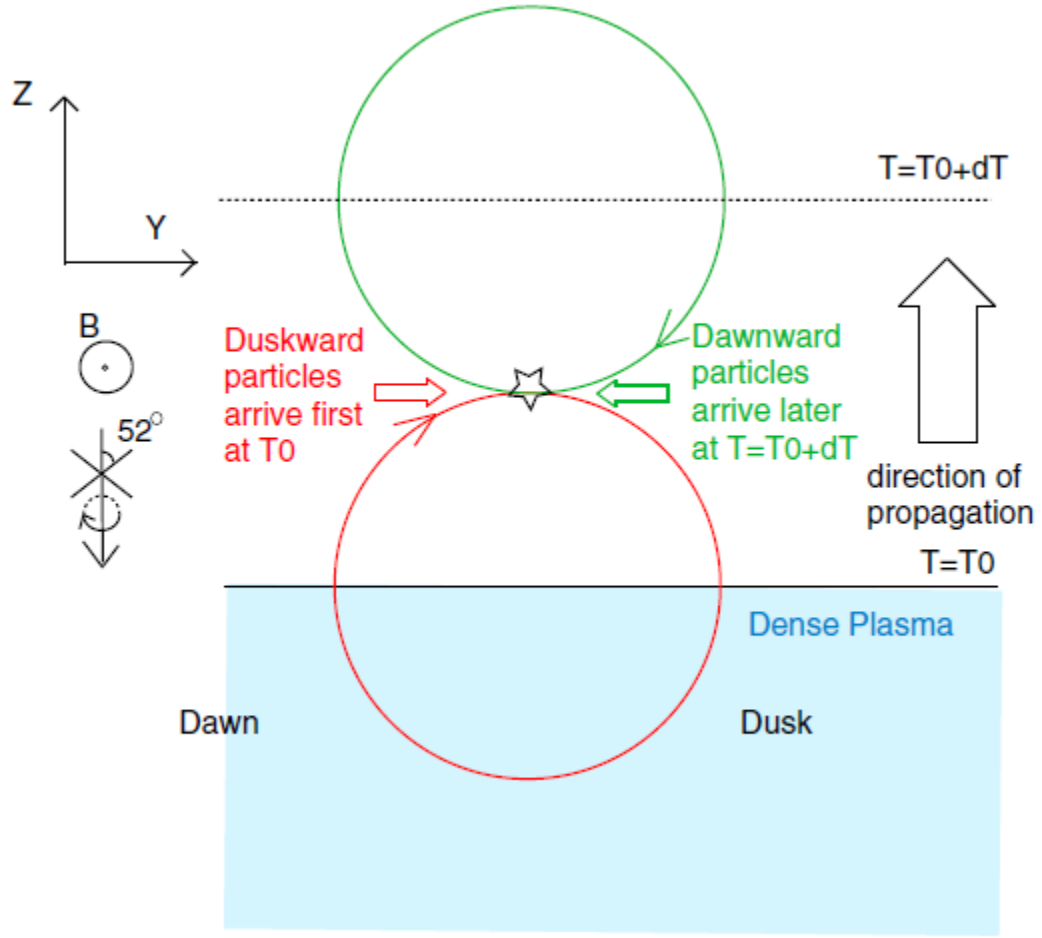

Figure 5.7. Pictorial representation of the remote sensing technique. The red line represents the gyro-orbit of an energetic ion, which has its guiding center at the boundary at T_0. The green line is the gyro-orbit of a similar ion detected at $T=T_0 +dT$; i.e., after the boundary moves two gyroradii northward within the time dT.

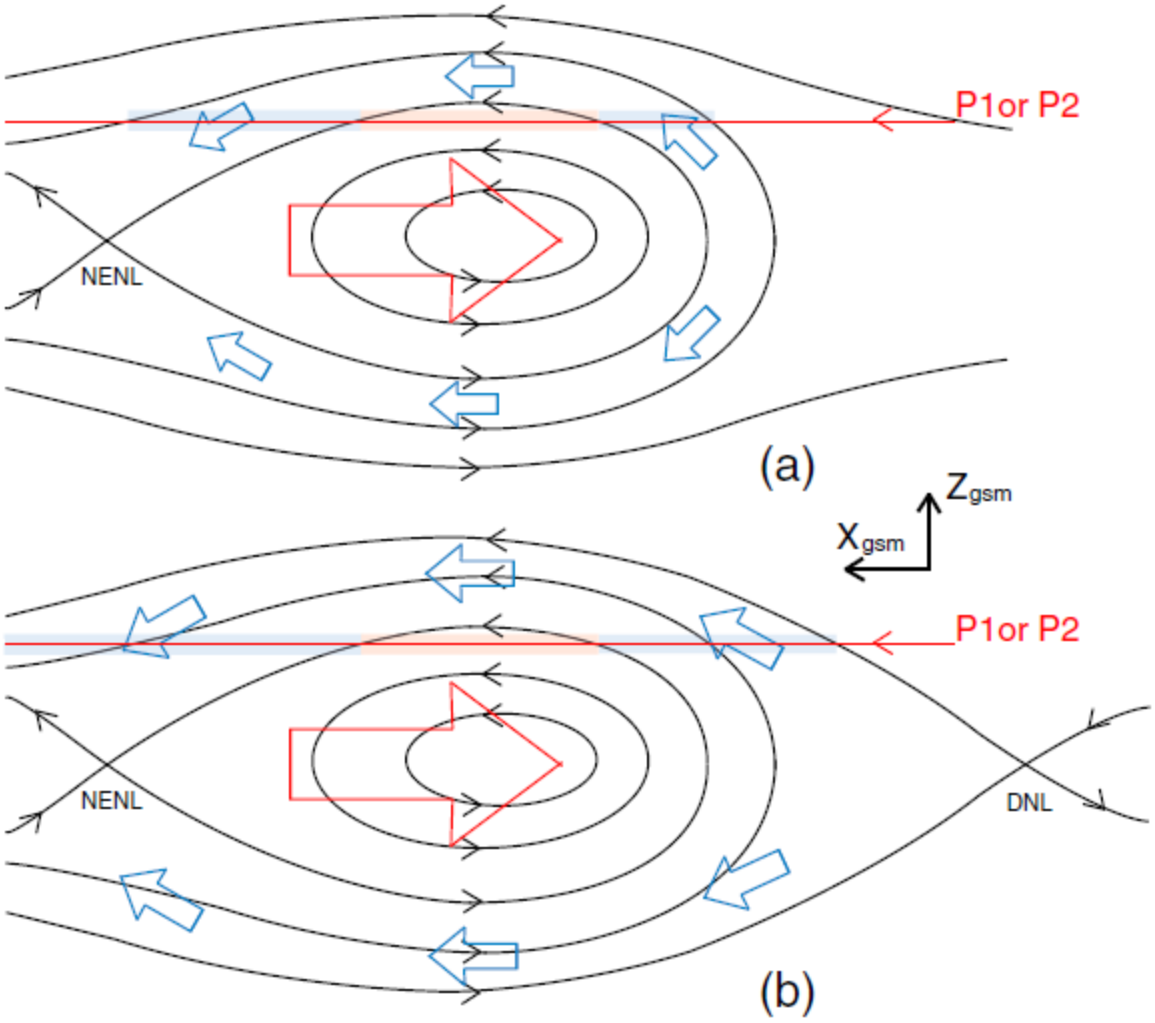

Figure 5.8. Two possible interpretations of the multi-layered plasmoid structure in the meridional plane (the top one is the favored one in this study). Black lines represent magnetic topology. Red and blue arrows signify tailward and earthward bulk flow direction. The red line shows the relative probe trajectory as the plasmoid propagates tailward. In addition, sub-structure within the plasma sheet is colored in light red and light blue corresponding to the same shaded regions as in Figure 5.1.

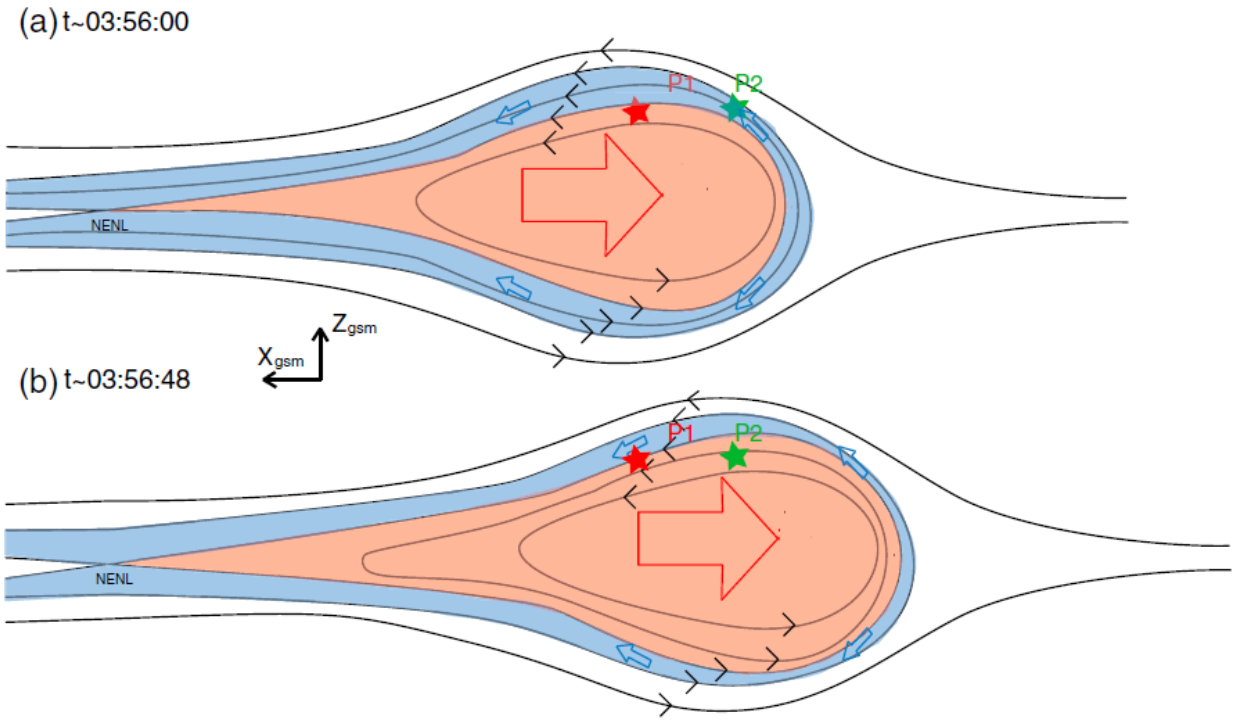

Figure 5.9. Pictorial representation of plasmoid expansion: the structure observed by P1 (Figure 5.9a) had grown larger when observed by P2 (Figure 5.9b) due to NENL reconnection on plasma sheet field lines. Regions with different color shading represent layers with different plasma populations and flow directions, corresponding to similar shades in Figure 1. Relative probe locations and trajectories are marked in red (P1) and green (P2).

CHAPTER 6 Anti-Dipolarization Fronts Observed by ARTEMIS

In this chapter, I discuss the relationships between anti-dipolarization fronts (ADFs) and plasmoids. Below shows a diagram comparing ADFs to plasmoid similar to Figure 1.3. I show that magnetic and particle properties of typically tailward-moving ADFs are very similar to those of typically earthward-moving DFs, which is different from plasmoids (as illustrated in Figure 1.3). Like DFs, ADFs exhibit a sharp density decrease, plasma pressure increase, magnetic pressure increase, and particle heating immediately following the sharp B_Z change. Also, particle spectra indicate that, as with DFs, there are two distinctly different magnetically separated populations ahead of and behind ADFs. This is different from the energy spectrograms of plasmoids, however, which indicate a single hot population at the plasmoid center. We conclude that mid-tail ADFs are likely products of fast reconnection, observed on the tailward side of the reconnection site, just as DFs are products of fast reconnection seen on the earthward side. We suggest that ADFs are proto-plasmoids that emerge from near-earth reconnection and evolve quickly into plasmoids as they propagate down the tail.

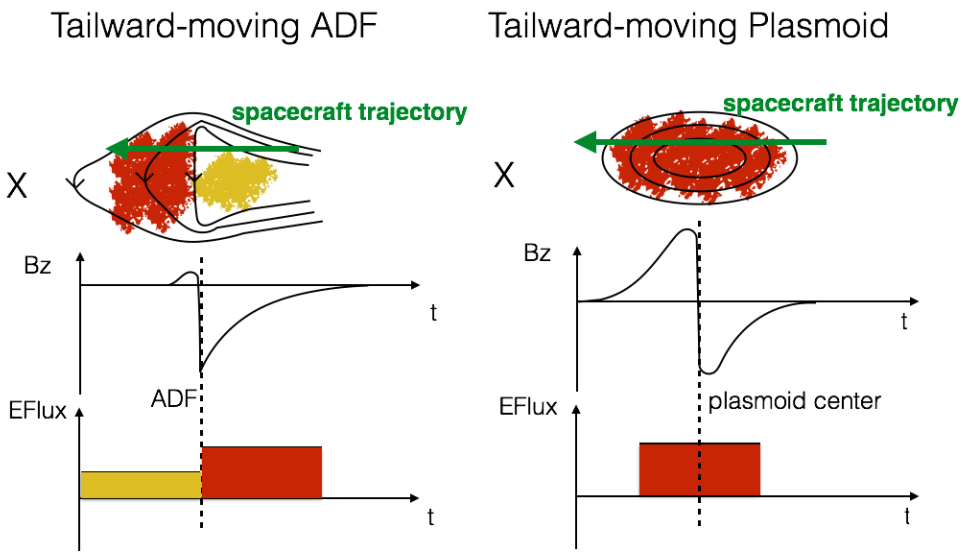

6.1 Introduction

A cursory observation of ARTEMIS data and past publications in light of the recent discovery of proto-plasmoids in Angelopoulos et al. [2013] reveals that anti-dipolarization fronts occur quite frequently in the mid-tail and near-Earth-tail. This impression is borne first by a more systematic examination of the plasmoids near lunar orbit utilized for Chapter 4: tailward-moving plasmoids exhibit an asymmetric north-south bipolar B_Z signature with a larger southward variation suggesting that ADFs are commonplace in this dataset. Next, observation of published data from studies of tailward flows [*Ohtani et al.*, 2004, Figure 8] and plasmoids [*Slavin et al.*, 2003, Figure 9], revealing asymmetric bipolar signatures in B_Z, indicate that ADFs exist in previous "plasmoid" lists at the near-Earth tail across a variety of databases. It is unclear how ADFs differ from plasmoids, however, because in previous studies ADFs have not been distinguished from plasmoids. In this study, an attempt is made to do just that. I first studied ADFs identified by criteria similar to that of DFs, which requires an extremely sharp B_Z decrease. Then I removed the ADFs from previous raw "plasmoid" list identified by traditional plasmoid criteria, which require a strong total pressure enhancement and a B_Z bipolar variation (Chapter 4). I considered the rest as "classical" plasmoids and then compared ADF to plasmoid properties using magnetic field and plasma observations.

The goal of this ADF study is to understand plasmoid evolution and reconnection outflow characteristics on the tailward side of the reconnection site. *Angelopoulos et al.* [2013] suggest that proto-plasmoid (by definition encompassing an ADF within it) may eventually evolve into a classical plasmoid as it propagates to the distant tail. As an ADF could be formed by open field line reconnection, such an evolution would require reconnection at another site, tailward of the

ADF. When reconnection occurs between ADFs which are separated in the dawn-dusk direction, it results in the formation of an azimuthally extended plasmoid. Here I present a case study that supports the hypothesis that an ADF may evolve into a plasmoid through reconnections. The observations of DFs and ADFs indicate that reconnection could produce a pair of fronts moving in opposite directions. *Sitnov et al.* [2011] simulated the onset of reconnection in 2-D current sheet equilibria that included an X-line. By applying a convective electric field E_Y outside the current sheet, a pair of fronts would be generated, which transport energy and flux rapidly away from the reconnection site and enable reconnection to continue. In this study, I show clearly the similarities between ADFs and DFs on the two sides of the reconnection site.

I surveyed 3 years of ARTEMIS (P1 and P2) data and studied anti-dipolarization fronts (ADFs) at X~-60 R_E. In Section 6.2, I show detailed plasma observations of a typical ADF. In Section 6.3, I introduce the statistical selection criteria and present a superposed epoch analysis. In Sections 6.4 and 6.5, I compare ADFs with plasmoids and present conclusions.

6.2 Database and an Example of an ADF

Since October 2010, the ARTEMIS spacecraft (P1 and P2) [*Angelopoulos*, 2010; *Sibeck et al.*, 2011] have spent 4 days per month in the magnetotail close to lunar orbit (X~ -40 to -60 R_E). Because the typical NENL location is at X= -20 to -30 R_E, the orbits of the ARTEMIS spacecraft favor observation of anti-dipolarization fronts(ADFs) generated directly from NENL reconnection. Using three years of ARTEMIS observations (from October 2010 to October 2013), I identified ADFs on the tailward side of the NENL. The magnetic field and plasma data are obtained from the fluxgate magnetometer (FGM) [*Auster et al.*, 2008], the electrostatic

analyzer (ESA) [*McFadden et al.*, 2008], and the solid-state telescope (SST) [*Angelopoulos*, 2008b] onboard ARTEMIS.

I applied my selection criteria to magnetic field fluxgate spin-fit (FGS) data in 3-4s resolution (depending on satellite spin period, which varied during the interval of study), which are available most of the time. I calculated plasma moments from the full particle distribution functions. However, plasma data in full-angular distribution and 3-4s time resolution are only available during fast-survey mode (approximately 8-12 hours per day, depending on the year). Hence, in my superposed epoch analysis I only included ADFs that occurred during fast-survey mode. During fast-survey mode, magnetic field data at higher resolution (4-samples-per-second data) were also available and utilized (instead of spin-fits) in the superposed epoch analysis.

The intensity of ground activity is indicated by the THEMIS pseudo AE index, which is computed from THEMIS ground magnetometer observations [*Angelopoulos*, 2008b]. Since mid-tail plasmoids are generally localized in the magnetotail, their corresponding ground activities should also be localized [*Chapter 4*]. The ~50 THEMIS ground magnetometers provide a dense station network in North America which offers spatially well-resolved auroral electrojet measurements of even localized auroral activations between 0300 UT and 1200 UT. In the superposed epoch analysis, I therefore utilize the THEMIS pseudo AE index on ADFs between 0300 UT and 1200 UT.

Figure 6.1 shows a typical isolated ADF on the tailward side of the NENL observed by both P1 and P2 on 1st August 2012 at ~0422 UT when P1 and P2 were located at (-56.7, 10.3, 1.7) R_E and (-56.2, 11.1, 0.9) R_E in GSM coordinates. The term "isolated" means that the magnetic field is relatively unperturbed before ADF arrival. Figure 6.1a, which presents the THEMIS-AE index

during the 4 hours before and after ADF arrival, shows a major AE enhancement beginning at ~ 0404 UT and a smaller AE enhancement beginning at ~0420 UT. I suggest that the isolated ADF (marked by dashed line on the right) is related to the smaller AE enhancement, and the other ADF (marked by dashed line on the left) observed at ~0407 UT is related to the larger AE enhancement. Here I discuss only the isolated ADF, since this study focuses on isolated ADFs such as the one observed at ~0422 UT. Similar to the DFs, this ADF presents a sudden front-like perturbation in B_Z (Figure 6.1b, 6.1f), a gradually increasing fast flow that starts approximately 1 minute prior to ADF arrival (Figure 6.1c, 6.1g), and a total pressure enhancement (Figure 6.1d, 6.1h). Moreover, the populations preceding and trailing the ADF are distinctly different from each other (Figure 6.1e, 6.1i).

Figure 6.2 shows ion angular distributions in azimuthal angle (Φ) and electron angular distributions in pitch angle (PA) within 4 minutes before and after ADF arrival. The ADF separates two distinct populations. Before ADF arrival (~0422 UT), P1 and P2 were at the plasma sheet boundary layer (~0418 UT). Tailward-streaming electrons (pitch angle ~ 180 degrees at northern hemisphere, Figures 6.2d and 6.2h) and ions (azimuthal angle ~ 180 degrees, Figure 6.2b) are observed. These energetic electrons indicate an active NENL reconnection earthward of the spacecraft. These energetic ions, on the other hand, could be either streaming-ions from the reconnection site or reflected ambient plasma sheet ions accelerated by the electric field behind the front [*Zhou et al.*, 2012]. At 04:19:30 UT, P2, which was slightly (less than $1R_E$) duskward and southward of P1 (P2 was closer to the neutral sheet), entered the central plasma sheet, where a hotter isotropic electron distribution was observed (Figure 6.2f, 6.2h). As shown by the energy flux increase (Figure 6.2c, 6.2f), compression began ~1 minute prior to ADF

arrival. At the same time, the velocity and pressure started to build up. Behind the ADF, both spacecraft encountered energetic ions with fast tailward flow (Figure 6.2b, 6.2f).

To better understand the scenario, I also plotted the energy flux distributions for electrons with different pitch angles at four key times (times marked by four lines under Figure 6.2h; distributions shown in Figure 6.2i to v2p). The red, blue, and black lines represent electron populations that are anti-parallel, parallel, or perpendicular, respectively, to the magnetic field direction. Except when a spacecraft was inside the central plasma sheet (Figure 6.2n), tailward-streaming electrons (anti-parallel when Bx is positive and parallel when Bx is negative) were observed most of the time during ADF passage (Figure 6.2i, 6.2j, 6.2k, 6.2m, 6.2o, 6.2p). However, after ADF passage when both spacecraft were still inside the hot tailward flow (similar to the post-plasmoid plasma sheet in previous studies), the magnetic field line topologies were no longer open everywhere. For example, at ~0425 UT, P1 observed counter-streaming electrons (Figure 6.2l), suggesting that the field lines at P1 closed due to another reconnection tailward of the spacecraft.

I interpret the above observations using the cartoon shown in Figure 6.2q and 6.2r. Before ADF passage (6.2q), P1 was at the northern PSBL, and P2, which was at the plasma sheet, sensed the compression prior to ADF arrival (Figure 6.2c). Then, as indicated by the B_X variation, P1, which was originally located northward of the central plasma sheet (CPS), located right inside the CPS after the ADF; P2, which was originally located at the CPS, moved to the southward side of the CPS. Since the two spacecraft were separated only ~1 R_E in Z_{GSM} direction, I conclude that the plasma sheet has moved northward after the passage of the front (~1R_E). After ADF passage (2r), P1 was at the center of the post-plasmoid plasma sheet, and P2 was closer to

the southern PSBL. Both P1 and P2 observed a strong magnetic field in B_Z component and heated plasma. Note that another reconnection site tailward of the spacecraft (perhaps distant tail reconnection) should have been activated and closed some of the IMF (interplanetary magnetic field) field lines.

The observed features of ADFs evidently differ from those of classical plasmoids as revealed from distant tail observations. By surveying the first 10 months of ARTEMIS observations, I identified 74 "plasmoids" (52 tailward-moving and 22 earthward-moving) as defined by standard means, based on their total pressure enhancement [*Chapter 4*]. These "plasmoid" observations include both ADFs and typical plasmoids (see Figure C1 in Appendix C, which shows two plasmoids that have also been investigated by *Kiehas et al.* [2013]). In the Appendix C, I also present a typical DF (Figure C2) observed by both ARTEMIS spacecraft at the mid-tail, which has features similar to those of DFs at the near-Earth tail [*Runov et al.*, 2011; *Liu et al.*, 2013a]. These additional Figures reinforce my statements that ADFs, DFs and (classical) plasmoids all exist in the mid-tail.

6.3 Statistical Study

To select ADFs, I use the DF selection criteria of *Liu et al*. [2013a] with some simple modifications. My selection criteria for an isolated ADF are as follows:

(1) $dB_Z/dt < -0.5$ nT/s. The first point that meets this criterion denotes the t_0.

(2) Minimum Bz in the t_0 to t_0 + 30 s time range at least 5 nT smaller than that in the t_0-30 s to t_0 time range.

(3) Minimum B_Z in the t_0 to t_0 + 30 s time range smaller than -5 nT.

I also require the magnetic field to be relatively unperturbed prior to front arrival as follows (all applied to the time range from t_0-3min to t_0-30 s):

(4) $dB_Z/dt<0.25$ nT/s for the entire time range.

(5) Standard deviation about the mean B_Z, δB_Z <1.5 nT.

(6) Minimum B_Z greater by 2 nT than B_Z in the time range from t_0 to t_0+30s.

After removing perturbations in the dynamic magnetosheath, I identified 43 ADFs in 4600 hours of magnetotail observations by either ARTEMIS-P1 or -P2. For observations during fast-survey mode, I calculated the β-values to determine the most favorable spacecraft locations (β >0.5) for observing ADFs. During 1000 hours of observations in fast-survey mode inside the plasma sheet, 26 ADFs were observed. Figure 6.3a (6.3c) presents the locations of these 43 ADFs (26 in fast-survey) in the aberrated GSM-XY plane (view from the south). After normalization to the spacecraft residence time at different Y_{AGSM} locations (Figure 6.3b and 6.3d, green), ADFs (Figure 6.3b and 6.3d, magenta) still occur preferentially at the dusk side. Note that in Figure 6.3d, I restrict the spacecraft residence time (green) to β >0.5. This distribution is similar to that from ARTEMIS observations of plasmoids at the mid-tail [*Chapter 4*], GEOTAIL observations of NENL reconnection sites at the near-Earth tail [*Nagai et al.*, 2013], and THEMIS observations of earthward DFs [*Liu et al.*, 2013a] and traveling compression regions (TCRs, the remote signatures of plasmoids in the lobe) [*Imber et al.*, 2011] at the near-Earth tail. Since ADFs are also considered direct products of NENL reconnection, their cross-tail distributions are expected to be similar to those of NENL reconnection, earthward DFs, and mid-tail plasmoids.

The 26 ADFs that occurred during fast-survey mode have similar plasma moment properties. Figure 6.4 and Figure 6.5 show the results of my superposed epoch analysis (zero epoch is the positive B_Z peak point immediately before t_0 in the criteria). I superposed magnetic field ($|B_X|$, B_Z), electric field (E_X, E_Y), velocity (total velocity $V_{i,total}$ and perpendicular velocity in the X direction $V_{perp,X}$), density (Ni), temperature (Ti), and pressure (thermal pressure P_{th}, magnetic field pressure P_B, total pressure P_{ttl}). Although I show most variables in GSM coordinates, I present electric field variables in modified DSL (Despun Sun-L-vectorZ) coordinates that are approximately similar to GSE coordinates ($\delta E_X = E_X - E_{X,offset} \sim E_{X,GSE}$, $\delta E_Y^* = -(E_Y - E_{Y,offset}) \sim E_{Y,GSE}$, see *Angelopoulos* [2008b], *Liu et al.* [2011] and *Li et al.*[2013] for issues related to EFI data and the standard method to work around them). As shown in Figure 6.4a, the sharp decrease in B_Z is preceded by a smaller B_Z increase. Tailward flows (Figure 6.4e) usually begin about 1 minute before ADF arrival. The fast plasma motion of the ADFs results in a self-consistent dawn-dusk electric field [*Runov et al.*, 2011] at the front (Figure 6.4b). As with earthward DFs, behind the front (earthward of tailward-moving ADFs), the densities are lower (Figure 6.4h) and the temperatures are higher (Figure 6.4i). In addition, the magnetic pressure peaks immediately after the front (Figure 6.4j), and the thermal pressure peaks immediately before it (Figure 6.4k). The total pressure (sum of thermal pressure and magnetic pressure) is enhanced right at the front (Figure 4l), which is also typical of plasmoids (considering the front is the location of the B_Z reversal, the O-point of a plasmoid and the approximate location where pressure or curvature forces peak). The magnetic pressure enhancement behind the front is mostly contributed by B_Z, just as the pressure profile for DFs [*Chapter 3*]: As shown in Figure 6.4m, the total pressure in the GSM-Z direction ($P_{total,\,Z}$) drops quickly behind the front.

As in the case study, the correlation between AE enhancement and ADF observations also appears in the superposed THEMIS-AE index (Figure 6.5a). Here I superposed the THEMIS-AE index for all 17 ADFs from 0300 UT to 1200 UT to get the most accurate THEMIS measurements (17 of the 26 ADFs happened from 0300UT to 1200UT). As indicated by the median AE value, most of the ADFs are correlated with AE enhancements that start several minutes earlier, though the amplitude of AE enhancement is smoothed out in this figure (an effect of superposition).

In Figures 6.5b and 6.5c, I also present the superposed energy spectra for ion and electron observations after normalization. For each ADF, I normalize the observed ion and electron differential energy flux by dividing it by its average value over the preceding "quiet" time (from t_0-7 minutes to t_0-5 minutes). During this period, both magnetic field and plasma properties are considered relatively undisturbed by the arriving ADF. I then superpose the normalized ADF spectra. The population behind the ADF is clearly more energetic than the undisturbed population ahead of it. The distinct background particle observations also suggest that two different populations are observed on two sides of an ADF. About 1 minute before the ADF arrival, the energy flux of both ions and electrons start increasing in a broad energy range (figures 6.5b and 6.5c), which is consistent with the density enhancement shown in figure 6.4h. This observation suggests that the ambient plasma ahead of the front is compressed. As shown in Figure 6.5b, energetic ions (> 20keV) start to be observed earlier than the compressed particles before the ADF arrival, earlier than the ions of lower energy. They represent the field-aligned streaming ions as shown in previous case studies spacecraft are further from the neutral sheet [e.g., Figure 6.2b; *Angelopoulos et al.*, 2013, Figures S9, S11]. As shown in Figure 6.4g,

consistent with the appearance of the energetic ions, a precursor (tailward) flow starts ~ 2 minute before ADF arrival. Similar ion distribution features, thought to be caused by ion reflection on the DF, and accompanying earthward flows have been observed in association with DFs [*Zhou et al.*, 2010, *Zhou et al.*, 2011]. Prior to DF arrival, rather than thermalized ions observed near the neutral sheet, beam-like ions are seen at some distance further from the neutral sheet [*Zhou et al.*, 2012].

In my previous study of plasmoids using ARTEMIS observations (see Table 6.1), 74 "plasmoids" (52 tailward-moving "plasmoids" and 22 earthward-moving "plasmoids") were identified in 261 hours of plasma sheet observations [*Chapter 4*]. In my previous study, "plasmoids" were identified mainly by the total pressure enhancement; thus, a "plasmoid" in this list could be either a plasmoid or a ADF (or DF). During this period, from October 2010 to July 2011, 5 of 52 tailward-moving "plasmoids" (~10%) were actually ADFs and 2 of 22 earthward-moving "plasmoids" (~10%) were DFs. I exclude the 5 ADFs and 2 DFs from the previous "plasmoid" event list and study the remaining 67 plasmoids.

For comparison, I superposed the energy spectra (Figure 6.6) and parameters (Figure 6.7) of the 67 plasmoids. Here, the superposed epoch time is chosen as the midpoint of the bipolar signature in B_Z. Since the midpoint (t_{mid}) of B_Z bipolar signature for ADF is within one-spin (3-4s) of t_0 (t_{mid} - t_0 ~ -2.8s ± 2.8s), I suggest that the superposed epoch times in Figure 6.5 and Figure 6.6 are equivalent. To distinguish ADFs from plasmoids, I compare Figure 6.6 and Figure 6.7 to Figure 6.5 and Figure 6.4, respectively. First, the energy spectra of plasmoids in general clearly differ from those of ADFs. In Figure 6.6, a single hot population is shown at the center of the total pressure enhancement, as expected for the energy spectra of a plasmoid. Second, the B_Z

variations for the tailward-moving plasmoids (Figure 6.7e) are much smoother and more symmetric than the sharp, extremely asymmetric B_Z variations at the ADFs: the difference between the positive and negative peak values is smaller than that for ADFs.

As shown in the previous case study (Figure 6.1), a non-isolated ADF concurrent with a major AE enhancement was observed by both P1 and P2 before the isolated ADF. Several other non-isolated ADFs have been observed prior to isolated ADFs in my dataset, most likely because of the nature of reconnection: As reconnection operates first on closed plasma sheet field lines and then proceeds to encompass the lobe field lines with larger magnetic field strength, the energy dissipation and the Alfvén speed likely get larger and the downstream outflow speed faster. As a result, both the observed amplitude and the variations of B_Z will strengthen and satisfy my criteria for isolated ADF identification.

6.4 Interpretation and Discussion

As shown in the above superposed epoch analysis, tailward ADFs and earthward DFs, identified by their steep variation (front-like) in the B_Z component (decrease for ADFs and increase for DFs) share similar properties: (1) The B_Z component variations are asymmetric (small positive, large negative for ADFs and small negative, large positive for DFs) and mirror images of each other. Both are correlated with substorms. (2) A fast flow starts about 1 minute prior to the front arrival, and its speed increases gradually ahead of the front. (3) Two distinct plasma populations are separated by the front. Compressed ambient plasma sheet plasma is ahead of it (the thermal pressure gradually builds up), heated plasma within newly reconnected magnetic field lines is behind it (the magnetic pressure dominates the total pressure) [*e.g., Chapter 3; Liu et al., 2013b*]. The thickness of ADF is typically ~ 3500km along its normal direction estimated using the

minimum variance analysis method [*Liu et al.*, 2013a, Appendix A], twice the thickness of DF at the near-Earth tail. (4) Energetic ions are observed ahead of the front. For DFs, these ions are accelerated ambient plasma sheet particles reflected by the fast-propagating front and extending into the equatorial plasma sheet ahead of the front (where they participate in the pressure buildup) [*Zhou et al.*, 2014] or streaming along field lines somewhat further away from the neutral sheet (where they appear as "boundary layer"-like beams)[*Zhou et al.*, 2012]. The reflection is caused by the strong magnetic field (B_Z) behind the front, and the acceleration by the strong electric field (E_Y) behind the front [*Zhou et al.*, 2010, 2011]. This mechanism is also valid for ADFs, since strong negative B_Z and duskward E_y have also been observed behind them (Figure 6.4a, b); therefore I interpret these ions are due to a similar, reflection process. Also, as shown in Figure 6.2c, along with tailward velocity, the ions at the compressed region show a duskward drift ($\Phi \sim$ 270 degrees) that fits the model of reflected ions accelerated by E_Y [*Zhou et al.*, 2010, 2011], again supporting the ion reflection model at ADFs as well. These similarities between ADFs and DFs suggested that the two types of fronts are produced by the same mechanism - near-Earth neutral line reconnection [Figure 1, *Angelopoulos et al.*, 2013]. As suggested in the nightside flux transfer event (NFTE) model of bursty flows [*Sormakov and Sergeev*, 2008] and MHD simulations (e.g., *Ugai*, 2011), reconnected field lines carrying tenuous, hot plasma reside behind the front. As the population behind the front is ejected by the curvature forces of the newly reconnection field lines, the population ahead of it (ambient plasma sheet plasma) is compressed.

There are some differences between tailward ADFs at the mid-tail plasma sheet and earthward DFs at the near-Earth tail, however. As shown in Figures 6.2, field-aligned energetic ions are seen several minutes before the front arrival (Panel b, $\Phi \sim$180 degree), but the compressed low

energy ions are observed only ~1 minute before the front arrival (Panel 2c). This could be explained by the topological difference of magnetic field lines between the near-Earth tail and the mid-tail. Unlike the relatively strong dipole field in the near-Earth tail, the magnetic field at the mid-tail is mainly in the +/- X direction, anti-parallel/parallel to the propagation direction of ADFs. Hence, streaming particles coming along field lines from the reconnection site are more common than heated near-neutral sheet heated particles.

Anti-dipolarization fronts may exist not only in the mid-tail. Based on Geotail observations at the near-Earth tail (X> -31 RE), *Ohtani et al.* [2004] studied the fast tailward flows and found similar sharp decrease in B_Z with amplitude comparable (5~10 nT) to my ADF observations at mid-tail. Their average flow speed is also ~200km/s and the flow duration is also several minutes. Similar to the ADF observations, density decrease and temperature enhancement are observed related to the fast flow observations. Based on these similarities, I suggest that ADFs exist in their dataset. However, differences between the two observations made at different X-locations (and also different criteria) are also very clear. (1) The magnetic field B_Z observed at $-20 < X_{AGSM} < -5\ R_E$ barely turns to negative. My mid-tail ADF observations, on the other hand, are mostly negative. This difference simply reflects the characteristic of the background magnetic dipole field. Such trend has been shown in near-Earth tail observations (*Ohtani et al*.[2004] Figure 9b). (2) The density appears to be gradually decreasing irrelevant to magnetic field change for the tailward flows at the near-Earth tail. This is different from near-Earth tail earthward flow events (equivalent to DFs), where density increases gradually ahead of the front and decreases abruptly at the front. However, from the mid-tail ADF observations, though different from near-Earth tailward flow events, the density varies similar to the near-Earth DFs.

There are two possibilities for this difference. First, the tailward flows are selected at the earthward side of the typical X-line locations and the superposed parameters may represent characteristics of other structures besides ADFs. Second, the near-Earth tail observations reveal the original state of ADF structures, which evolves while propagates tailward. To further investigate this difference in future studies, consistent ADF criteria should be applied on near-Earth observations so that ADFs will be distinguished from other tailward-moving structures.

I also applied the DF criteria of *Liu et al.* [2013a] to the same three years of ARTEMIS observations and identified 29 DFs (positive B_Z enhancement) at the mid-tail (15 of them during fast survey, see Appendix C). Their properties are similar to those of DFs at the near-Earth tail (see Appendix C). I find that 11 out of the 15 fast-survey DFs show earthward flows, which is approximately the same ratio of tailward ADFs showing tailward flows (23 out of the 26 fast-survey ADFs show tailward flows). However, earthward DFs have approximately half the absolute occurrence rate than tailward ADFs at the ARTEMIS distances, indicating the predominance of the near-Earth reconnection inside of X~-60 R_E. In other words, even though earthward flows are observed more frequently than tailward flows at X~-60 R_E [*Nishimura et al.*, 2013a, 2013b], flows with near-Earth reconnection-associated strong magnetic field perturbations are observed more often in the tailward direction than in the earthward direction. This is likely because reconnection at X<-60 R_E, although more frequent, is not as strong as that at the near-Earth tail due to the low plasma density and magnetic field strength in the distant tail.

The differences between ADFs and plasmoids are evident when comparing the energy spectra of the normalized differential energy flux in Figures 6.5 and 6.6. The energy spectra of ADFs have a sharp boundary separating two populations of different typical energy. The energy spectra of

plasmoids, however, have a hot population rather than a sharp boundary at the center. Consider that in the NFTE model, if the spacecraft trajectory were close to the boundary of the NFTE (a lobe-NFTE-lobe type traverse), the energy spectra of the NFTE would be similar to that of a plasmoid [*Sormakov and Sergeev*, 2008]. To avoid this potential bias, I also restricted my analysis to plasmoids in the central plasma sheet (by requiring that the plasma β-value be greater than 0.5 during the quiet time before the plasmoid observation) and found that the superposed energy spectra of this subset of plasmoid observations have similar properties (not shown here) to the energy spectra of the entire set of plasmoids (Figure 6.5).

Although the detailed evolution of ADFs into plasmoids is unclear, the two phenomena are probably related because their cross-tail distributions are quite similar (Figure 6.3d and Figure 6.3b in *Li et al.* [2014]). Note that in this study, I identified 26 ADFs (in fast survey) from 1000 hours of plasma sheet observations. Hence, the occurrence rate of ADFs (26/1000) is only 10% that of tailward-moving plasmoids (52/261). ADFs have not been reported in distant-tail observations, and cursory review of published data from that distance suggests that they either do not exist or they are scarce in the distant-tail region. *Angelopoulos et al.* [2013] noted that ADFs may be proto-plasmoids generated directly from reconnection and that they evolve into plasmoids at the distant tail. Another reconnection site tailward of the ADFs would be required for this mechanism, however, in order to close the open field lines. Further studies with multi-spacecraft conjunctions are needed to prove this scenario.

6.5 Summary

I surveyed three years of ARTEMIS observations near lunar orbit and identified 43 anti-dipolarization fronts. These fronts, which show total pressure enhancement and bipolar B_Z

perturbation similar to those of plasmoids, actually differ from plasmoids. (1) Their magnetic field bipolar signature is highly asymmetric compared to plasmoids. It is more appropriate to describe the magnetic field variation as a small B_Z increase followed by a sudden, sharp decrease in B_Z. (2) The population following an ADF is distinctly different (more energetic, hot, and tenuous) from the one ahead of an ADF.

As indicated from MHD simulations, an ADF can be produced by a single pulse of fast reconnection, and it is not necessarily a closed loop/flux rope structure, unless plasma sheet field lines were involved in the reconnection process. This is different from the mechanism of plasmoid formation, in which two X-lines are required, and resembles the nightside flux transfer event picture of earthward flows. From the case study, the open field lines associated with the ADF start to get reconnected and form closed magnetic field loops after ADF passage. This supports the hypothesis that ADFs may evolve into plasmoids as they propagate to the distant tail.

The magnetic field and plasma properties of ADFs are almost the same as those of DFs in the near-Earth tail, except for the directions of B_Z, V_X, and E_X. These differences are all expected, since ADFs are on the tailward side of the reconnection site. Hence, ADF observations support the idea that near-Earth reconnection could generate a pair of fronts moving in opposite directions.

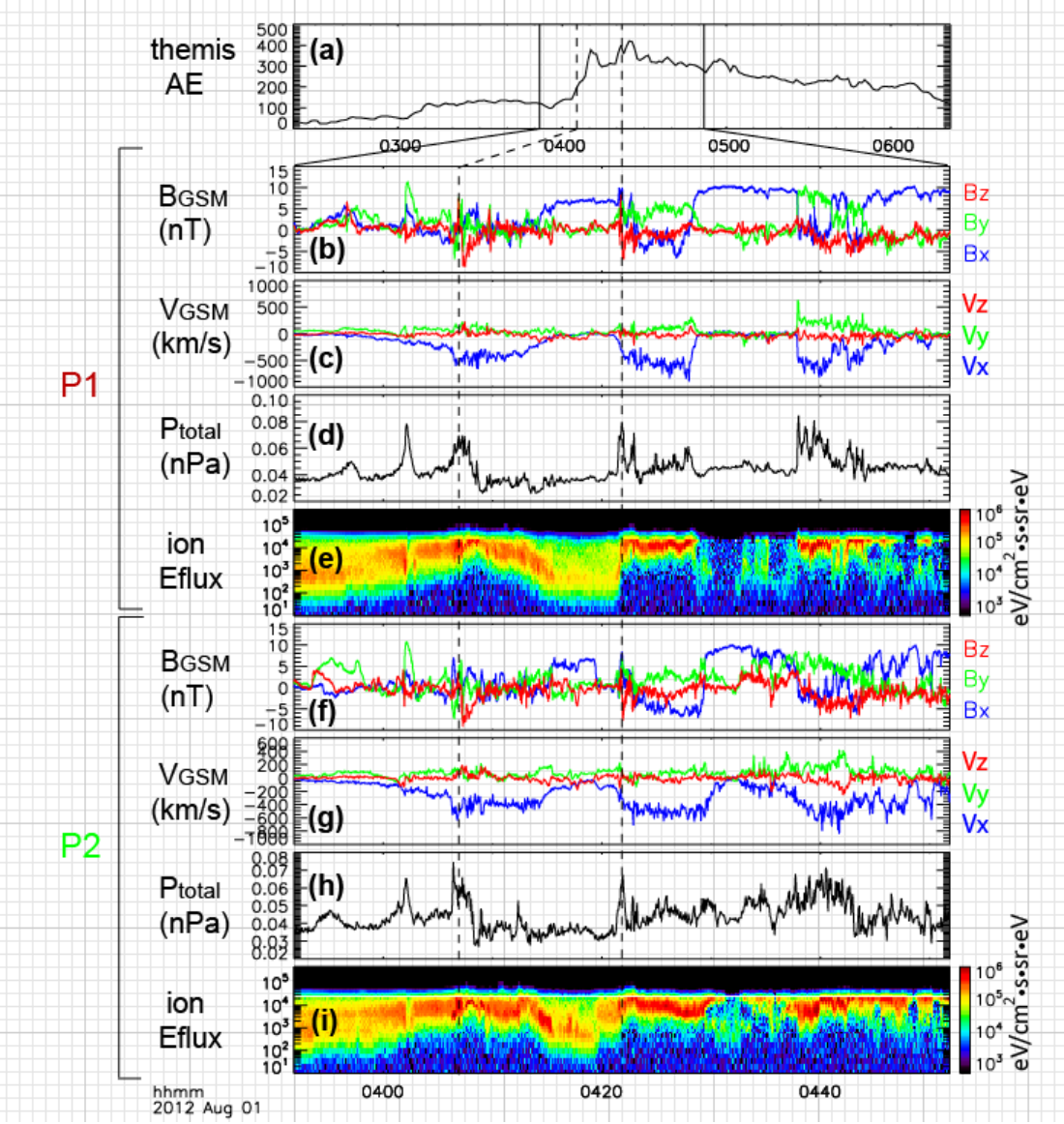

Figure 6.1. A typical isolated ADF (dashed line on the right) observed by the two ARTEMIS spacecraft, P1 and P2, at 0422 UT. From top to bottom are (a) the THEMIS AE index, (b–e) P1 observations, and (f–i) P2 observations. The spacecraft observations include the magnetic field and ion velocity in GSM coordinates, the total pressure (thermal and magnetic field pressure), and the ion energy flux spectrogram (from ESA and SST). The dashed line on the left indicates another ADF observed at 0407 UT.

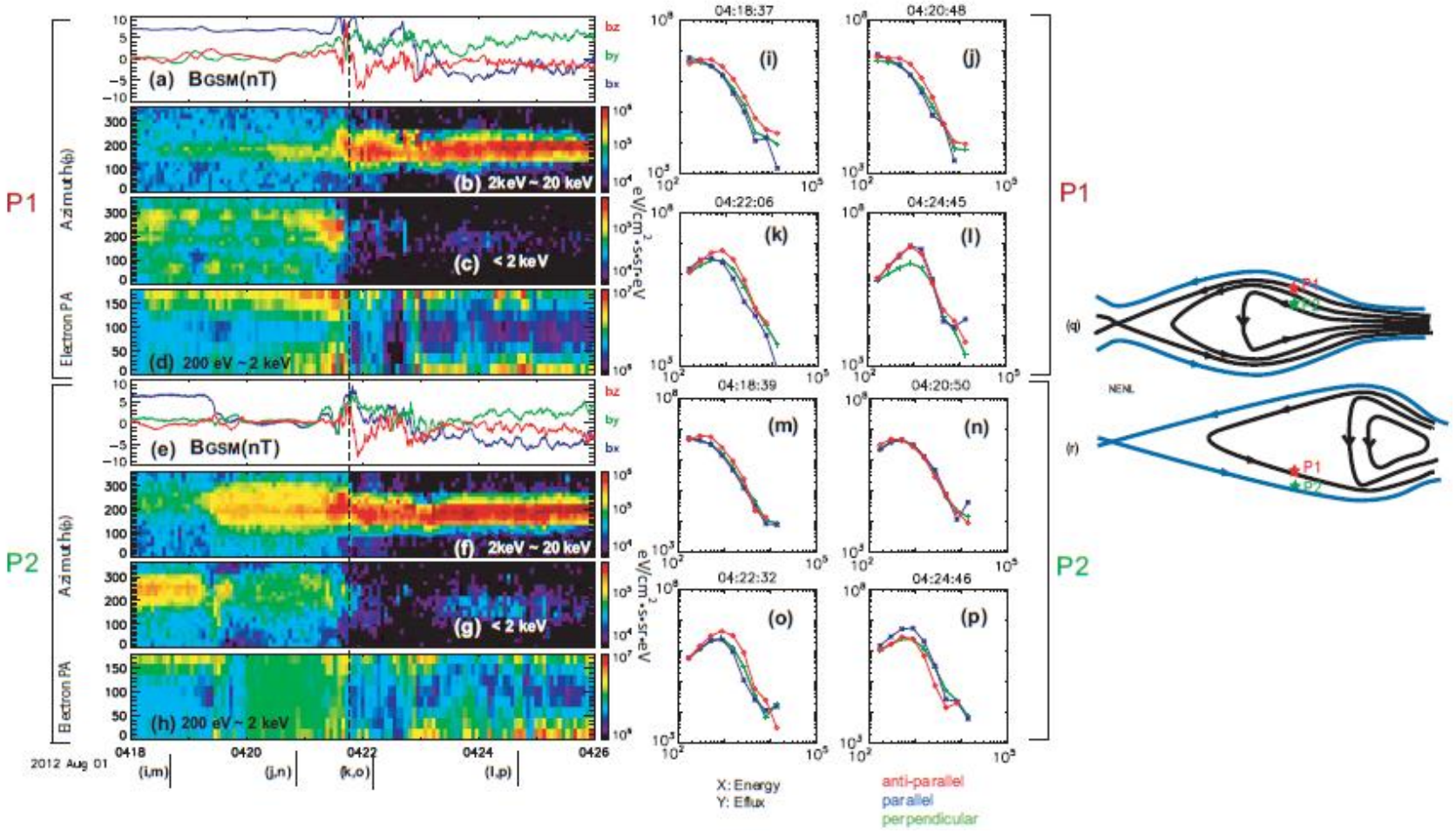

Figure 6.2. Particle angular distributions for the isolated ADF shown in Figure 1. Observations from P1 (2a-2d and 2i-2l) and P2 (2e-2h and 2m-2p) include magnetic field (2a, 2e), azimuthal angle distribution for energetic ions (2b, 2f) and low-energy ions (2c, 2g), electron pitch-angle distributions (2d, 2h), and electron energy flux profile (2i-2p) at four key times. I interpret the scenario in the cartoon shown in 2q and 2r.

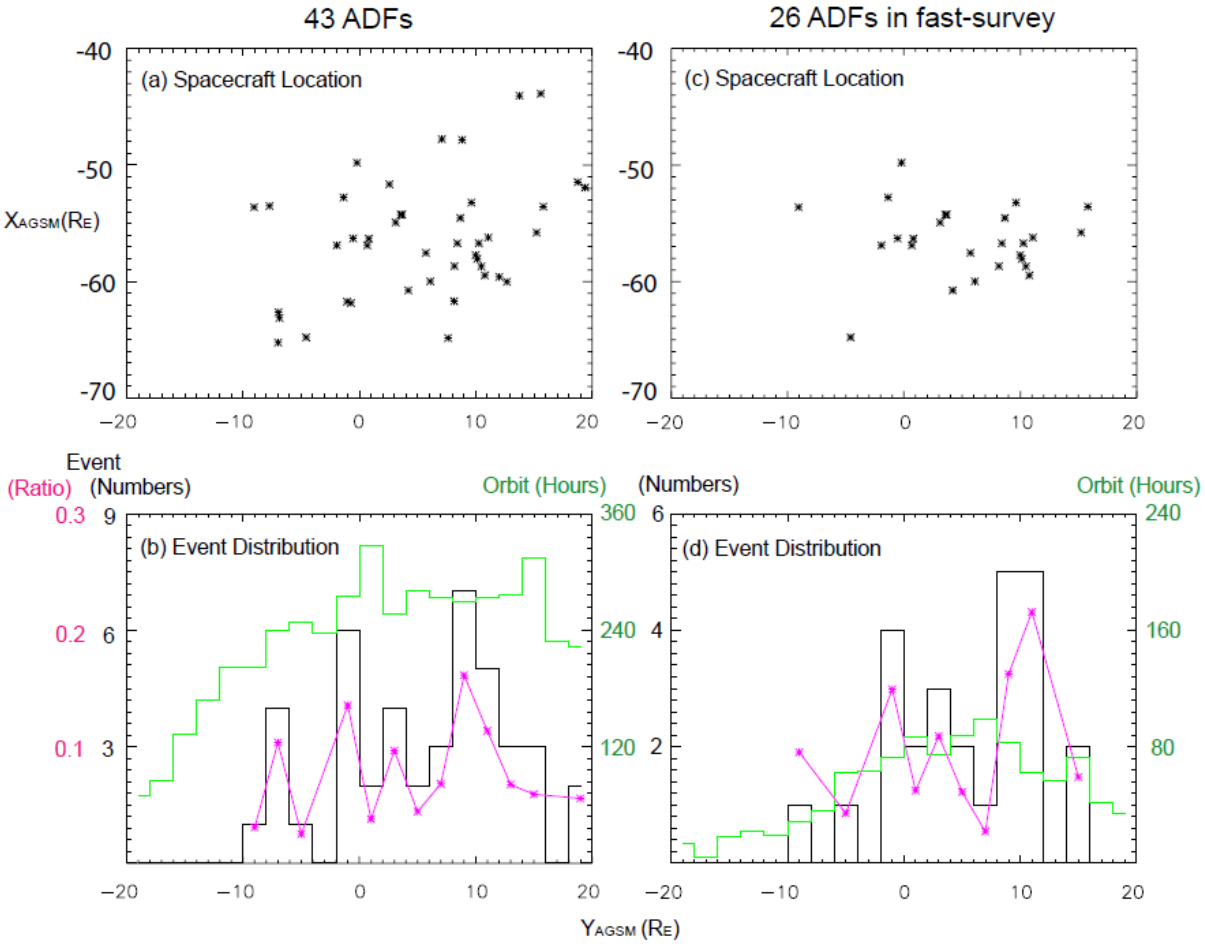

Figure 6.3. Event distribution in the azimuthal direction (Y_{AGSM}) for 43 ADFs (a-b) and 26 ADFs during fast survey (c-d). The horizontal axis is the Y_{AGSM} location of the spacecraft. In Figures 3a and 3c, the vertical axis is the X_{AGSM} location of the spacecraft (distributions in the equatorial plane viewing from south). In Figures 3b and 3d, the total number of events at different Y_{AGSM} locations is shown in black. The residence time of the spacecraft at different Y_{AGSM} locations is plotted in green. The normalized event distribution (total number divided by residence time) is shown in magenta.

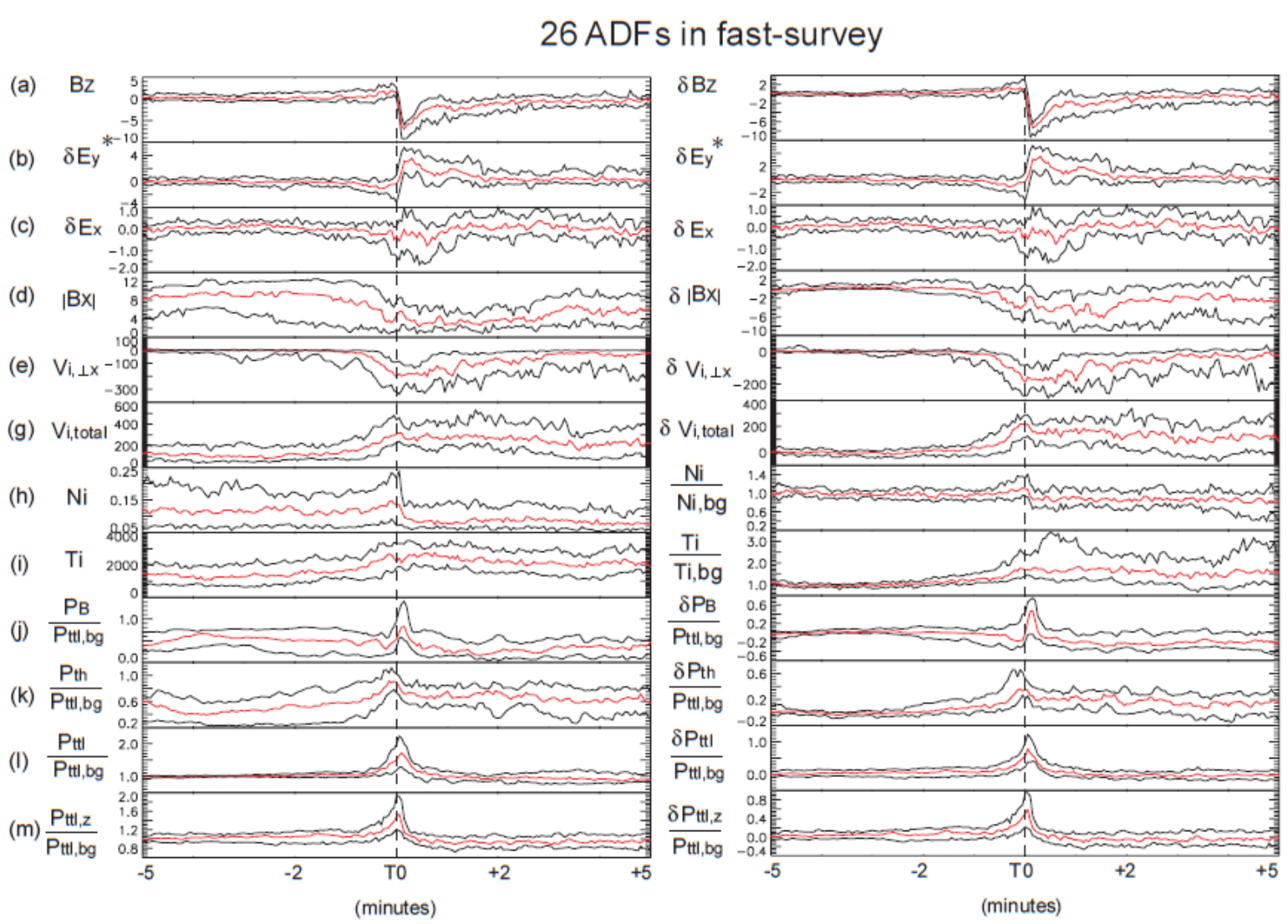

Figure 6.4. Superposed epoch analysis of the magnetic field (4a, 4d), electric field (4b, 4c), ion velocity (4e, 4g), ion density (4h), ion temperature (4i) and pressure (4j-4m) for 26 ADFs during fast survey. Here, P_B, P_{th}, P_{ttl} refer to magnetic pressure, thermal pressure and total pressure; $P_{ttl,bg}$ is the average value of total pressure from t_0-7 min to t_0-5 min. In each panels, upper and lower quartiles (black) and median values (red) are presented. Quantities on the left are then detrended by subtracting their average values from t_0-7 min to t_0-5 min. The detrended values are plotted on the right.

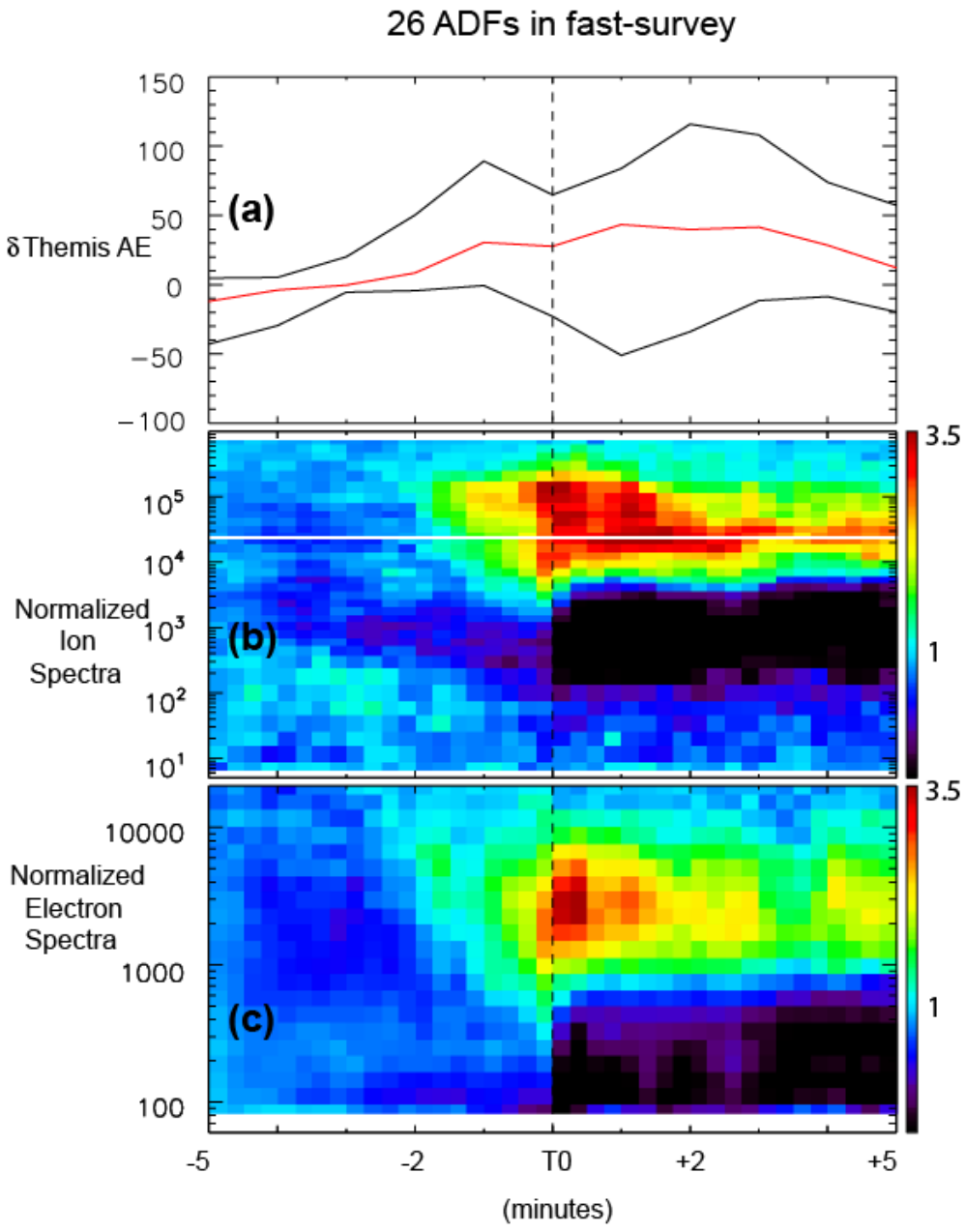

Figure 6.5. Superposed epoch analysis of the AE-index (5a), normalized ion energy flux spectrogram (5b), and normalized electron energy flux spectrogram (5c) for 26 ADFs during fast survey. In Panel a, upper and lower quartiles (black) and median values (red) are presented.

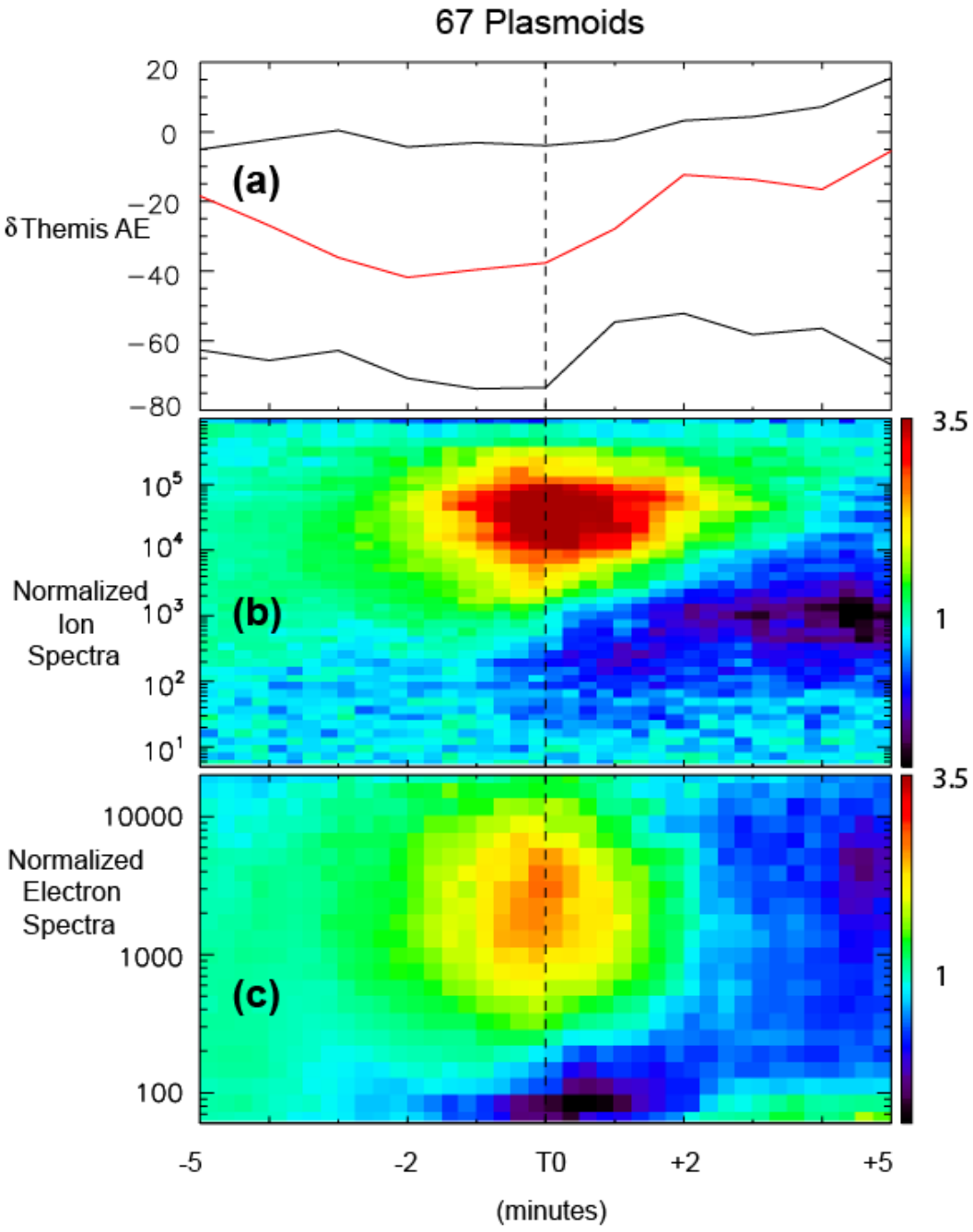

Figure 6.6. Superposed epoch analysis of the AE-index (5a), normalized ion energy flux spectrogram (5b), and normalized electron energy flux spectrogram (5c) for 67 plasmoids during fast survey. In Panel a, upper and lower quartiles (black) and median values (red) are presented.

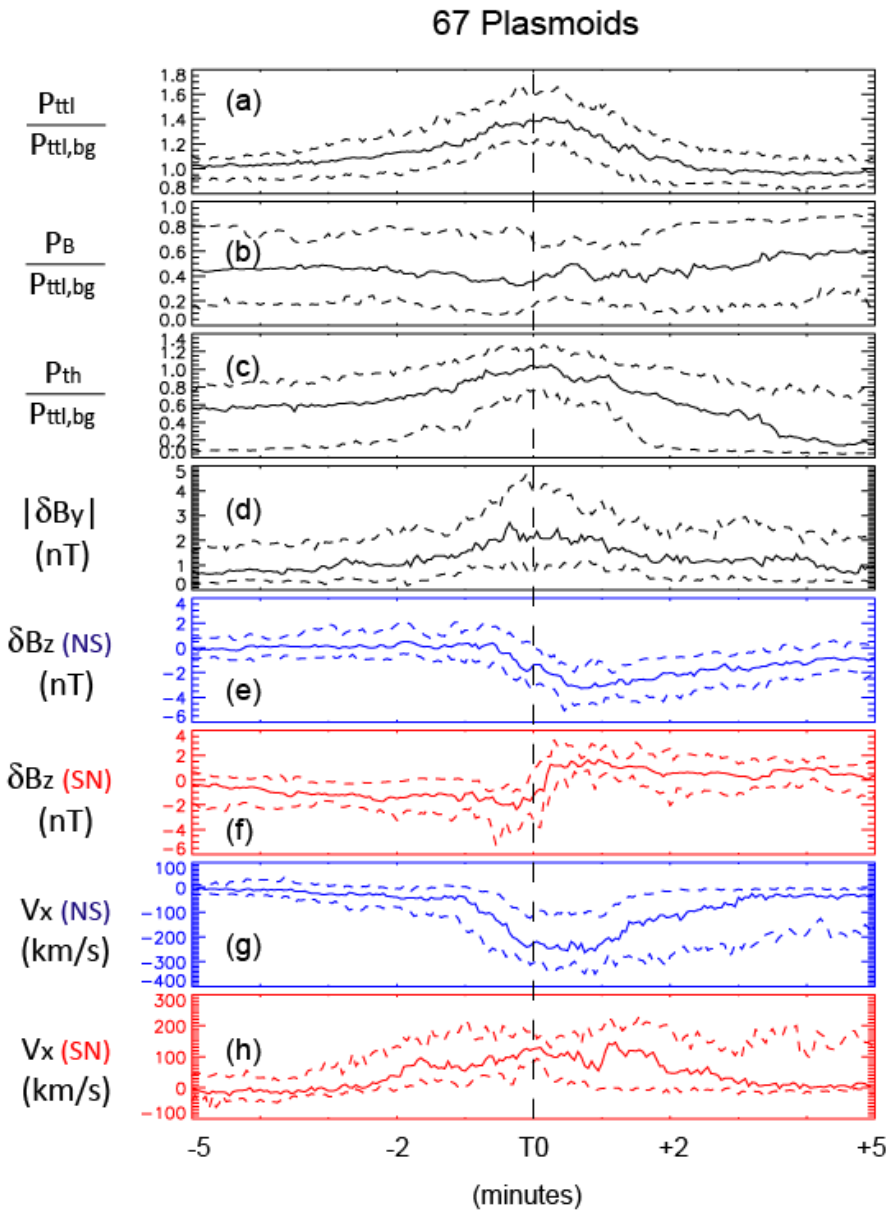

Figure 6.7. Superposed epoch analysis of pressure (7a - 7c), magnetic field (4d - 4f), and ion velocity (4e, 4g) for 67 plasmoids. Forty-seven of them are tailward-moving (7e, 7g), and 20 of them are earthward-moving (7f, 7h). Here, P_B, P_{th}, P_{ttl} refer to magnetic pressure, thermal pressure and total pressure; $P_{ttl,bg}$ is the average value of total pressure from t_0-7 min to t_0-5 min.

Event Category	B_Z	Observation Period	Observation Region	Observation Time (beta>0.5)	Event Number	Flow direction
DF (in fast survey)	South-North	2010.Oct-2013.Oct	X=-40 ~ -70 R_E	1000 hours	15	11 earthward
ADF (in fast survey)	North-South	2010.Oct-2013.Oct	X=-40 ~ -70 R_E	1000 hours	26	23 tailward
tailward Plasmoids	North-South	2010.Oct-2011.July	X=-40 ~ -70 R_E	261 hours	52 (5 ADF)	/
earthward Plasmoids	South-North	2010.Oct-2011.July	X=-40 ~ -70 R_E	261 hours	22 (2 DF)	/
DF ([*Liu et al.*, 2013a])	South-North	2008-2011	X=-10 ~ -30 R_E	every 1000 minutes	2	/

Table 6.1. Observation Database Summary

CHAPTER 7 Summary

Formation and expulsion of plasmoids are important aspects of magnetotail dynamics. The traditional NENL model describes such processes from a two-dimensional perspective and explains correlations between distant-tail plasmoid observations and substorm ground perturbations. This classical model, however, cannot explain recent findings related to the localized nature of plasmoids and fast flows. In this dissertation, three problems are investigated to help better understand plasmoid generation and evolution from a three-dimensional perspective.

In Chapter 4, I estimated the typical cross-tail extent of plasmoids at the mid-tail based on correlations between plasmoid/TCR observations at two locations separated mainly in the azimuthal direction. I found that: (1) Plasmoids near lunar orbit, like other near-Earth reconnection-related phenomena, occur preferentially on the duskside of the magnetotail. (2) In my dataset, the typical plasmoid azimuthal size is about 5 to 10 R_E, much smaller than expected from previous distant-tail observations. (3) Plasmoids with an azimuthal size greater than 10 R_E exist but only at geomagnetic activity levels higher (AEpeak>400 nT) than typically found in my dataset (median AEpeak ~ 230 nT for my plasmoid dataset and median AE ~ 100 nT during the entire period of ARTEMIS magnetotail observations). From above results, I conclude that during small to moderate substorms (AEpeak<400 nT), plasmoids do not grow beyond ~10 R_E until they have moved tailward of X ~ -65 R_E. During large substorms (AEpeak>400 nT), however, plasmoids either grow beyond ~10 R_E before they reach lunar distance or extend across a large portion of the magnetotail.

In Chapter 5, I estimated the average plasmoid size in its propagation direction to be 9 R_E and its expansion rate to be ~7 R_E/min at the observation locations. This plasmoid expansion observed at the plasmoid boundary (close to the plasma sheet boundary layer) is interpreted as plasmoid growth in both the X_{GSM} and the Z_{GSM} directions caused by near-Earth-neutral-line reconnection on closed plasma sheet field lines. The velocity inside the plasmoid was found to be non-uniform; the core likely moves as fast as 500 km/s, and the outer layers move more slowly (and in the reverse direction). The absence of lobe reconnection, particularly on the earthward side, suggests that plasmoid formation and expulsion both result from closed plasma sheet field-line reconnection.

In Chapter 6, I conclude that mid-tail ADFs are likely products of fast reconnection observed on the tailward side of the reconnection site, just as DFs are products of fast reconnection seen on its earthward side. (1) First, like DFs and plasmoids, ADFs are associated with auroral electrojet enhancements. (2) Second, like DFs, ADFs exhibit a sharp density decrease, a plasma pressure increase, a magnetic pressure increase, and particle heating immediately following the sharp B_Z change. (3) Third, particle spectra indicate that, as with DFs, there are two different magnetically separated populations ahead of and behind ADFs. Energy spectrograms of plasmoids, however, indicate a single hot population at the plasmoid center. I suggest that ADFs are proto-plasmoids that emerge from near-Earth reconnection and evolve quickly into plasmoids as they propagate down the tail.

I summarize the main results of this dissertation as follows: 1) NENL reconnections do not occur at the same time and same rate at different locations across the magnetotail; larger substorms are usually related to more extended NENL across the magnetotail. 2) Plasmoids could be ejected

tailward before the NENL proceeds to lobe field lines; thus, further growth beyond the mid-tail region may be caused by reconnections within one plasmoid or between several plasmoids. 3) NENL reconnection on either open field lines or closed field lines could produce and eject ADFs, structures physically different from plasmoids, directly. Those ADFs produced by lobe field line reconnection could evolve into plasmoids by re-reconnection of the IMF field lines.

APPENDIX A: Calculating the ideal success ratio for plasmoid detection

The success ratio is defined as the frequency with which both the test spacecraft and the reference spacecraft observe a plasmoid.

$$\text{Success Ratio} = \frac{\text{Probability (test spacecraft observes a plasmoid)}}{\text{Probability (reference spacecraft observes a plasmoid)}}$$

$$= \frac{\text{Probability (P1 and P2 both observe a plasmoid)} \times 2}{\text{Probability (P1 observes a plasmoid)} + \text{Probability (P2 observes a plasmoid)}}$$

$$= \frac{\text{Probability (P1 and P2 both observe a plasmoid)} + \text{Probability (P1 and P2 both observe a plasmoid)}}{\text{Probability (P1 or P2 observes a plasmoid)} + \text{Probability (P1 and P2 both observe a plasmoid)}}$$

Note that the success ratio, as defined in the observations, is naturally larger than the probability of both P1 and P2 observe the same plasmoid when P1 or P2 observes a plasmoid.

I build a simple model to calculate the ideal success ratio for a given plasmoid extent "a" and a given spacecraft separation "b". The assumptions are described as follows:

(1) The magnetotail's full azimuthal extent is 40 R_E.

(2) Both the spacecraft separation and the plasmoid axis are in the Y_{AGSM} direction.

(3) Both spacecraft are inside the magnetotail.

(4) Both sides of the plasmoid are inside the magnetotail.

(5) The plasmoid and spacecraft center locations are uniformly distributed inside the magnetotail.

The distribution function for the plasmoid center "x" and spacecraft center "y" in azimuthal direction can be written as:

$$f(x,y) = \frac{1}{(40-a)(40-b)}$$

$$x \in \left[-20+\frac{a}{2}, 20-\frac{a}{2}\right], y \in \left[-20+\frac{b}{2}, 20-\frac{b}{2}\right], 0 < b \leq a \leq 40\ R_E$$

Probability (P1 observes a plasmoid) = Probability $\left(x-\frac{a}{2} \leq y-\frac{b}{2} \leq x+\frac{a}{2}\right)$

$$= \begin{cases} \int_{-20+\frac{a}{2}}^{20-b-\frac{a}{2}} dx \int_{x-\frac{a}{2}+\frac{b}{2}}^{x+\frac{a}{2}+\frac{b}{2}} f(x,y)dy + \int_{20-b-\frac{a}{2}}^{20-\frac{a}{2}} dx \int_{x-\frac{a}{2}+\frac{b}{2}}^{20-\frac{b}{2}} f(x,y)dy = \dfrac{(40a-a^2-\frac{1}{2}b^2)}{(40-a)(40-b)}, & a \leq 40-b \\ \int_{-20+\frac{a}{2}}^{20-\frac{a}{2}} dx \int_{x-\frac{a}{2}+\frac{b}{2}}^{20-\frac{b}{2}} f(x,y)dy = \dfrac{(20+\frac{a}{2}-b)}{(40-b)} & , \quad a > 40-b \end{cases}$$

Probability (P2 observes a plasmoid) = Probability $\left(x-\frac{a}{2} \leq y+\frac{b}{2} \leq x+\frac{a}{2}\right)$

= Probability (P1 observes a plasmoid)

Probability (P1 and P2 both observe a plasmoid)

= Probability $\left(x-\frac{a}{2} \leq y-\frac{b}{2}$ and $y+\frac{b}{2} \leq x+\frac{a}{2}\right)$

$$= \int_{-20+\frac{a}{2}}^{20-\frac{a}{2}} dx \int_{x-\frac{a}{2}+\frac{b}{2}}^{x+\frac{a}{2}-\frac{b}{2}} \frac{1}{(40-a)(40-b)} dy = \frac{(a-b)}{(40-b)}$$

Hence, the success ratio is calculated as function of the plasmoid extent "a" and the spacecraft separation "b":

$$\mathrm{f}(\mathrm{a},\mathrm{b}) = \begin{cases} \dfrac{(\mathrm{a}-\mathrm{b})(40-\mathrm{a})}{(40\mathrm{a}-\mathrm{a}^2-\frac{1}{2}\mathrm{b}^2)}, & a \le 40-\mathrm{b} \\ \dfrac{(\mathrm{a}-\mathrm{b})}{\left(20+\frac{\mathrm{a}}{2}-\mathrm{b}\right)}, & \mathrm{a} > 40-\mathrm{b} \end{cases} \qquad 0 < b \le \mathrm{a} \le 40\ \mathrm{R_E}$$

I use this function to plot the probability curves in Figure 4.4b.

APPENDIX B: Solar Wind Flux Input during 2011, Oct 12th, 1:00- 5:00 UT

The total flux input into the magnetosphere from 01:00 UT to 03:40 UT is less than 3×10^7 Wb. The flux transported tailward in the form of the plasmoid is approximately 1.5×10^7 Wb, assuming that the extent of the plasmoid is ~10 R_E in azimuthal direction. Thus the plasmoid transport a significant portion of the flux previously loaded to the magnetotail. Note that the flux has been continuously added to the magnetosphere after the plasmoid passage. I suggest these flux will be transport tailward significantly after lobe reconnection took place.

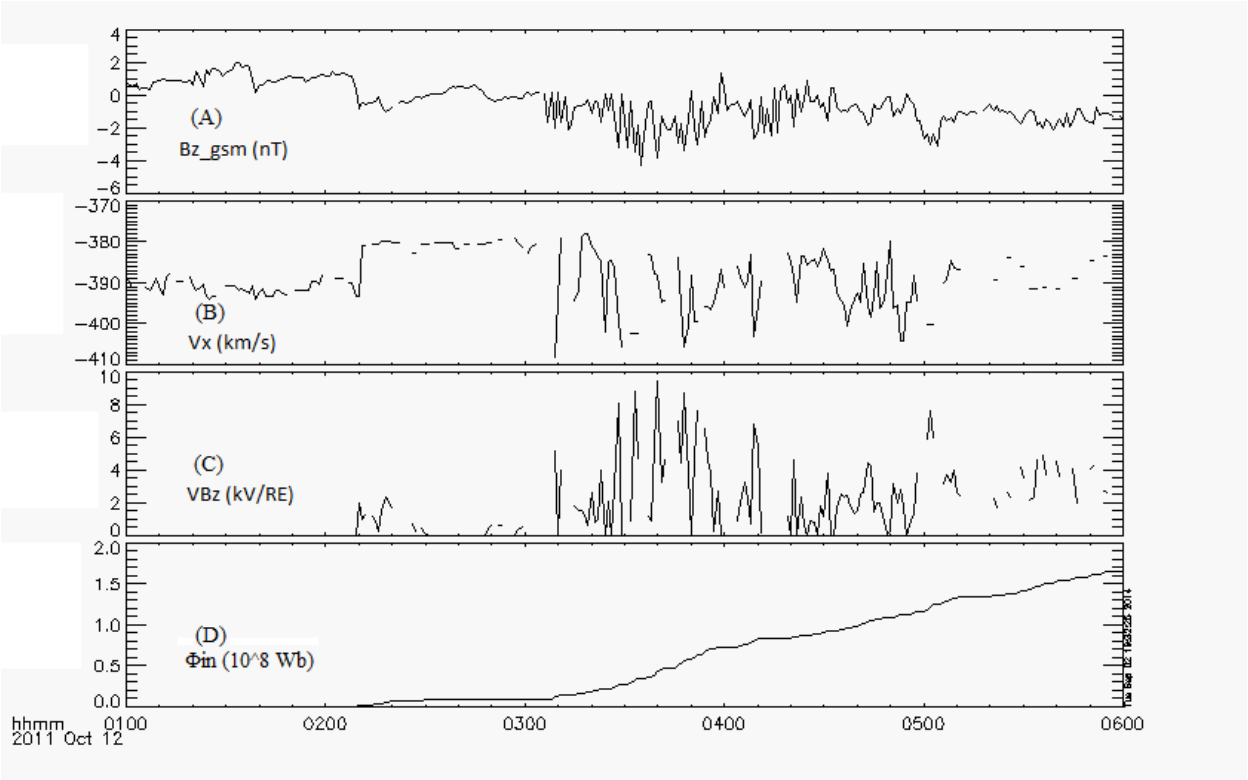

Figure B1.Computed solar wind input to the magnetosphere. Top two panels show the solar wind magnetic field B_Z component and velocity V_X component in GSM coordinate (OMNI data). Panel C shows the Electric field E_Y (VB_{south}) imposed on the magnetosphere due to the solar

wind flow. Panel D shows the total flux added to the magnetosphere due to dayside reconnection, which is estimated as the cumulative integral of E_Y, Φ_{in}, after accounting for the reconnection rate efficiency (20%) and the size of the magnetosphere (40 R_E).

APPENDIX C: Additional Figures for Chapter 6

Figure C1 shows two typical plasmoids selected from my plasmoid dataset, which are also studied in the *Kiehas et al.* [2013] paper. Figure C2 shows a typical mid-tail DF observed by both P1 and P2. Among the 15 selected DFs during fast survey, 11 of them show earthward flows. I superposed the parameters and energy spectra of the 11 DFs and showed them in Figure C3 and Figure C4. Their formats are the same with Figure 6.4 and Figure 6.5. In general, the dawn-dusk E_Y, the earthward E_X, the earthward flow velocity, the pressure profiles, the density depletion and the temperature enhancement behind the front are all similar to the DFs observed at the near-Earth tail [*Liu et al.*, 2013a].

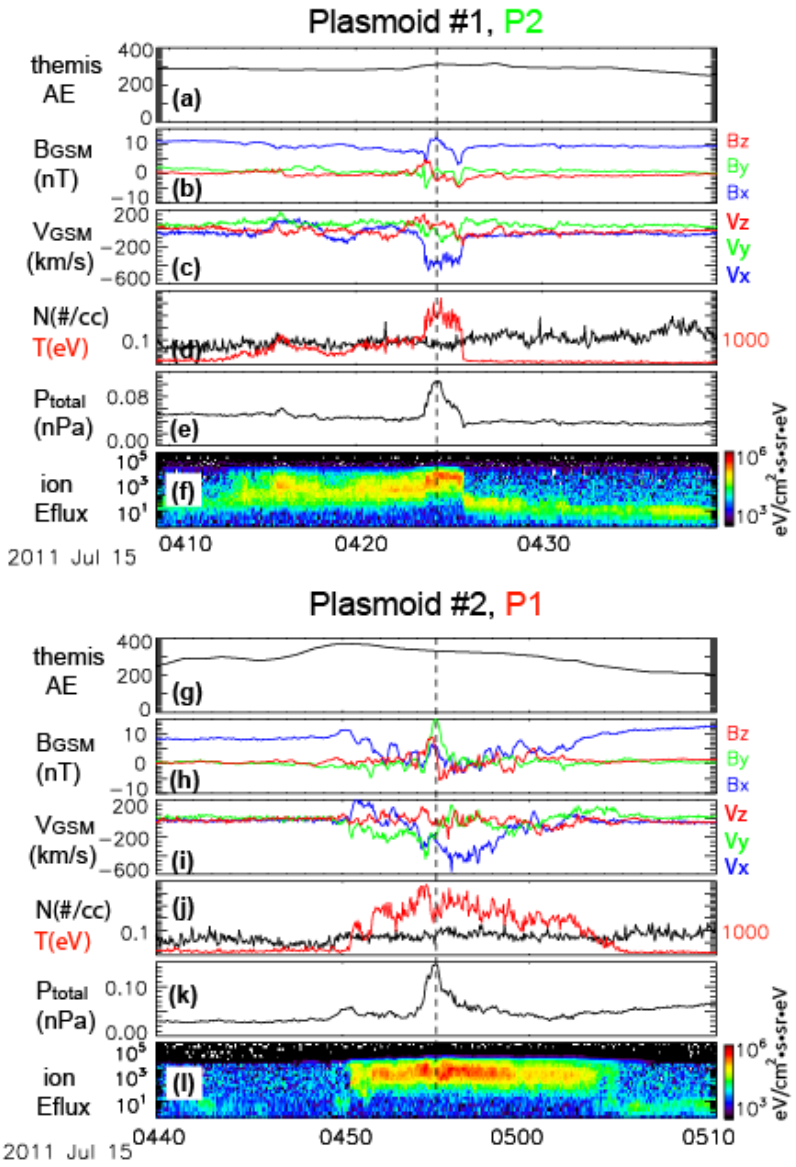

Figure C1. Two typical plasmoids observed by ARTEMIS spacecraft. The spacecraft observations include the magnetic field and ion velocity in GSM coordinates, ion temperature and density, the total pressure (thermal and magnetic field pressure), and the ion energy flux spectrogram (from ESA and SST).

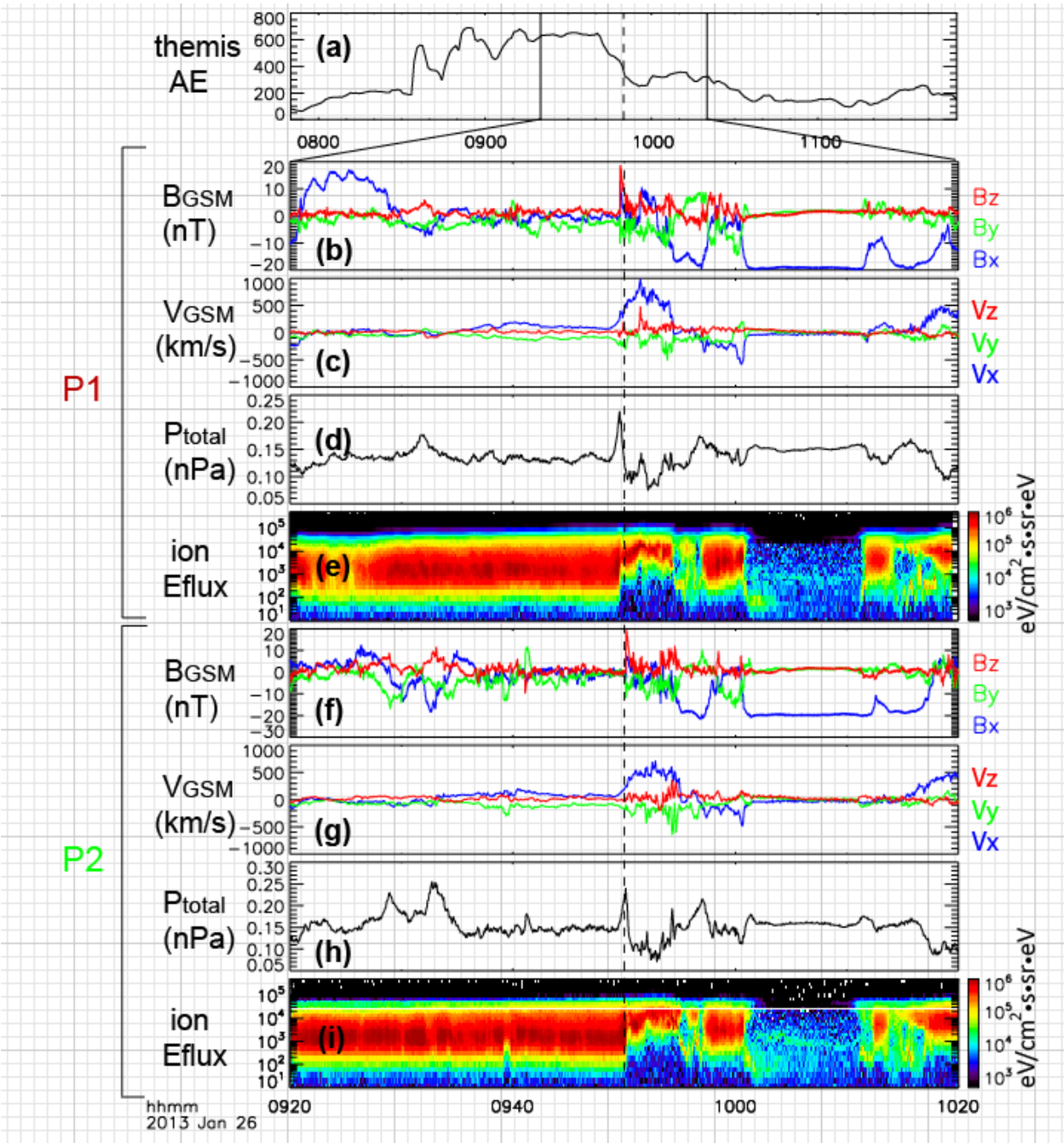

Figure C2 A typical isolated DF observed by the two ARTEMIS spacecraft, P1 and P2 at 0950 UT. The format is the same as in Figure 6.1.

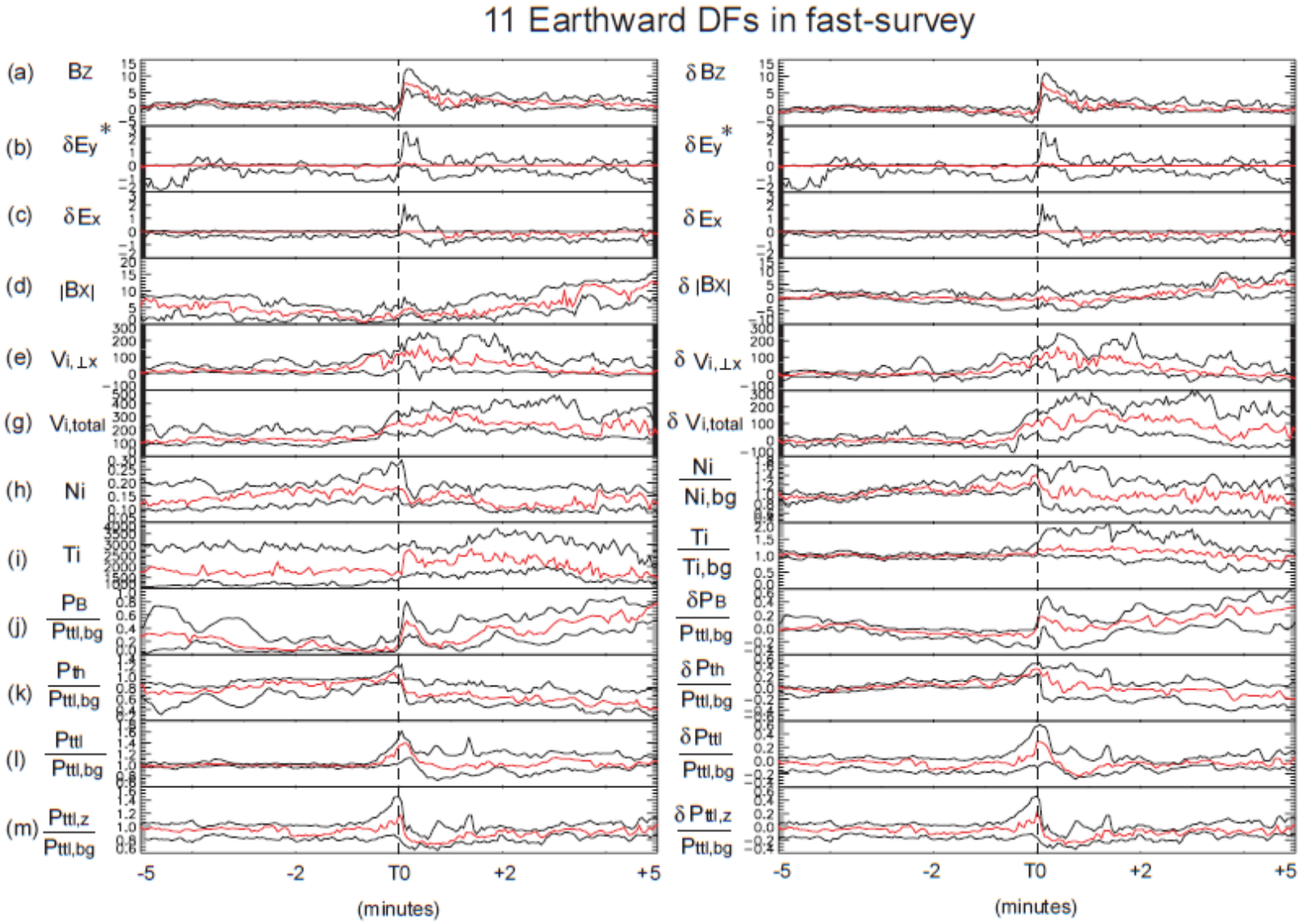

Figure C3. Superposed epoch analysis for 11 earthward-moving DFs during fast survey. The format is the same as in Figure 6.4.

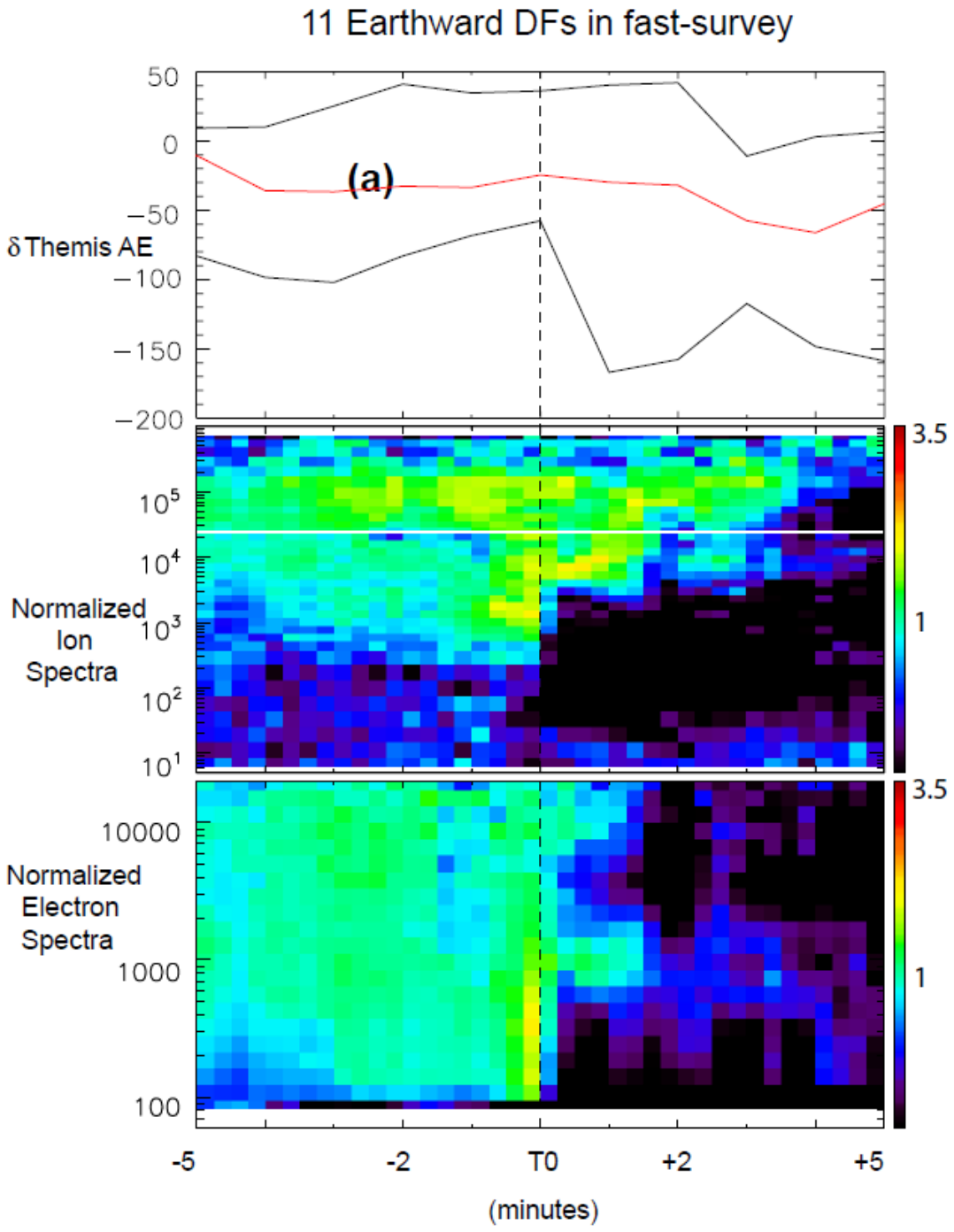

Figure C4 Superposed epoch analysis for 11 earthward-moving DFs during fast survey. The format is the same as in Figure 6.5.

Bibliography

Abe, S. A., and M. Hoshino (2001), Nonlinear evolution of plasmoid structure, *Earth, Planets, and Space, 53*, 663-671.

Aikio, A. T., V. A. Sergeev, M. A. Shukhtina, L. I. Vagina, V. Angelopoulos, and G. D. Reeves (1999), Characteristics of pseudobreakups and substorms observed in the ionosphere, at the geosynchronous orbit, and in the midtail, *J. Geophys. Res., 104*, 12,263-12,288, doi:10.1029/1999JA900118.

Angelopoulos, V., W. Baumjohann, C. F. Kennel, F. V. Coroniti, M. G. Kivelson, R. Pellat, R. J. Walker, H. Luehr, and G. Paschmann (1992), Bursty bulk flows in the inner central plasma sheet, *J. Geophys. Res., 97*, 4027-4039, doi:10.1029/91JA02701.

Angelopoulos, V., et al. (1994), Statistical characteristics of bursty bulk flow events, J. Geophys. Res., 99, 21,257–21,280, doi:10.1029/ 94JA01263.

Angelopoulos, V., T.D. Phan, D.E. Larson, F.S. Mozer, R.P. Lin, K. Tsuruda, H. Hayakawa, T. Mukai, S. Kokubun, T. Yamamoto, D.J. Williams, R.W. McEntire, R.P. Lepping, G.K. Parks, M. Brittnacher, G. Germany, J. Spann, H.J. Singer, and K. Yumoto: "Magnetotail flow bursts: association to global magnetospheric circulation, relationship to ionospheric activity and direct evidence for localization", *Geophys. Res. Lett*., **24**, 2275 (1997)

Angelopoulos, V., et al. (2008a), Tail Reconnection Triggering Substorm Onset, *Science 321*, 931, doi:10.1126/science.1160495.

Angelopoulos, V. (2008b), The THEMIS Mission, *Space Sci. Rev., 141*, 5-34, doi:10.1007/s11214-008-9336-1.

Angelopoulos, V. (2010), The ARTEMIS Mission, *Space Sci. Rev.*, doi:10.1007/s11214-010-9687-2.

Angelopoulos, V., et al. (2013) Electromagnetic energy conversion at reconnection fronts, *Science*, 2013 Sep 27; 341(6153):1478-82. doi: 10.1126/science.1236992.

Auster, H. U., et al. (2008), The THEMIS Fluxgate Magnetometer, *Space Sci. Rev., 141*, 235-264, doi:10.1007/s11214-008-9365-9.

Baker, D. N., T. I. Pulkkinen, V. Angelopoulos, W. Baumjohann, and R. L. McPherron (1996), Neutral line model of substorms: Past results and present view, *J. Geophys. Res., 101*, 12,975-13,010, doi:10.1029/95JA03753.

Baumjohann, W., M. Hesse, S. Kokubun, T. Mukai, T. Nagai, and A. A. Petrukovich (1999), Substorm dipolarization and recovery, J. Geophys. Res., 104, 24,995–25,000, doi:10.1029/1999JA900282.

Birn, J., J. Raeder, Y. Wang, R. Wolf, and M. Hesse (2004), On the propagation of bubbles in the geomagnetic tail, Ann. Geophys., 22, 1773–1786, doi:10.5194/angeo-22-1773-2004.

Bonnell, J. W., F. S. Mozer, G. T. Delory, A. J. Hull, R. E. Ergun, C. M. Cully, V. Angelopoulos, and P. R. Harvey (2008), The Electric Field Instrument (EFI) for THEMIS, Space Sci. Res., 141, 303–341, doi:10.1007/s11214-008-9469-2.

Borg, A.L., et al. (2012), Observations of magnetic flux ropes during magnetic reconnection in the Earth's magnetotail, *Ann. Geophys.*, 30,761-773, 2012, doi: 10.5194/angeo-30-761-2012

Dubyagin, S., V. Sergeev, S. Apatenkov, V. Angelopoulos, R. Nakamura, J. McFadden, D. Larson, and J. Bonnell (2010), Pressure and entropy changes in the flow-braking region during magnetic field dipolarization, J. Geophys. Res., 115, A10225, doi:10.1029/2010JA015625.

Eastwood, J. P., D. G. Sibeck, J. A. Slavin, M. L. Goldstein, B. Lavraud, M. Sitnov, S. Imber, A. Balogh,E. A. Lucek, and I. Dandouras (2005), Observations of multiple X-line structure in the Earth's magnetotail current sheet: A Cluster case study, Geophys. Res. Lett., 32, L11105, doi:10.1029/2005GL022509.

Grigorenko, E.E., et al. (2011) Non-adiabatic Ion Acceleration in the Earth Magnetotail and Its Various Manifestations in the Plasma Sheet Boundary Layer, *Space Sci. Rev.*, doi: 10.1007/s11214-011-9858-9

Halekas, J. S., et al. (2012), Lunar Precursor Effects in the Solar Wind and Terrestrial Magnetosphere, *J. Geophys. Res.*, p. in press.

Hones, E. W., Jr. (1977), Substorm processes in the magnetotail - Comments on 'On hot tenuous plasmas, reballs, and boundary layers in the Earth's magnetotail' by L. A. Frank, K. L. Ackerson, and R. P. Lepping, *J. Geophys. Res., 82*, 5633-5640, doi: 10.1029/JA082i035p05633.

Hones et al.(1984), Structure of the magnetotail at 220 earth radii and its response to geomagnetic activity , *Geophys. Res. Lett* ., vol. 11, Jan. 1984, p. 5-7, doi: 10.1029/GL011i001p00005

Hughes, W. J., and D. G. Sibeck (1987), On the 3-dimensional structure of plasmoids, *Geophys. Res. Lett., 14*, 636-639, doi:10.1029/GL014i006p00636.

Ieda, A., S. Machida, T. Mukai, Y. Saito, T. Yamamoto, A. Nishida, T. Terasawa, and S. Kokubun (1998), Statistical analysis of the plasmoid evolution with Geotail observations, *J. Geophys. Res., 103*, 4453-4466, doi:10.1029/97JA03240.

Ieda, A.et al. (2008), Longitudinal association between magnetotail reconnection and auroral breakup based on Geotail and Polar observations, *J. Geophys.Res.*, Volume 113, Issue A8, doi: 10.1029/2008JA013127

Imber, S. M., J. A. Slavin, H. U. Auster, and V. Angelopoulos (2011), A THEMIS survey of flux ropes and traveling compression regions: Location of the near-Earth reconnection site during solar minimum, *J. Geophys. Res.*, 116, A02201, doi:10.1029/2010JA016026.

Kiehas, S. A., et al. (2009), First application of a Petschek-type reconnection model with time-varying reconnection rate to THEMIS observations, *J. Geophys. Res.*, 114, A00C20, doi:10.1029/2008JA013528.

Kiehas, S.A., V. Angelopoulos, A.Runov, S.-S. Li, (2013), On the azimuthal size of flux ropes near lunar orbit, *J. Geophys. Res. Space Physics*, 118, 4415–4424, doi:10.1002/jgra.50425.

Li, S. -S., V. Angelopoulos, A. Runov, X.-Z. Zhou, J. McFadden, D. Larson, J. Bonnell, and U. Auster(2011), On the force balance around dipolarization fronts within bursty bulk flows, *J. Geophys. Res.*,116, A00I35, doi:10.1029/2010JA015884.

Li, S. -S., V. Angelopoulos, A. Runov, S. A. Kiehas, and X.-Z. Zhou (2013), Plasmoid growth and expulsion revealed by two-point ARTEMIS observations, *J. Geophys. Res. Space Physics*, 118, 2133–2144, doi:10.1002/jgra.50105.

Li, S. -S. et al. (2014a), Azimuthal Extent and Properties of Mid-tail Plasmoids From Two-point ARTEMIS Observations at the Earth-Moon Lagrange Points, *J. Geophys. Res. Space Physics*, 119,1781-1796, doi: 10.1002/2013JA019292.

Li, S.-S., J. Liu, V. Angelopoulos, A. Runov, X. –Z. Zhou, and S. Kiehas (2014b), Anti-Dipolarization Fronts Observed by ARTEMIS, *J. Geophys. Res. Space Physics*, DOI: 10.1002/2014JA020062

Liu, J., C. Gabrielse, V. Angelopoulos, N. A. Frissell, L. R. Lyons, J. P. McFadden, J. Bonnell, and K. H. Glassmeier (2011), Superposed epoch analysis of magnetotail flux transport during substorms observed by THEMIS, *J. Geophys. Res.*, 116, A00I29, doi:10.1029/2010JA015886.

Liu, J., V. Angelopoulos, A. Runov, and X.-Z. Zhou (2013a), On the current sheets surrounding dipolarizing flux bundles in the magnetotail: The case for wedgelets, *J. Geophys. Res.*, 118, 2000-2020, doi:10.1002/jgra.50092.

Liu, J., V. Angelopoulos, X.-Z. Zhou, A. Runov, and Z. H. Yao (2013b), On the role of pressure and flow perturbations around dipolarizing flux bundles, *J. Geophys. Res.*, doi:10.1002/2013JA019256.

Machida, S., A. Ieda, T. Mukai, Y. Saito, and A. Nishida (2000), Statistical visualization of Earth's magnetotail during substorms by means of multidimensional superposed epoch analysis with Geotail data, *J. Geophys. Res., 105,* 25,291-25,304, doi: 10.1029/2000JA900064.

McFadden, J. P., C. W. Carlson, D. Larson, J. Bonnell, F. Mozer, V. Angelopoulos, K.-H. Glassmeier, and U. Auster (2008), THEMIS ESA first science results and performance issues, *Space Sci. Rev.*, 141, 477–508, doi:10.1007/s11214-008-9433-1.

McPherron, R. L., C. T. Russell, and M. P. Aubry (1973), Satellite studies of magnetospheric substorms on August 15, 1968: 9. Phenomenological model for substorms, *J. Geophys. Res.*,78(16), 3131–3149, doi:10.1029/JA078i016p03131.

Moldwin, M. B., and W. J. Hughes (1992a), On the formation and evolution of plasmoids -A survey of ISEE 3 Geotail data, *J. Geophys. Res., 97*, 19,259, doi:10.1029/92JA01598.

Moldwin, M. B., and W. J. Hughes (1992b), Multi-satellite observations of plasmoids -IMP 8 and ISEE 3, *Geophys. Res. Lett., 19*, 1081-1084, doi:10.1029/92GL00779.

Moldwin, M. B., and W. J. Hughes (1993), Geomagnetic substorm association of plasmoids, *J. Geophys. Res., 98*, 81-88, doi:10.1029/92JA02153.

Moldwin, M. B., and W. J. Hughes (1994), Observations of Earthward and tailward propagating flux rope plasmoids: Expanding the plasmoid model of geomagnetic substorms, *J. Geophys. Res., 99*, 183-198, doi:10.1029/93JA02102.

Nagai, T., K. Takahashi, H. Kawano, T. Yamamoto, S. Kokubun, and A. Nishida (1994), Initial GEOTAIL survey of magnetic substorm signatures in the magnetotail, *Geophys. Res. Lett., 21*, 2991-2994, doi:10.1029/94GL01420.

Nagai, T. and Machida, S. (1998) Magnetic Reconnection in the Near-Earth Magnetotail, *AGU Geophysical Monograph Series*, doi: 10.1029/GM105p0211

Nagai, T., I. Shinohara, M. Fujimoto, M. Hoshino, Y. Saito, S. Machida, and T. Mukai (2001), Geotail observations of the Hall current system: Evidence of magnetic reconnection in the magnetotail, *J. Geophys. Res.*, *106*, 25,929-25,950, doi: 10.1029/2001JA900038.

Nagai, T., I. Shinohara, S. Zenitani, R. Nakamura, T. K. M. Nakamura, M. Fujimoto, Y. Saito, and T. Mukai (2013), Three-dimensional structure of magnetic reconnection in the magnetotail from Geotail observations, *J. Geophys. Res. Space Physics*, 118, doi:10.1002/jgra.50247.

Nakamura, R., et al., Motion of the dipolarization front during a flow burst event observed by Cluster, *Geophys. Res. Lett*., 29(20), 1942, doi:10.1029/2002GL015763, 2002.

Nakamura.R et al. (2004), Spacial scale of high-speed flows in the plasma sheet observed by Cluster, *Geophys. Res. Lett, 31*, doi:10.1029/2004GL019558

Nishida, A., M. Scholer, T. Terasawa, S. J. Bame, G. Gloeckler, E. J. Smith, and R. D. Zwickl (1986),Quasi-stagnant plasmoid in the middle tail: A new preexpansion phase phenomenon, *J. Geophys. Res*., *91(A4)*, 4245–4255, doi:10.1029/JA091iA04p04245

Nishida, A., et al. (1994), Transition from slow flow to fast tailward flow in the distant plasma sheet, *Geophys. Res. Lett., 21*, 2939-2942, doi:10.1029/94GL01374.

Nishimura, Y., L. R. Lyons, X. Xing, V. Angelopoulos, E. F. Donovan, S. B. Mende, J. W. Bonnell, and U. Auster (2013a), Identifying the magnetotail source region leading to preonset poleward boundary intensifications, *J. Geophys. Res. Space Physics*, 118, 4335–4340.

Nishimura, Y., L. R. Lyons, X. Xing, V. Angelopoulos, E. F. Donovan, S. B. Mende, J. W. Bonnell, and U. Auster (2013b), Tail reconnection region versus auroral activity inferred from conjugate ARTEMIS plasma sheet flow and auroral observations, *J. Geophys. Res. Space Physics*, 118, 5758–5766, doi:10.1002/jgra.50549.

Ohtani, S., M. A. Shay, and T. Mukai (2004), Temporal structure of the fast convective flow in the plasma sheet: Comparison between observations and two-fluid simulations, *J. Geophys. Res.*, 109, A03210, doi:10.1029/2003JA010002

Panov, E. V., et al. (2010a), Plasma sheet thickness during a bursty bulk flow reversal, J. Geophys. Res., 115, A05213, doi:10.1029/2009JA014743.

Panov, E. V., et al. (2010b), Multiple overshoot and rebound of a bursty bulk flow, Geophys. Res. Lett., 37, L08103, doi:10.1029/2009GL041971.

Petrukovich, A. A. et al. (1998), Two spacecraft observations of a reconnection pulse during an auroral breakup, *J. Geophys. Res.* Volume 103, Issue A1, p. 47-60, doi: 10.1029/97JA02296

Pritchett, P. L., and F. V. Coroniti (2010), A kinetic ballooning/interchange instability in the magnetotail, J. Geophys. Res., 115, A06301, doi:10.1029/ 2009JA014752.

Raj, A. et al. (2002) Wind survey of high-speed bulk flows and field-aligned beams in the near-Earth plasma sheet, *J. Geophys. Res.*, 107, 1419, doi:10.1029/2001JA007547, 2002.

Rastatter, L., and M. Hesse (1999), Patchy Reconnection and evolution of multiple plasmoids in the Earth's magnetotail: E_ects on near-Earth current system, *J. Geophys. Res., 104*, 25,011-25,020, doi:10.1029/1999JA900375.

Richard, R. L., R. J. Walker, R. D. Sydora, and M. Ashour-Abdalla (1989), The coalescence of magnetic flux ropes and reconnection in the magnetotail, *J. Geophys. Res., 94*,2471-2483, doi:10.1029/JA094iA03p02471.

Richardson, I. G., and S. W. H. Cowley (1985), Plasmoid-associated energetic ion bursts in the deep geomagnetic tail: Properties of the boundary layer, *J. Geophys. Res.*, 90(A12), 12133–12158, doi:10.1029/JA090iA12p12133.

Richardson, I. G., M. Scholer, B. T. Tsurutani, P. W. Daly, and D. N. Baker (1987a), Simultaneous observations of the near-earth and distant geomagnetic tail during a substorm by ISEE-1, ISEE-3 and geostationary spacecraft, *Plantery and Space Science, 35*, 209-226, doi:10.1016/0032-0633(87)90090-0.

Richardson, I. G., S. W. H. Cowley, E. W. Hones, Jr., and S. J. Bame (1987b), Plasmoid-associated energetic ion bursts in the deep geomagnetic tail - Properties of plasmoids and the postplasmoid plasma sheet, *J. Geophys. Res., 92*, 9997-10,013, doi:10.1029/JA092iA09p09997.

Runov, A., V. Angelopoulos, M. I. Sitnov, V. A. Sergeev, J. Bonnell, J. P. McFadden, D. Larson, K.-H. Glassmeier, and U. Auster (2009), THEMIS observations of an earthward-propagating dipolarization front, *Geophys. Res. Lett.*, 36, L14106, doi:10.1029/2009GL038980.

Runov, A., V. Angelopoulos, X.-Z. Zhou, X.-J. Zhang, S. Li, F. Plaschke, and J. Bonnell (2011), A THEMIS multicase study of dipolarization fronts in the magnetotail plasma sheet, *J. Geophys. Res.*,116, A05216, doi:10.1029/2010JA016316.

Russell, C. T., and R. L. McPherron (1973), The magnetotail and substorms. *Space Sci Rev.*, 15, 205–266, doi:10.1007/BF00169321.

Russell, C. T. (1974), The solar wind and magnetosphere dynamics, in the book "*Correlated Interplanetary and Magnetospheric Observations*", P. 3, D. Reidel Publ. Co., Dordrecht, Holland

Scholer, M., D. Hovestadt, B. Klecker, G. Gloeckler, and F. M. Ipavich (1984), Characteristics of plasmoidlike structures in the distant magnetotail, *J. Geophys. Res., 89*, 8872-8876, doi:10.1029/JA089iA10p08872.

Semenov, V. S., I. V. Kubyshkin, M. F. Heyn, and H. K. Biernat (1984), Temporal evolution of the convective plasma flow during a reconnection process, *Adv. Space Res., 4*, 471-474.

Sergeev, V., Elphic, R. C., Mozer, F. S., Saint-Marc, A., and Sauvaud, J.-A.(1992), A two-satellite study of nightside flux transfer events in the plasma sheet, Planet. Space Sci., 40, 1551–1572.

Sergeev, V. A., V. Angelopoulos, J. T. Gosling, C. A. Cattell, and C. T. Russell (1996), Detection of localized, plasma-depleted flux tubes or bubbles in the midtail plasma sheet, J. Geophys. Res., 101, 10,817–10,826, doi:10.1029/96JA00460.

Sergeev, V. A., K. Liou, P. T. Newell, S.-I. Ohtani, M. R. Hairston, and F. Rich (2004), Auroral streamers: Characteristics of associated precipitation, convection and field-aligned currents, Ann. Geophys., 22, 537–548, doi:10.5194/angeo-22-537-2004.

Sergeev, V., V. Angelopoulos, S. Apatenkov, J. Bonnell, R. Ergun, R. Nakamura, J. McFadden, D. Larson, and A. Runov (2009), Kinetic structure of the sharp injection/dipolarization front in the flow-braking region, Geophys. Res. Lett., 36, L21105,doi:10.1029/2009GL040658.

Sharma, A. S. et al.(2008), Transient and localized processes in the magnetotail: a review, *Annales Geophysicae, 26*, 955—1006, doi: 10.5194/angeo-26-955-2008

Shiokawa, K., et al. (1998), High-speed ion flow, substorm current wedge, and multiple Pi 2 pulsations, J. Geophys. Res., 103, 4491–4507, doi:10.1029/97JA01680.

Sibeck, D. G., and V. Angelopoulos (2008), THEMIS science objectives and mission phases, Space Sci. Rev., 141, 35–59, doi:10.1007/s11214- 008-9393-5.

Sibeck, D. G., et al. (2011), ARTEMIS Science Objectives, *Space Sci. Rev.*, p. 270, doi:10.1007/s11214-011-9777-9.

Sitnov, M. I., M. Swisdak, and A. V. Divin (2009), Dipolarization fronts as a signature of transient reconnection in the magnetotail, J. Geophys. Res., 114, A04202, doi:10.1029/2008JA013980.

Sitnov, M. I., and M. Swisdak (2011), Onset of collisionless magnetic reconnection in two-dimensional current sheets and formation of dipolarization fronts, *J. Geophys. Res*., 116, A12216, doi:10.1029/2011JA016920.

Slavin, J. A., E. J. Smith, B. T. Tsurutani, D. G. Sibeck, H. J. Singer, D. N. Baker, J. T. Gosling, E. W. Hones, and F. L. Scarf (1984), Substorm associated traveling compression regions in the distant tail - ISEE-3 geotail observations, *Geophys. Res. Lett., 11*, 657-660, doi:10.1029/GL011i007p00657.

Slavin, J. A. et al. (1985), An ISEE 3 study of average and substorm conditions in the distant magnetotail, *J. Geophys. Res.*, vol. 90, Nov. 1, 1985, p. 10,875-10,895, doi: 10.1029/JA090iA11p10875

Slavin, J. A., et al. (1989), CDAW 8 observations of plasmoid signatures in the geomagnetic tail - An assessment, *J. Geophys. Res., 94*, 15,153-15,175, doi:10.1029/JA094iA11p15153.

Slavin, J. A., M. F. Smith, E. L. Mazur, D. N. Baker, E. W. Hones, Jr., T. Iyemori, and E. W. Greenstadt (1993), ISEE 3 observations of traveling compression regions in the earth's magnetotail, *J. Geophys. Res., 98*, 15,425, doi:10.1029/93JA01467.

Slavin, J.A., et al. (1997), WIND, GEOTAIL, and GOES 9 observations of magnetic field dipolarization and bursty bulk flows in the near-tail, *Geophys. Res. Lett.*, doi: 10.1029/97GL00542

Slavin, J. A., et al. (1999), Dual spacecraft observations of lobe magnetic field perturbations before, during and after plasmoid release, *Geophys. Res. Lett., 26*, 2897-2900, doi:10.1029/1999GL003606.

Slavin, J. A., et al. (2003), Geotail observations of magnetic flux ropes in the plasma sheet, *J. Geophys. Res., 108*, 1015, doi:10.1029/2002JA009557.

Slavin, J. A., E. I. Tanskanen, M. Hesse, C. J. Owen, M. W. Dunlop, S. Imber, E. A. Lucek, A. Balogh, and K.-H. Glassmeier (2005), Cluster observations of traveling compression regions in the near-tail, *J. Geophys. Res.*, *110*, A06207, doi:10.1029/2004JA010878.

Sormakov, D.A. and V.A. Sergeev (2008), Topology of Magnetic Flux Ropes in the Magnetospheric Plasma Sheet as Measured by the *Geotail* Spacecraft, *Cosmic Research*, Vol.46, No.5, PP.387-391

Sonnerup, B. U. Ö., and M. Scheible (1998), Minimum and maximum variance analysis, in Analysis Methods for Multi-Spacecraft Data, ISSI Sci. Rep. Ser., vol. 1. edited by Götz Paschmann and Patrick Daly, pp. 185–220, Eur. Space Agency, Noordwijk, Netherlands.

Sweetser, T.H., S.B. Broschart, V.Angelopoulos, G.J. Whiffen, D.C. Folta, M-.K. Chung, S.J. Hatch, M.A. Woodard (2011),ARTEMIS Mission Design, *Space Sci. Rev.*, doi: 10.1007/S11214-012-9869-1

Taguchi, S., J. A. Slavin, and R. P. Lepping (1998a), Traveling compression regions in the midtail: Fifteen years of IMP 8 observations, *J. Geophys. Res.*, *103(A8)*, 17641–17650, doi:10.1029/98JA01206.

Taguchi, S., J. A. Slavin, M. Kiyohara, M. Nose, G. D. Reeves, and R. P. Lepping (1998b), Temporal relationship between midtail traveling compression regions and substorm onset: Evidence for near-Earth neutral line formation in the late growth phase, *J. Geophys. Res.*, 103(A11), 26607–26612, doi:10.1029/98JA02617.

Tsyganenko., N.A. (1995), Modeling the Earth's magnetospheric field confined within a realistic magnetopause. *J. Geophys. Res.*, Vol.100, No. A4, Pages 5599-5612, doi: 94JA03193.

Ugai, M.: Virtual satellite observations of plasmoids generated by fast reconnection in the geomagnetic tail, *Ann. Geophys*., 29, 1411-1422, doi:10.5194/angeo-29-1411-2011, 2011

Wolf, R. A., V. Kumar, F. R. Toffoletto, G. M. Erickson, A. M. Savoie, C. X. Chen, and C. L. Lemon (2006), Estimating local plasma sheet pv5/3 from single spacecraft observations, J. Geophys. Res., 111, A12218, doi:10.1029/2006JA012010.

Wolf, R. A., Y. Wan, X. Xing, J.-C. Zhang, and S. Sazykin (2009), Entropy and plasma sheet transport, J. Geophys. Res., 114, A00D05, doi:10.1029/2009JA014044.

Yao, Z., et al. (2013), Current structures associated with dipolarization fronts, *J. Geophys. Res.* Space Physics, 118, 6980–6985, doi:10.1002/2013JA019290.

Zhou, X.-Z., V. Angelopoulos, V. A. Sergeev, and A. Runov (2010), Accelerated ions ahead of earthward propagating dipolarization fronts, *J. Geophys. Res.*, 115, A00I03, doi:10.1029/2010JA015481.

Zhou, X.-Z., V. Angelopoulos, V. A. Sergeev, and A. Runov (2011), On the nature of precursor flows upstream of advancing dipolarization fronts, *J. Geophys. Res.*, 116, A03222, doi:10.1029/2010JA016165.

Zhou, X.-Z., V. Angelopoulos, A. Runov, J. Liu, and Y. S. Ge (2012), Emergence of the active magnetotail plasma sheet boundary from transient, localized ion acceleration, *J. Geophys. Res.*, 117, A10216, doi:10.1029/2012JA018171.

Zhou, X.-Z., V. Angelopoulos, J. Liu, A. Runov, and S.-S. Li (2014), On the origin of pressure and magnetic perturbations ahead of dipolarization fronts, *J. Geophys. Res.* Space Physics, 119, 211–220, doi:10.1002/2013JA019394.Zong, Q-G., et al. (2004), Cluster observations of earthward flowing plasmoid in the tail, *Geophys. Res. Lett.*, 31, L18803, doi:10.1029/2004GL020692.

Zwickl, R. D. et al. (1984), Evolution of the earth's distant magnetotail - ISEE 3 electron plasma results, , *J. Geophys. Res.* vol. 89, Dec. 1, 1984, p. 11007-11012, doi: 10.1029/JA089iA12p11007